Toward Ultracold Atoms for Quantum Thermalization Studies

by

Omar Hussein

A thesis
presented to the University of Waterloo
in fulfillment of the
thesis requirement for the degree of
Master in Science
in
Physics

Waterloo, Ontario, Canada, 2022

Author's Declaration

I hereby declare that I am the sole author of this thesis. This is a true copy of the thesis, including any required final revisions, as accepted by my examiners.

I understand that my thesis may be made electronically available to the public.

Abstract

Ultracold atoms are a great platform to understand one of the most interesting open problems in physics: quantum thermalization. Building a new lab for ultracold atoms is a challenging task for the various tools that need to be built. In this thesis, the tools tackled are used for cooling and control. For cooling, a potential Zeeman slower was designed and built with the future task of being tested on cesium atoms. For control, an interlock and a current controller circuits were built, and an AOM driver was significantly improved. Finally, we will provide a review of the experiments made with ultracold atoms to study thermalization, and we will show how we are planning to use our tools to join the other labs in the quest to find answers for quantum thermalization.

Table of Contents

List of Figures

Chapter 1

Introduction

The problem of quantum thermalization is how an isolated quantum system can thermalize or, in other words, be described by thermodynamical ensembles. It is a common practice to use statistical mechanics for quantum systems although it is derived originally from classical treatments. Since it apparently works, one can in principle find a way to justify using it through a quantum mechanical treatment. The problem fundamentally lies in how a pure quantum system can be described by a mixed state; furthermore, quantum mechanics is linear unlike classical mechanics, where one can use the ergodic theorem to explain statistical mechanics from a dynamical point of view. Several theoretical advances have been made such as the eigenstate thermalization hypothesis, but nothing yet provides a complete theory.[1,4] On the other hand, several experiments were done to study thermalization. Some of these experiments were done using ultracold atoms due to their precise control and near-ideal isolation. The platform of ultracold atoms was used to study thermalization through its simulation of two systems: the Lieb-Liniger and the Bose-Hubbard models. The Lieb-Liniger model is an integrable system that doesn't thermalize or cannot be described by the canonical ensemble. The experiments were able to show its integrability and were even able to break it. [33,34,39,47,51] For the Bose-Hubbard model, the goal was to find correlations between entanglement and thermalization. In chapter 4, we provide a review of these experiments to know the methods, the results, and the limitations. Our short-term goal is to have a Lieb-Liniger model with periodic boundary conditions, with a knob to break its integrability, and without the technical limitations faced by the other experiments. In the longer run, we would implement entanglement entropy measurements to find correlations between entanglement and how integrable the systems is.

To be able to start searching for answers, we need to build a lab. It is done mainly

through three essential ingredients: a source of atoms, cooling, and control. The source of atoms can be seen in Zach's work.[64] My work and contribution during my Master's years are in the cooling and control parts of the lab. We need to cool down atoms for several reasons including trapping the atoms, simulating the desired Hamiltonians, starting from a precise pure state, and imaging atoms precisely. The first step of cooling atoms is the Zeeman slowing. We will show how we built it and discuss all its details in chapter 2. For the third ingredient, we need control to build and manipulate these Hamiltonians and their states efficiently. The control is done through different electronics that we built for the lab. These electronics are the interlock, the Acousto-Optic Modulator (AOM) driver, and the current controller. The interlock is for safety while the other two devices are for control. All these devices are discussed in chapter 3.

Before discussing the specific projects done to build the lab, we need to know our atoms and the tools that we plan to use to manipulate our atoms. The atoms and tools are the subject of this chapter.

1.1 Atoms

For our experiments, we need a boson and a fermion. Having two kinds of particles provide more ways to manipulate and control your atoms. Our choice of atoms is cesium and lithium. In the following sections, we will discuss all the relevant properties of the atoms and what makes them a good choice for our planned experiments.

1.1.1 Cesium

Cesium is an atom with 55 electrons; only one electron is in the outermost valence shell, the 6s. We are working with ^{133}Cs since it is the only stable isotope. Given that the nuclear spin is $I = \frac{7}{2}$, cesium is a boson since the total spin state $\frac{7}{2} + \frac{1}{2} = 4$ or $|\frac{7}{2} - \frac{1}{2}| = 3$ is an integer. These states come from the addition of angular momenta. Notice that we only considered the spin of one electron, which is the outermost electron, and not the other 54. The reason is that electrons fill all the lower shells in singlet pairs, which means that they have a total spin of zero.

Fine Structure

Before introducing the fine structure, the notation $n^{2S+1}L_J$ used to describe the atom's states should be reviewed. The variable n is the principal number of the energy level of the valence electron. Note that this notation only works for alkali atoms since a single n won't be able to describe more than one valence electron in different energy shells. The variable S is the total spin of the electrons; it will always be $1/2$ for alkalis since only one electron in the outermost shell is unpaired. Orbital angular momentum is denoted as L; a few examples are the following: S for L=0 and P for L=1. Finally, $J = L + S$ is the addition of orbital angular momentum and spin.

The hydrogen atom has the degenerate states of $2^2P_{1/2}$ and $2^2P_{3/2}$, and this degeneracy is lifted when we take the spin-orbit coupling into account. To elaborate more, the proton rotates around the electron in the electron's reference frame; the magnetic field produced by the proton's motion interacts with the dipole moment of the electron. The dipole moment is proportional to the spin while the magnetic field is proportional to the orbital angular momentum. Hence, the name comes from this coupling. We won't jump into the details of the spin-orbit coupling. The only thing that we want to emphasize is that the quantum numbers that allow us to use perturbation theory are $J = L + S$ and $m_j = m_l + m_s$. The main result of this coupling is that the degeneracy is lifted for states with the same L but different J.

In cesium, the D_1 line, $6^2\ \mathrm{S}_{1/2} \longrightarrow 6^2\mathrm{P}_{1/2}$, and the D_2 line, $6^2\ \mathrm{S}_{1/2} \longrightarrow 6^2\mathrm{P}_{3/2}$, have different transition frequencies due to the spin-orbit coupling[1]. The transition frequency of the D_1 line is $\omega_0 = 2\pi \cdot 335.1$ THz. On the other hand, the D_2 line has $\omega_0 = 2\pi \cdot 351.7$ THz. It can be seen that the difference is about $2\pi \cdot 16$ THz, which gives us the advantage to address one of the states without affecting the other.[62]

Hyperfine Structure

The hyperfine structure is the coupling between the magnetic field generated from the electron's total angular momentum, which is proportional to J, and the spin of the nucleus.

[1]The degeneracy between the S-states and the P-state is lifted for a different reason, which is the core electrons shielding the nuclear charge. The S-state tends to penetrate the shielding and sees the nuclear charge more than the P-states.[63] It was important to state this effect since it has a higher scale of energy shifts than the spin-orbit coupling, which is seen in figure 1.1.

The Hamiltonian of this interaction is the following:

$$H_{hs} = A\hat{I} \cdot \hat{J} \tag{1.1}$$

where A is the magnetic dipole constant. The hyperfine structure has another term due to the electric quadrupole, but it was ignored since its effect is lower than the magnetic dipole effect by a factor of 100. The good quantum numbers for the hyperfine structure are $F = I + J$ and $m_f = m_i + m_j$. Using the addition of angular momenta, the ground state $6^2S_{1/2}$ has $F = 3$ or $F = 4$ since $I = 7/2$ and $J = 1/2$. For $6^2P_{1/2}$, $F = 3$ or $F = 4$. Similarly, for $6^2P_{3/2}$, F can be 2, 3, 4, or 5. The degeneracy is lifted in the F-states due to the perturbation of H_{hs}. The energy levels can be seen in the figure from Daniel Steck's document on cesium; it shows the hyperfine structures for the D2 line.[62]

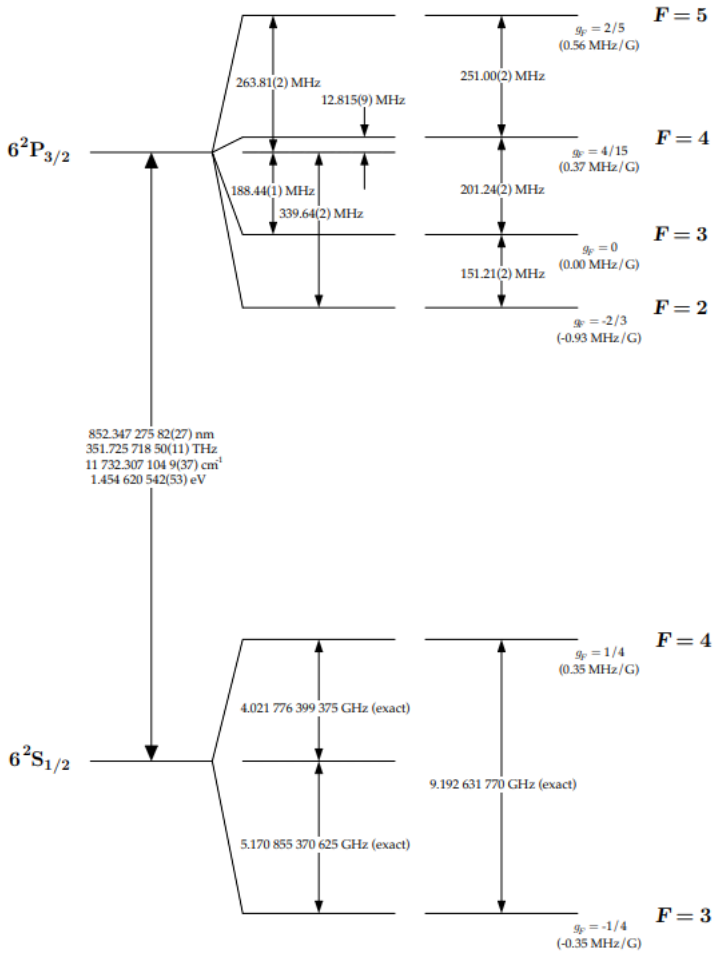

Figure 1.1: **Cesium D2 Line**. The first column shows the transition frequency of the unperturbed D2 line. The next column shows how those unperturbed levels split due to the hyperfine interaction. The last column shows the g_F factors and the relative energies between the consecutive hyperfine states. The figure is taken from ref [62].

The reason for our introduction of the hyperfine structure is that these energy levels are what we are going to target with our lasers; therefore, a natural concern would be if these states can even be targeted separately. The answer is found in the fundamental uncertainty principle, which states that the energy of a hyperfine state has some uncertainty that depends on its decay rate τ. The decay rate corresponds to the uncertainty in time.

Calculating the uncertainty in energy ΔE:

$$\Delta E = \frac{\hbar}{2\tau} = \frac{\hbar\Gamma}{2}$$

From the above equation, one can deduce the uncertainty in angular frequency: $\Delta\omega = \Gamma/2 = 2\pi \cdot 2.61$ MHz, where Γ is known as the natural linewidth. Since the natural linewidth is much smaller than the difference between the $F = 4$ and $F = 5$ states, these states can be targeted independently.

Zeeman Effect

Applying a magnetic field to the atom can change the energy levels; the shift of energy levels is known as the Zeeman effect. The strength of the magnetic field determines the good quantum numbers; therefore, the degeneracy is lifted into states with different quantum numbers depending on the strengths. Consider the following Hamiltonian of a magnetic field interacting with the total atomic magnetic moment μ_{atom}:

$$\begin{aligned} H &= -\mu_{atom} \cdot B \\ &= \mu_{\mathrm{B}} \left(g_S \hat{S} + g_L \hat{L} + g_I \hat{I} \right) \cdot \mathbf{B} \\ &= \mu_{\mathrm{B}} \left(g_S \hat{S}_z + g_L \hat{L}_z + g_I \hat{I}_z \right) B_z \end{aligned} \tag{1.2}$$

where $\mu_{\mathrm{B}} = 9.274 \cdot 10^{-24}$ J/T is the Bohr magneton. Each angular momentum has its g-factor g_i. This Hamiltonian will always be a perturbation for the fine structure since our magnetic fields will never reach the impossibly high magnetic fields that make this Hamiltonian comparable to the fine structure. A rough calculation that shows the strength of such a magnetic field is $B = \frac{h \cdot f}{\mu_{\mathrm{B}}} \approx 1000$ T, where f is the difference between the D1 line and D2 line transitions. Therefore, the quantum numbers $|J\ m_j\rangle$, which are compatible with the fine structure, are the proper ones to start with. We need to transform equation 1.2 to be written in terms of J_z using the Wigner-Eckart theorem[2]:

$$H_{\mathrm{B}} = \mu_{\mathrm{B}} \left(g_S \frac{\langle \hat{S} \cdot \hat{J} \rangle}{J(J+1)} \hat{J}_z + g_L \frac{\langle \hat{L} \cdot \hat{J} \rangle}{J(J+1)} \hat{J}_z + g_I \hat{I}_z \right) B_z = \mu_{\mathrm{B}} \left(g_J \hat{J}_z + g_I \hat{I}_z \right) B_z \tag{1.3}$$

[2]Rigorously the Wigner-Eckart theorem is for expectation value and not for generating new Hamiltonians, but it is in practice treated for generating new Hamiltonians for the proper quantum number

For $g_S = 2$ and $g_L = 1$, g_J is:

$$g_J \simeq 1 + \frac{J(J+1) + S(S+1) - L(L+1)}{2J(J+1)}$$

Now starting from the above equation, the derivation for the energy levels for different strengths or regimes of the magnetic field will be shown.[62]

High Magnetic Field Regime

When the magnetic field is much stronger than the hyperfine Hamiltonian but perturbs the fine structure, H_{hs} acts as a perturbation to the $|Jm_jIm_i\rangle$ states while the states $|J\, m_j\, I\, m_i\rangle$ are eigenstates of equation 1.3. The energy shifts when calculated are the following:

$$E_{|Jm_jIm_i\rangle} = \mu_{\mathrm{B}}\left(g_J m_j + g_I m_i\right) + A_{\mathrm{hfs}} m_j m_i$$

The second term of hyperfine perturbation results from $\langle J_x\rangle = \langle J_y\rangle = 0$ and $\langle J_z\rangle = m_j$. Since g_I is a factor of 10000 lower than g_J, the energy levels mainly divide into sets of lines depending on m_j while the 8 lines in each set are the m_i values due to the hyperfine term. Figure 1.2 shows this categorization in the range of very high magnetic fields.[62]

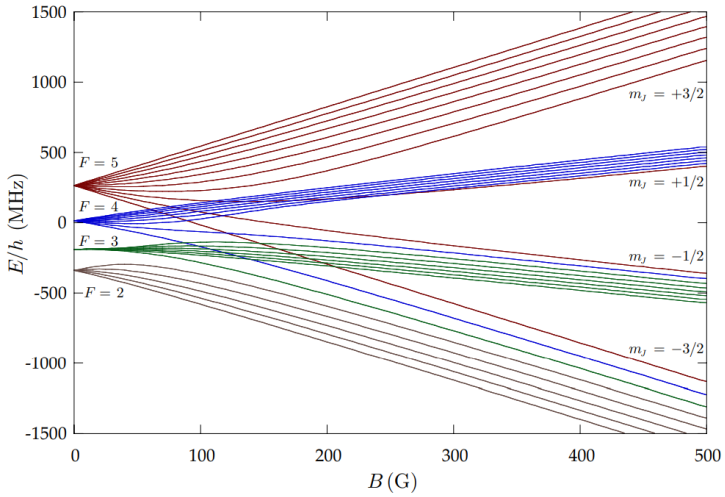

Figure 1.2: **Zeeman Effect on Hyperfine States of** $6^2P_{3/2}$. The anomalous Zeeman effect can be seen at the start while the high magnetic field regime is at the end. The figure is taken from ref [62].

Low Magnetic Field Regime: Anomalous Zeeman Effect

In figure 1.2, one would notice how the state's energy changes linearly with the magnetic field in the low magnetic field regime where H_B is a perturbation to H_{hs}. The effect in this regime is known as the anomalous Zeeman effect since the normal Zeeman effect couldn't explain it. In the anomalous Zeeman effect, the $|F\ m_f\rangle$ quantum numbers will be the right ones to use for perturbation theory. As a result, the Wigner-Eckart theorem will be used again in equation 1.3:

$$H_{\mathrm{B}} = \mu_{\mathrm{B}} g_F \hat{F}_z B_z \tag{1.4}$$

where g_F is:

$$g_F \simeq g_J \frac{F(F+1) - I(I+1) + J(J+1)}{2F(F+1)}$$

For cesium, the g_F factors are seen in figure 1.1. Applying the Hamiltonian on different $|F\ m_f\rangle$ states shows that the degeneracy is lifted on states with different m_f's [62]:

$$\Delta E_{\left|Fm_f\right\rangle} = \mu_{\mathrm{B}} g_F m_f B_z$$

Intermediate fields: Breit-Rabi Formula

For intermediate fields, states with $J = 1/2$ have an analytical formula that describes the Zeeman effect. It is known as the Breit-Rabi formula:

$$E_{\left|J=\frac{1}{2} m_j I m_i\right\rangle} = -\frac{\Delta E_{\mathrm{hfs}}}{2(2I+1)} + g_I \mu_{\mathrm{B}} m_f B \pm \frac{\Delta E_{\mathrm{hfs}}}{2}\left(1 + \frac{4m_f x}{2I+1} + x^2\right)^{1/2}$$

Note again the middle term can be ignored since the nuclear g-factor is too small, $g_I \approx -4 \times 10^{-4}$. This formula is only applied for $J = 1/2$ since there are only two hyperfine states. The sublevels of these states get coupled by the interaction with the magnetic field only when $m_f = m'_f$. This means that for each m_f two states get coupled. In figure 1.3, the Zeeman effect for the ground state is shown and can be completely described by the formula.[62]

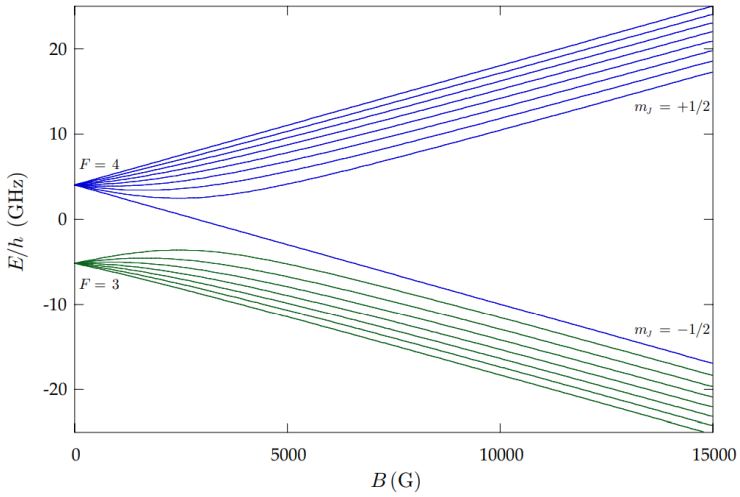

Figure 1.3: **Zeeman Effect on Hyperfine States of** $6^2S_{1/2}$. It shows similar properties in the splitting as the one in figure 1.2. The figure is taken from ref [62].

1.1.2 Lithium

Lithium is our second atom with three electrons, of which only one is a valence electron in the 2s shell. Two isotopes of lithium exist: ^{6}Li and ^{7}Li. Since we already have a boson, we choose a fermion, which is ^{6}Li with $I = 1$. We will now discuss briefly the fine and hyperfine structure of lithium. We will also show the Zeeman effect on the states.

Fine structure, Hyperfine structure, and Zeeman Effect

Starting with the fine structure, the transition frequency of the D_1 line is $\omega_0 = 2\pi \cdot 446.78$ THz while the D_2 line has $\omega_0 = 2\pi \cdot 446.79$ THz. A difference of 10 GHz is enough to target each state alone. Note also the difference of about 100 THz in the D line of cesium and that of lithium. This difference shows the reason why each type of atom can be controlled and manipulated individually. For example, one can create independent lattices for each kind of atom.

Regarding the hyperfine structure, the ground state $2^2S_{1/2}$ has $F = 1/2$ and $F = 3/2$. The state $2^2P_{1/2}$ has $F = 1/2$ and $F = 3/2$. Finally, $2^2P_{3/2}$ has $F = 1/2$, $F = 3/2$, and $F = 5/2$. In figure 1.4, one can see the D lines with the hyperfine structure included. Note

from the figure that $2^2P_{3/2}$ has its F-states inverted in energy. The state $F = 3/2$ has higher energy than that of $F = 5/2$. This inversion is due to the negative magnetic dipole constant of lithium.

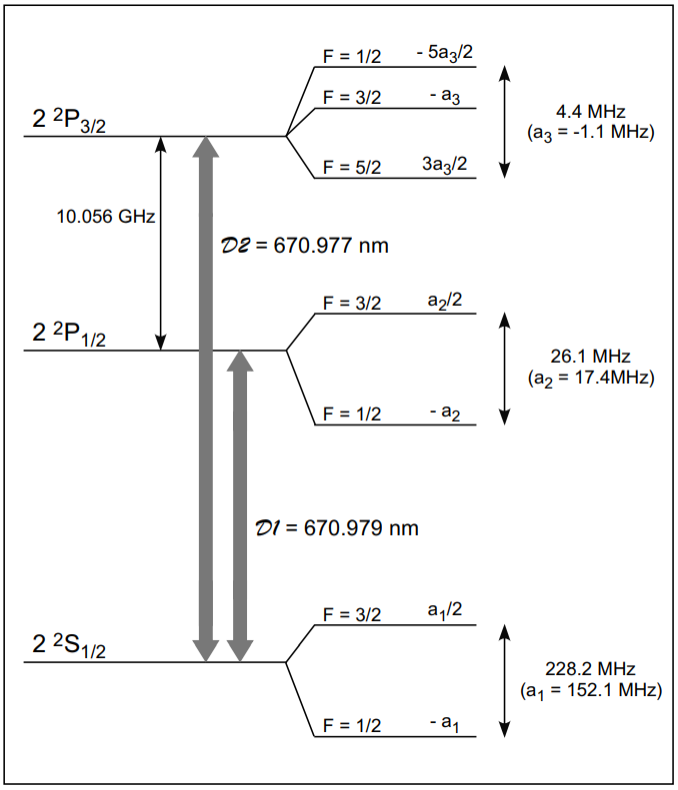

Figure 1.4: **Lithium D Lines**. The first column shows the transition frequency of the unperturbed D line while the next column shows how those unperturbed levels split due to the hyperfine interaction. The figure is taken from ref [65].

For completeness, we show the Zeeman effect on the hyperfine states of lithium. Note the difference in the range of the magnetic field to observe the three regimes of the Zeeman effect. For example, 6 G is enough to observe the high field regime in the hyperfine states of $6^2P_{3/2}$ while those of cesium needed about 400 G.[65]

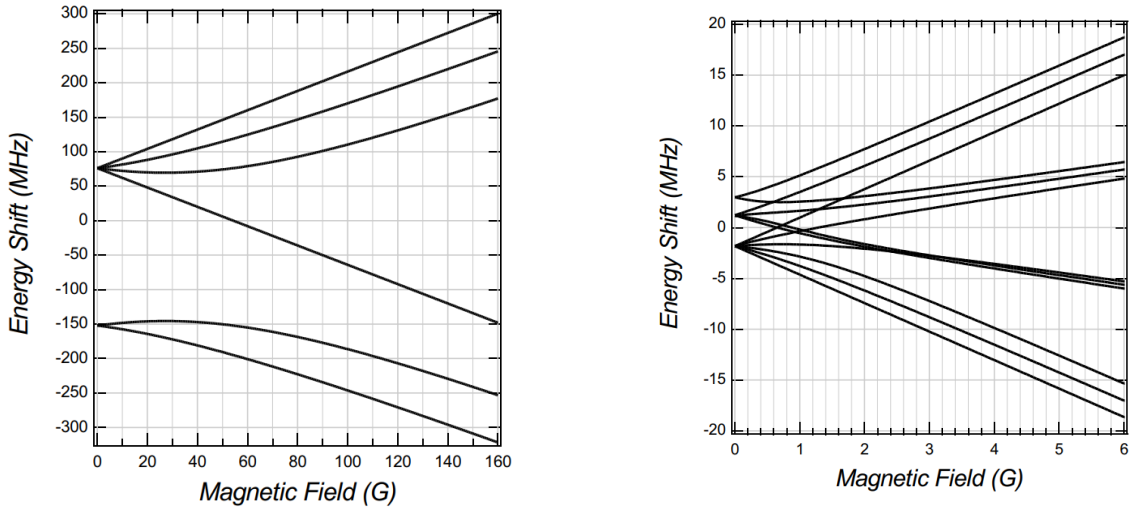

(a) Zeeman effect on hyperfine states of $2^2S_{1/2}$.

(b) Zeeman effect on hyperfine states of $6^2P_{3/2}$.

Figure 1.5: **Zeeman Effect in Lithium**. Figure is from ref [65].

1.1.3 Feshbach Resonance

The main reason behind our choice of atoms is their Feshbach resonances. A Feshbach resonance is a physical phenomenon related to coupling a molecular bound state to a scattering state. The details of this topic are beyond the scope of this thesis. However, the important thing to know is that Feshbach resonances can be used to tune scattering lengths using magnetic fields:

$$a(B) = a_0 \left(1 - \frac{\Delta}{B - B_0}\right) \tag{1.5}$$

where a_0 is the background scattering length, B_0 is the magnetic field at which the resonance occurs, and Δ is the resonance width. The scattering length can be tuned to manipulate the interactions between atoms. Cesium has a lot of Feshbach resonances, and lithium has an exceptionally good Feshbach resonance. Moreover, there are multiple Feshbach resonances between the two atoms such that we can tune their interactions with each other. This tool will be very important for quenches when we suddenly change the interaction strength. It will also be important for a time-of-flight measurement. The interactions will be turned off since they may affect the measurement.[67]

1.2 Tools

As has been said, two of the main ingredients for building a new lab are cooling and control. Cooling is essential since it is a prerequisite for trapping, precise control, and imaging, and control is essential for manipulation. In this section, we mainly discuss the tools that we would need and that are the motivation for what has been built so far during this Masters.

1.2.1 Cooling

Without cooling, one wouldn't be able to trap atoms and subject them to the wanted Hamiltonians. For example, one wouldn't be able to create a 1D Bose gas unless the thermal energy is lower than the first excited state energy of the transverse confinement. In addition, cooling allows imaging with single atom resolution.[66] Finally, thermalization is usually studied by starting with a ground state, which requires a Bose-Einstein condensate to be achieved.

Creating a Bose-Einstein condensate requires four stages of cooling. The first stage is using a Zeeman slower to slow down atoms after they exit from the oven. They are slowed down until they can be captured by the Magneto-Optical trap (MOT), which is the second stage of cooling. In the second phase of cooling, the atom in the MOT behaves like a damped harmonic oscillator that traps atoms and further cools them down to the Doppler limit, which is the lowest temperature that can be achieved in a MOT. This temperature is restricted by the random walks in the velocity space of an atom due to the random nature of spontaneous emission that causes recoils in random directions. In the third stage, we use sub-Doppler techniques that make use of the hyperfine structure to cool below the Doppler limit. Finally, we use evaporative cooling to remove the highest energy atoms of our system and achieve a BEC.

The first stage of cooling, which is the Zeeman slowing, is the subject of chapter 2, and we show all the details needed to build the Zeeman slower. Furthermore, all the mentioned stages need lasers, which are controlled by the AOM driver discussed in chapter 3. We mainly discuss how we improved the range of the AOM driver's output to have better evaporative cooling.

1.2.2 Control

The Zeeman slower needs its current to be controlled, and the evaporative cooling needs the power of the laser to be controlled. However, control is not only about cooling but also about simulating Hamiltonians with the ability to freely tune their parameters. It is also about changing quantum states as wanted. Starting with the Hamiltonians, it is pretty common that one may want to create a lattice using standing waves as seen in figure 1.6. The lattice is used for the simulation of the Bose-Hubbard model or for creating an array of 1D Bose gases. These standing waves should have a certain wavelength and a certain amplitude with minimal noise. To achieve that, one needs to control the laser's power and frequency, which is done by the AOM driver. The AOM driver's feedback loop ensures that the measured amplitude meets the wanted amplitude, and its built-in external RF connector adds to its ability the use of external RF sources with ultra-low frequency noise. These precise standing waves aren't only used for creating Hamiltonians. They are also used to take quantum states out of equilibrium. In some of the experiments to be shown in chapter 4, they used a sequence of standing waves to divide a Bose gas into two pieces with opposite, equal momenta.

In general, quenches are done by any sudden change in the Hamiltonian or, through the Heisenberg picture, the state. Using standing waves is just one way of many. Another tool that we are planning to use for quenches is the Feshbach resonances, which are not implemented by many labs studying thermalization. One can use Feshbach resonances to change the interaction strength between atoms by manipulating the scattering lengths. These resonances can be used not only in quenches but also for measurements and technical aspects like reducing three-body collisions. Achieving this tool needs great control over the current of the Feshbach coils, which is the goal of the current controller discussed in chapter 3.

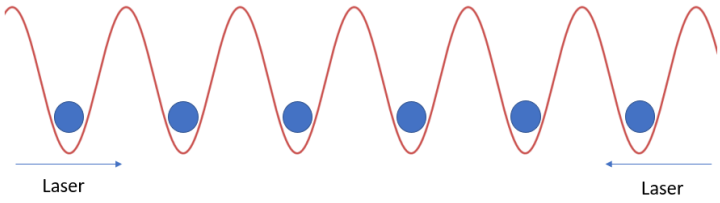

Figure 1.6: **Creating an Optical Lattice**. Due to the dipole force, one can use standing waves from two lasers with blue detuning to trap atoms at the nodes. At blue detuning, the atoms get repelled from high-intensity regions of the light.

In conclusion, the AOM driver and current controller will be essential for probing and manipulating our systems; thus, a lot of details will be discussed later about the design processes, hoping that it may help future students in our lab with their future projects.

Chapter 2

Zeeman Slower

Introduction

The Zeeman slower is the first step of cooling after the atoms are ejected from the oven before entering the MOT chamber, the second phase of cooling. Atoms come out with high speed; their speeds in a beam can be described by a distribution similar to the Maxwell-Boltzmann distribution for a gas of particles:

$$f(v)\,dv = \frac{1}{2}\left(\frac{m}{k_B T}\right)^2 v^3 \exp\left(-\frac{mv^2}{2k_B T}\right) dv$$

Note the difference of having v^3 in the effusive beam distribution instead of v^2 seen in the common Maxwell-Boltzmann distribution. This difference in the distribution is attributed for having a beam rather than a gas, and the distribution's temperature is that of the oven. These high speed atoms need to be slowed down to a velocity lower than the capture velocity of the MOT, a task that is done by the Zeeman slower.

In this section, we will introduce the scattering force and show how we constructed the Zeeman slower for cesium and lithium. For cesium, we will specify the velocities we want to address out of the oven and construct a Zeeman slower for this velocity that slows it down to a lower velocity than the capture one. In lithium, we will take on the design we already made for the cesium, modify the current, and then find out the final velocity coming out of it.

2.1 Scattering Force

Conservation of momentum requires that the momentum of the atom to change when it absorbs a photon; thus, you would expect that an atom would slow down if it is absorbing a photon moving against the atom's velocity. One could argue that the scattering force from the spontaneous decay or stimulated emission will introduce a recoil momentum to the atom that may cancel out the slowing down from the absorption. However, the spontaneous decay doesn't favor a certain direction for the emitted photons, so the average effect of emission will be no change of the momentum.

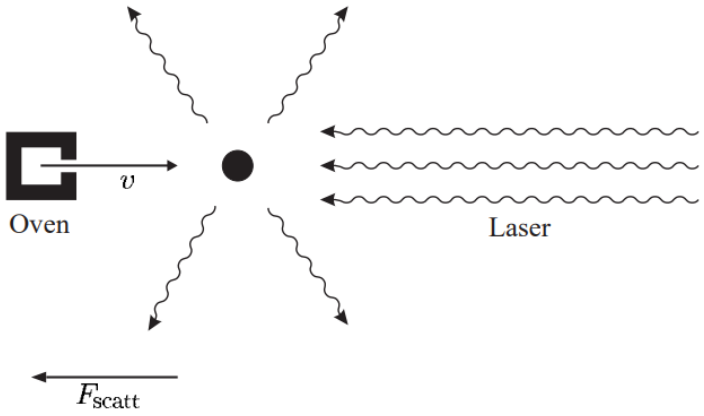

Figure 2.1: **The Concept of Scattering Force**. An atom absorbs the photons of the laser from a specific direction and emits them in all directions. The figure is taken from ref [63].

Since it is evident that we can slow down atoms with scattering force, it is now important to figure out a way to quantify this force. The force is equal to the change of momentum, which is $\hbar k$, multiplied by the rate that this process happens. The rate of change here is the decay rate Γ times the probability ρ_{22} being in the excited state, which can be derived from the optical Bloch equations [63]. The force is the following:

$$F_{scatt} = \hbar k \cdot \Gamma \rho_{22} = \hbar k \frac{\Gamma}{2} \frac{I/I_{\text{sat}}}{1 + I/I_{\text{sat}} + 4\delta^2/\Gamma^2} \tag{2.1}$$

where $\delta = \omega - \omega_0$ is the detuning, $I_{sat} = \frac{\hbar\omega_0\Gamma}{2\sigma_0}$ is the saturation intensity with the cross section σ_0, and $I/I_{\text{sat}} = 2\Omega^2/\Gamma^2$. Saturation intensity is a fundamental quantity of the

atom. It is one photon energy per decay time per the largest cross section of the atom. At resonance, saturation intensity gives you half the maximum force possible; this intensity of a laser can easily be achieved in the lab.[63]

Cesium

2.2 Analytic Design

To design the Zeeman slower, one needs to know the capture velocity needed in the MOT. The capture velocity of the MOT will give us some idea on what velocity we want to target out of the oven. After that, we will find an analytic field for the ideal Zeeman slower and try to match it as close as we can while making sure that we don't exceed a certain acceleration that may let us lose the atoms. Finally, we will calculate the final output velocity out of this slower.

2.2.1 Capture Velocity of MOT

To estimate out the capture velocity, one should figure out three important specifications. One is to choose between two transitions: the D1 or D2 line. Since we are targeting hyperfine states, one should next choose the targeted F-states. Finally, we have to know the intensity since it affects the scattering force and thus the cooling.

D1 vs D2 line

One needs to aim for a cycling transition. In other words, you need to figure out a transition that you won't need to depend strongly on repumping beams. A repumping beam is a laser that drives the transition from the unwanted states to the ones you are targeting. The best way to understand the importance of a cycling transition is through the cases of the D1 and D2 lines discussed in chapter 1.

For the D1 line, assume that you are targeting the transition between F=4 in the $6^2S_{1/2}$ and F=4 in the $6^2P_{1/2}$. This transition is allowed since the selection rule[1] for electric dipole

[1] We refer the reader to Foot's book for more discussion about selection rules.[63]

transition is $\Delta F = 0, \pm 1$. However, spontaneous decay would allow the transition from F=4 in the $6^2P_{1/2}$ to F=3 in $6^2S_{1/2}$. If you didn't have a repumping transition that takes the atoms back from the F=3 to F=4 in $6^2S_{1/2}$, then you would lose your atoms over time. In this case, a repumping beam is needed to take the atoms from the unwanted state to an excited state such that a spontaneous decay will bring them down to the correct one. If the spontaneous emission brings the atoms back to the wrong state, they will keep being repumped until they decay to the correct state.

For the D2 line, if we targeted the transition from F=4 in the $6^2S_{1/2}$ to F=5 in $6^2P_{3/2}$, then spontaneous decay will only move the atoms back to F=4 of the S state. Thus, we don't need a strong repumping beam to counter the decay. In conclusion, the D2 line is chosen because it has a cycling transition.

F-State

Based on the example just given above, we would choose F=4 to F=5 in $6^2S_{1/2}$ and $6^2P_{3/2}$, respectively. The choice of F quantum numbers isn't enough because both the MOT and the Zeeman slower depend on magnetic fields, so we need to also choose the m_f quantum states. The corresponding selection rule is $\Delta m_f = 0, \pm 1$, depending on the polarization of the beam; circular polarizations are the ones that drive the $\Delta m_f = \pm 1$ transitions, depending on the handedness.

In the MOT, the states absorb photons of different circular polarizations from each direction, which means the only transitions are of $\Delta m_f = \pm 1$. Unlike the MOT, the Zeeman slower doesn't have to be driven by a circular polarization; however, it will actually be advantageous. The case is analogous to the discussion about the D2 line. Choosing a circular polarization that drives a transition between $m_f = 4$ in the S state and $m_f = 5$ in the P state will allow the spontaneous decay to only happen between the same two states. In conclusion, we would use $m_f = 4$ and $m_f = 5$ or $m_f = -4$ and $m_f = -5$. These F-states with the highest and lowest m_f's are known as stretched states: $|F = 5\ m_f = 5\rangle$ and $|F = 5\ m_f = -5\rangle$.

Intensity

For the intensity, recall the scattering force in equation 2.1. As $I \to \infty$, $F_{\text{scatt}} = \hbar k \frac{\Gamma}{2}$, which is the maximum force. The intensity needed is impossible physically; however, achieving

the saturation intensity is easy and can be exceeded. The force for the saturation intensity is the following:

$$F_{\text{exp}} = \hbar k \frac{\Gamma}{4}$$

This force can be achieved even with detuning since we can get back our force by increasing the intensity beyond the saturation one.[63] The deceleration from this force will be calculated since it will be useful later:

$$a_s = \hbar k \frac{\Gamma}{4m} = 28897.48 \text{ m/s}^2 \tag{2.2}$$

where $\Gamma = 32.9 \cdot 10^6 \text{ s}^{-1} = 2\pi \cdot 5.234$ MHz is the decay rate for an excited state in the D2 line, k is the wavenumber of the D2 transition, and m is the mass of cesium.[62]

Capture Velocity

Now, we will try to figure out an estimate for the capture velocity since we now know our force or intensity. Using the constant deceleration calculated in equation 2.2, we find the capture velocity:

$$V_c = \sqrt{2 \cdot a_s \cdot D} = 34 \text{ m/s}$$

where $D = 2$ cm is the laser's diameter; we were not planning to have a MOT greater than 2 cm in diameter.

2.2.2 Ideal Field for the Zeeman Slower

Basic Idea

When an atom moves toward a beam of a certain frequency ω with a velocity v, the atom sees the frequency Doppler shifted due to its motion.

$$\omega' = \omega + kv$$

The idea of the Zeeman slower is fairly simple. Once the atoms are out of the oven with a certain velocity, you would want to shine a laser with a fixed frequency such that the doppler shift would make it on resonance. As a result, the atoms will experience a scattering force and slow down. Once the atoms start slowing down, the fixed frequency of the laser won't be on resonance anymore because the lower velocity will make less Doppler shift.

To compensate for the difference, the Zeeman shift will be used. The following simple equation illustrates the process:

$$\omega_0 = \omega + kv + \frac{\mu_B \cdot B(z)}{\hbar} \tag{2.3}$$

where ω is the laser's frequency and ω_0 is the transition frequency. As v becomes less, the magnetic field B will increase to satisfy the equation. One may ask what magnetic field regime is used for the Zeeman effect term in equation 2.3. Since the atoms are in stretched states, it doesn't matter which regime they are in. The reason is that a stretched state $|F\ m_f\rangle$ maps to one and only one state in the basis $|m_j\ m_i\rangle$. For example, $|F = 5\ m_f = 5\rangle = |m_j = \frac{3}{2}\ m_i = \frac{7}{2}\rangle$.

The Zeeman slower can be designed in two ways. One way is to have a zero magnetic field at the beginning of the coil such that the detuning will be determined based on which Zeeman capture velocity we are going to target. A Zeeman capture velocity is the highest velocity that the slower can slow down. Another way is to have the largest magnetic field at the beginning of the coil; consequently, the laser will be on resonance at the end of the coil. This resonance may push back or slow down the atoms less than the wanted velocity as they move through the transition between the Zeeman slower and the MOT chamber. We went with the former way to avoid pushing back the atoms; a simple picture that gives you a rough idea of the design is below.

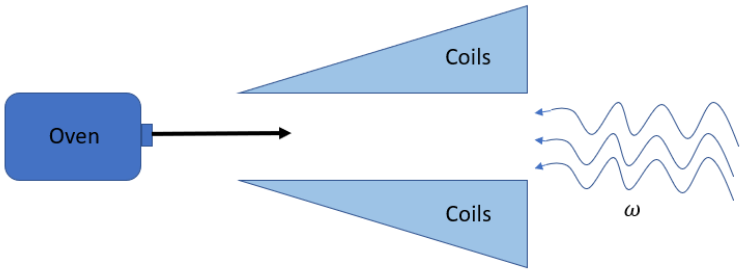

Figure 2.2: **A Rough Concept of a Zeeman Slower**. The simple drawing shows a rough design of the Zeeman slower. Note that the coils are thicker at the right end for a greater magnetic field.

Finally, it is important to note that the Zeeman slower slows down all particles that are equal to or less than the Zeeman capture velocity. The reason is that the atom will be

on resonance somewhere in the middle of the coil even if it wasn't at resonance at the start due to its less velocity. If an atom with the Zeeman capture velocity enters the slower, it will slow down to be on resonance at the next point until it exits the slower, so there is a resonant frequency for each velocity between the Zeeman capture velocity and the output velocity. For that reason, any atom with a velocity in this interval will be slowed down.

Design

Now that the MOT's capture velocity is determined, the target is to slow down atoms to lower than this value, so we need to choose what speed the Zeeman slower should output. We will pick 25 m/s, which is lower than the capture velocity just to have room for any non-idealities. To roughly get the input speed of the slower, we apply a constant acceleration equation:

$$v_{input} = \sqrt{(25\text{ m/s})^2 + 2 \cdot \mathrm{a_s} \cdot (10\text{ cm})} = 80.03\text{ m/s}$$

The 10 cm is the length of the Zeeman slower. Now note the following; this velocity is a rough estimate for a couple of reasons. One reason is that designing a slower won't give you a constant deceleration over the whole length. For example, there will be fringing fields at the end of the slower. Another reason is that you may decide to change the input velocity for better results, which you get to know from working on the slower and facing some technicalities. In fact, the velocity we ended up addressing was 76.4 m/s instead of 80.03 m/s. We reduced it at first because we were able to have a slower over about only 8.5cm of the pipe at the first iterations of the coil; the first iteration will be seen in the numerical section. Later, we were able to have even a larger distance but didn't address a different speed because that speed already had a satisfying population in the effusive beam distribution The oven will usually be at a temperature between 310C and 360C. With this Zeeman capture velocity for a temperature of 325C, we are targeting to slow down about 1% of the atoms exiting the oven's nozzle; the flux of the atoms is 10^{11} atoms/$(\mathrm{s} \cdot \mathrm{cm}^2)$.[64]

Now suppose we ran over these iterations and decided to address the 76.4 m/s instead of the previous one; we need to find the ideal Zeeman slower magnetic field. The basic calculation made in Foot will be done here [63]. Remember that the whole point of the Zeeman slower is to use magnetic field to compensate for the difference in frequency seen by the atom resulting from the Doppler effect and the detuning put by hand. The Zeeman effect part of equation 2.3 takes the effect of the magnetic field on both stretched states the F=4 and $m_F = -4$ for the S state and the F=5 and $m_f = -5$ for the P state. We chose the

negative m_f quantum numbers because these decrease the difference in frequency ω_0. The other part of the equation that needs to be determined is the detuning ω. It is determined so that the input velocity is already on resonance, so $\omega_0 - \omega = kv = 2\pi \cdot 89.63$ MHz. Solving this equation for the magnetic field, we have:

$$B(z) = \frac{\hbar}{\mu_B}(\omega_0 - \omega) - \frac{\hbar \cdot k \cdot v}{\mu_B} = B_0 - B_0\sqrt{1 - \frac{2 \cdot a \cdot z}{v_{input}^2}} \tag{2.4}$$

where $B_0 = \frac{\hbar}{\mu_B}(\omega_0 - \omega) = \frac{h \cdot v_{input}}{\lambda \cdot \mu_B} = 64.04G$.

2.2.3 Acceleration

As it is seen, a Zeeman slower is designed in such a way that at each point the magnetic field makes up for a specific velocity such that the combination of its Doppler effect, the Zeeman effect, and the detuning makes the transition on resonance. We give the term targeted velocity to this specific velocity. The last calculation needed is to find the acceleration of the targeted velocities of the magnetic field created and to check that they don't exceed the maximum acceleration of equation 2.2. The reason is that an atom will be lost if it was asked to accelerate more than the maximum acceleration physically possible. To calculate the acceleration of the targeted velocity, we simply take the time derivative of equation 2.3:

$$a_{target} = -\frac{\mu_B}{\hbar \cdot k}\frac{dB}{dz}\frac{dz}{dt} \tag{2.5}$$

where dz/dt is just the velocity, so we would rearrange equation 2.3 again and substitute it back:

$$a_{target} = |-\frac{\mu_B}{\hbar \cdot k^2}\frac{dB}{dz}(\delta - \frac{\mu_B \cdot B(z)}{\hbar})| \leq \hbar k\frac{\Gamma}{4m} \tag{2.6}$$

This equation here is extremely important. Although the Zeeman slower is designed to have a constant deceleration, designing a configuration for it numerically won't be perfect and will give us something close to the constant deceleration but not exactly. The most important thing to care about after these imperfections is the targeted acceleration, which is the acceleration asked from the atoms to achieve the target velocity at each point along the slower. For a fixed saturation intensity, the maximum acceleration that can be achieved is when the laser is on resonance; therefore, the atom will be left behind if you asked it to decelerate more than the maximum deceleration of equation 2.2. To understand the concept more, if at one point the atom was asked to decelerate more than it could, the atom won't be on resonance in the immediate next point in the slower, and it will keep being off resonance for the rest of the slower and will be lost.

Numerical Work

Th second step is to design the slower numerically. The main code for numerically calculating the magnetic field from a coil was done by another student. Before using the code to design the Zeeman slower, I modified it a bit to be user friendly. Instead of using a start and stop angle to define the length of the coil, I made it possible to define the length according to the actual start and end positions of the coil. With trial and error approach, I was able to design the first version of the Zeeman slower, which then needed to be improved. The second version will also be shown.

2.2.4 First Try

Layers Configuration and Power

In figure 2.3, it can be seen that the first configuration was made of 18 layers. At the top right end, one can see that there are a couple of equal narrow layers. From a technical aspect, these will be hard to implement because naturally the top layer will be winded over the lower one that requires it to be wider. Furthermore, it is better to avoid narrow layers as errors will be more significant in the narrow ones, and errors are more likely to happen at the end of the coil as a transition in the winding from one layer to the next occurs. These errors at the end are expected to happen because the of the tension from wrapping the first winding in a new layer. This tension will try to find a place in the lower layer rather than to start a new layer. The coils all have the same current. The power dissipated in this configuration was about 0.15Watt, which doesn't need water cooling.

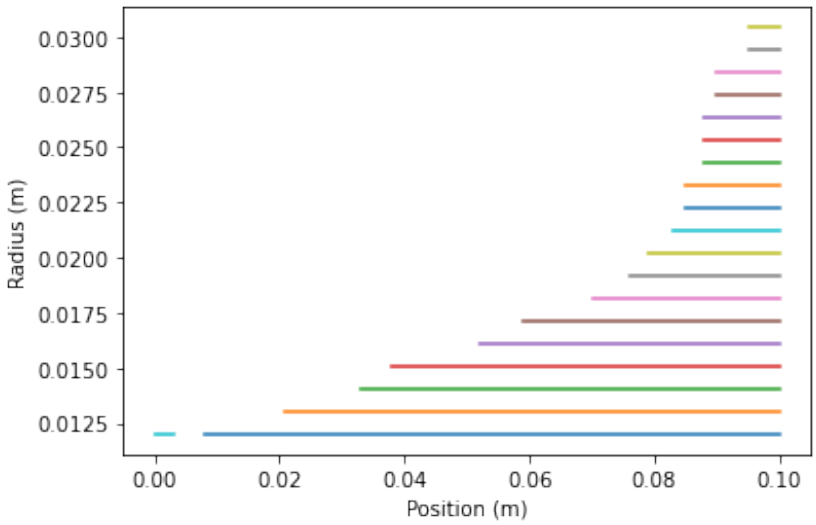

Figure 2.3: **Layer Configuration of the First Version**. This version of the slower is made of 18 layers. The y-axis shows the radius of the layer from the center of the slower's pipe, and the x-axis shows the 10 cm length of the slower.

Magnetic field

In figure 2.4, we compare the analytic and numerical results. The red graph is the analytic magnetic field while the blue one is the numerically calculated magnetic field of our configuration; it can be seen how they are well matched. To find the output velocity, substitute the peak magnetic field, which is 34.6 Gauss, in the same equation. The corresponding velocity is 35 m/s, which is slightly higher than the MOT's capture velocity. Obviously, we needed a better slower.

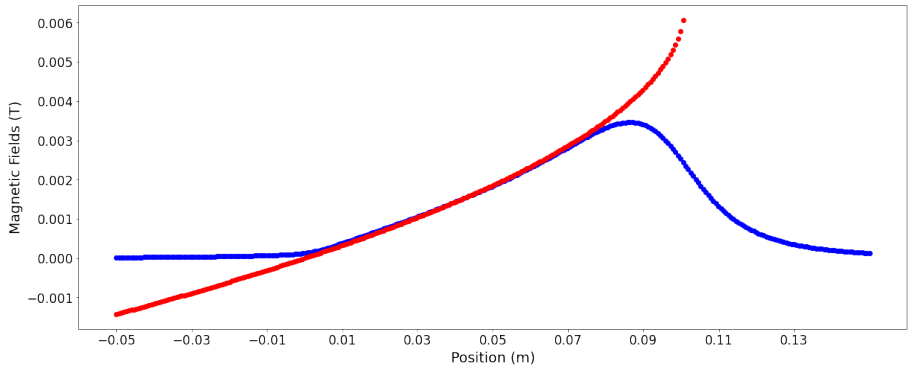

Figure 2.4: **Magnetic field vs Position**. The blue line is numerically calculated magnetic field, and the red line is the analytic magnetic field.

Acceleration

In figure 2.5, we show the ideal targeted acceleration and the targeted acceleration from our numerical model. It can be seen here that we managed to keep the acceleration, which is the green graph, below the threshold plotted by the black line. However, it can be seen that we didn't fully use the 10cm of the length of the pipe. Thus, our second try was to take more advantage of the length we have.

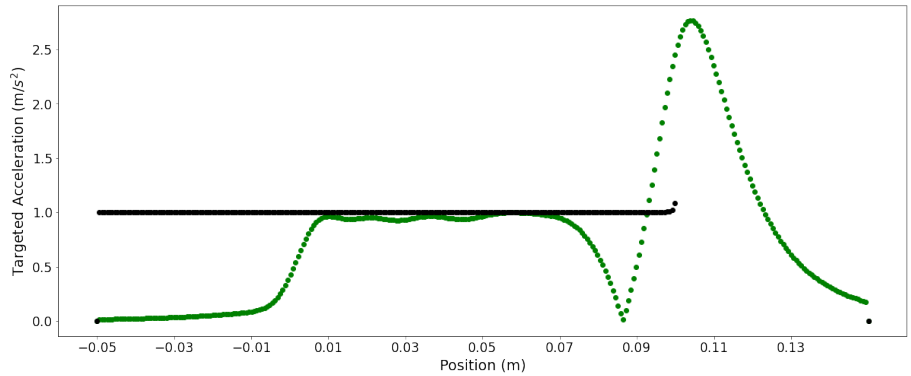

Figure 2.5: **Targeted Acceleration vs Position**. The black line is the normalized maximum acceleration while the green graph is the numerically calculated targeted acceleration.

2.2.5 Second Try

Layers Configuration

In the second try, we decided to add two more tricks. To smooth out the pumps in the targeted acceleration, we added double pitches, where there is a wire's diameter gap between one winding and the next one. The double pitches in most layers are located at the start of each one. If you look at the layers, you may find that some of the segments like layer 2 and layer 3 are divided into three colors; the first color from the left is the double pitch. Another trick is to add a different set of coils with high current at the end of the coil; it helps to extend the range of the field. You will find a very small segment at the end of layer 1 to layer 7; this segment is the high current coils. The middle colored segment is just a normal single pitched coil. This configuration has 10 layers, and its total power is 0.11W.

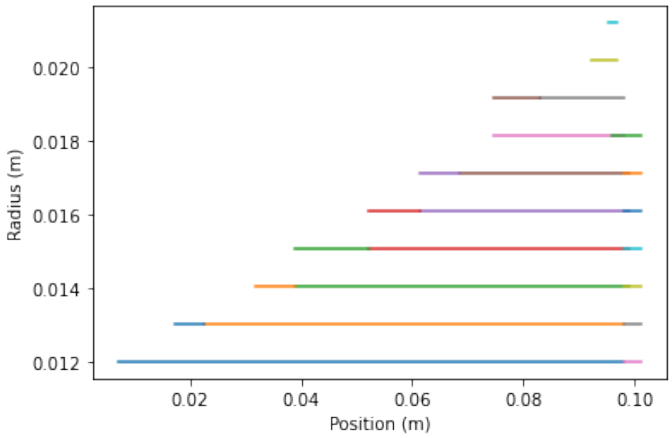

Figure 2.6: **Layer Configuration of the Second Version**. It has 10 layers. Whenever there is a layer with three colors, the first color is a double pitch. Furthermore, the tiny segment at the end of the first to the seventh layer is the high current part. The middle part is just a single pitched coil.

Magnetic Field

As before, figure 2.7 shows the comparison between the analytic and the numerical magnetic fields. The output velocity is 25.07 m/s due to 43.02G.

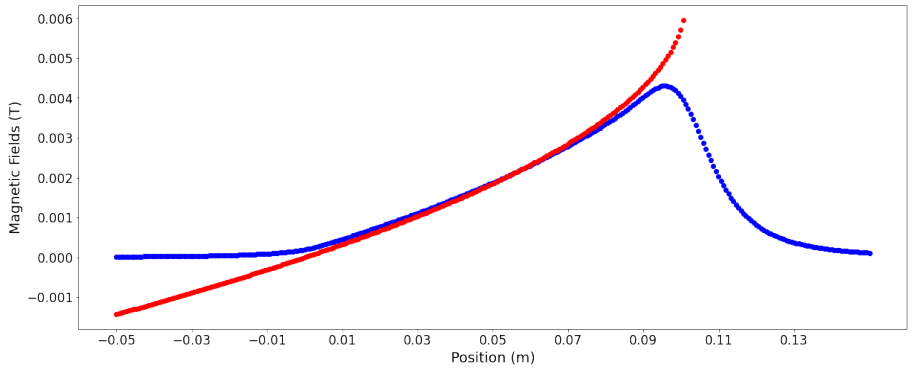

Figure 2.7: **Magnetic Field of the Second Version**. The blue curve is the magnetic field of the numerical model while the red graph is the analytic magnetic field.

Acceleration

It can be seen here in figure 2.8 that we were indeed able to extend our range of deceleration, which results in a better output velocity. Another improvement is how the curve is smoother, which is due to the double pitch coils.

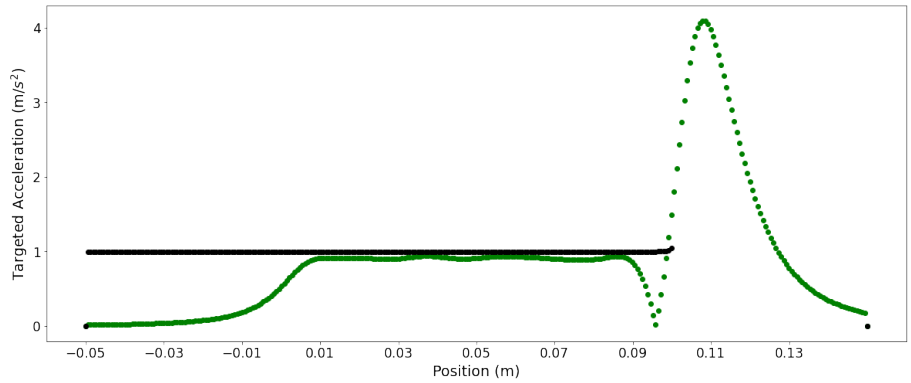

Figure 2.8: **Targeted Acceleration of Second Version**. The targeted acceleration (green) has an extended range.

Implementation

To build the Zeeman slower, we needed to get an 18-AWG wire from Digi-Key and the full nipple from Kurt-Lesker. The process of making the Zeeman Slower is shown here.

2.2.6 Vacuum Work

First of all, the stainless steel full nipple will be used in a vaccuum system. Before just using it, one should know that stainless steel usually has some hydrogen trapped in it, and this gas slowly diffuses out while in vaccuum. This diffusion may ruin the quality of our vaccuum during the experiments; thus, we need to bake the nipple first to diffuse out any hydrogen.

Baking is the process where you diffuse out most of the hydrogen you can. To do so, we first created a vaccuum inside the nipple. To create a vaccuum, we connected two pumps: a roughing pump and a turbo pump. A roughing pump starts first to put it to a lower pressure that is safe for the turbo pump to start working. The turbo pump lowers the pressure inside even more than what the roughing pump can do.

After creating the vaccuum, we would heat up the nipple so that we speed up the diffusion; we heated it up to about 310 Celsius. It was heated by wrapping a heating tape around it and increasing the temperature gradually. Finally, a lot of aluminum foils were wrapped around the pipe for insulation. A valid question can be asked here: why would one use a conductor like aluminum for insulation? The answer is that it is wrapped in a way such that there is a little air gap, which acts as an insulator between the pipe and the aluminum. Furthermore, the shiny part of the aluminum is facing inward to reflect any radiation from the heating thus insulating it better. A picture of the baking setup is below.

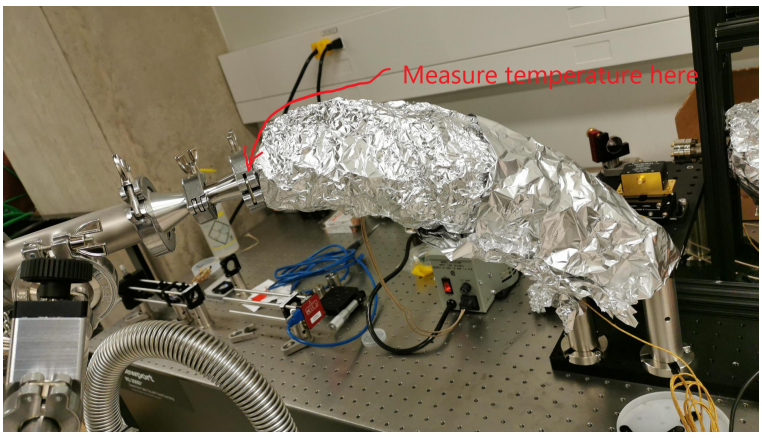

Figure 2.9: **Baking of the coil**. The aluminum foils are covering the full nipple and the heating tape.

2.2.7 Wrapping the coil

We started with baking since the non-magnetic epoxy doesn't withstand the 310C. The non-magnetic epoxy from Cotronics was used to fix each layer of coil windings in its place before wrapping the next layer. We mainly depended on tension to wrap the coils. Before using just tension, we thought about using a kapton tape to fix the coil positions before we apply the epoxy; however, the tape produced a lot of gaps, which made the use of only tension to be the best way. A picture below shows the Zeeman slower.

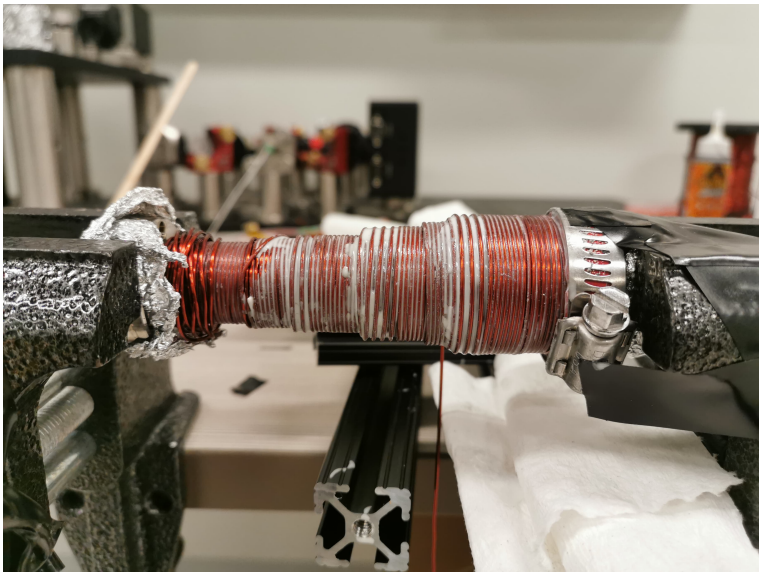

Figure 2.10: **Winding Wires**. The Zeeman slower in the process of wrapping the wires.

As it can be seen in the picture, the metal clamp at the far right was used to fix a 3D printed plastic piece. The 3D plastic part was used to serve as a hard wall to make the winding easier; it makes the moving from one layer to the next natural. It also serves as a barrier so that we can wind the lower current part first then the narrow high current coils later. A picture below shows the 3D printed piece.

Figure 2.11: **A 3D printed Plastic Part**. It was used for wrapping the coils to act as barrier for a more natural transition from one layer to the next.

Measurement

After wrapping the coils, we started measuring the magnetic field using Hirst's GM08 gaussmeter. We applied a current of 0.376A to the larger part of the coil and 2.7A to the end coils. We were able to get the following profile for the magnetic field.

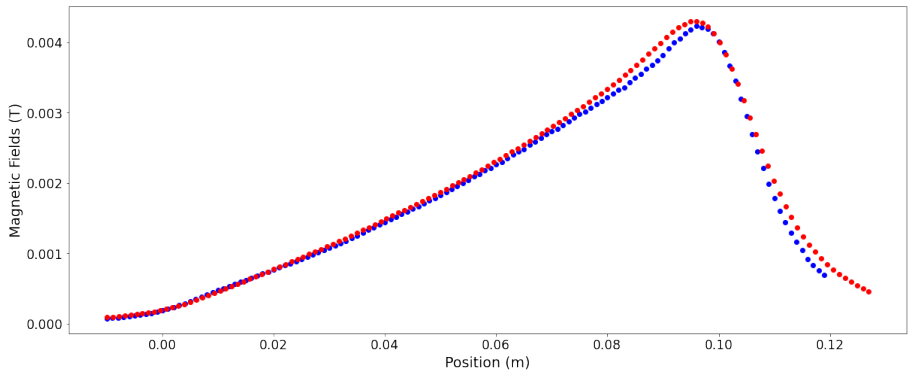

Figure 2.12: **Measured Magnetic field vs Numerical Magnetic Field**. Theblue graph is the measured magnetic field with currents of 0.376 A applied to the larger part of the coil and of 2.7 A to the end coils.

From figure 2.12, our peak magnetic field is 42.2 G, which corresponds to an output

velocity of 26.05m/s. The output velocity is still less than the MOT's capture velocity as we aimed. Although the magnetic field profile looks promising, we still have to check the targeted acceleration. With a few simple lines of code, we were able to graph it.

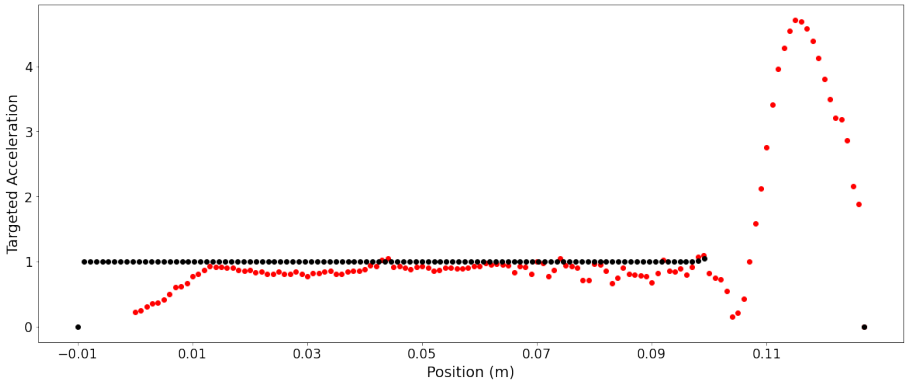

Figure 2.13: **The Measured targeted acceleration vs Ideal Targeted Acceleration**. The red line representing the measured acceleration is nearly horizontal except at the end. The few points that exceed the black line can be fixed easily by lowering the current by a small factor.

The acceleration is nearly horizontal except at the end of the coil. The imperfections at the end of the graph are expected because of the non-ideal intersection between the low-current coil and the high-current part as we approach the peak. The few red points above the black line can be lowered easily by lowering the current, which will consequently lower the peak magnetic field. In conclusion, the measurement of the potential slower is promising, and applying it to atoms is what remains.

Lithium

2.3 Analytic Design

All the reasons used to explain the transitions chosen will also be applied here. We will use the D2 line to drive a transition between F=3/2 in the S state and F=5/2 in the P state. Assuming that we will also have our laser at saturation intensity, the acceleration will be the following:

$$a = \hbar k \frac{\Gamma}{4m} = 912006 \text{ m/s}^2 \tag{2.7}$$

The much lower mass significantly increased the acceleration. Using the same simple calculation of the MOT's capture velocity, we find that the it is 191 m/s. The rest of the calculations done in cesium won't be made here since the strategy of making the slower will be different.

Before talking about the strategy, one should determine the capture velocity of the slower. Using the new acceleration, one finds that the largest velocity can be captured is about 467 m/s; we choose 396 m/s in case of any non-idealities. This adressed velocity of 396 m/s also ensures us that a good amount of the population of lithium atoms in the oven can be captured in the MOT. In the same temperature 325C, we would capture about 1.3% of the atoms exiting through the nozzle. After determining the capture velocity, the strategy will be the following. We will increase the current by a certain factor so that we can target this velocity at the start of the slower; consequently, the peak of the magnetic field will determine the output velocity of the slower.

2.4 Numerical Work

By just adjusting the current by a factor of 7.5 in the code, we got a slower for lithium. However, the slower will have a higher power of 6.16W.

Magnetic Field and Acceleration

Below you can find the graph for the magnetic field. The output velocity is 98.4 m/s for a peak of 331.7G. We can trap even more particles if we targeted a higher velocity. One can also see how the targeted acceleration is below the threshold.

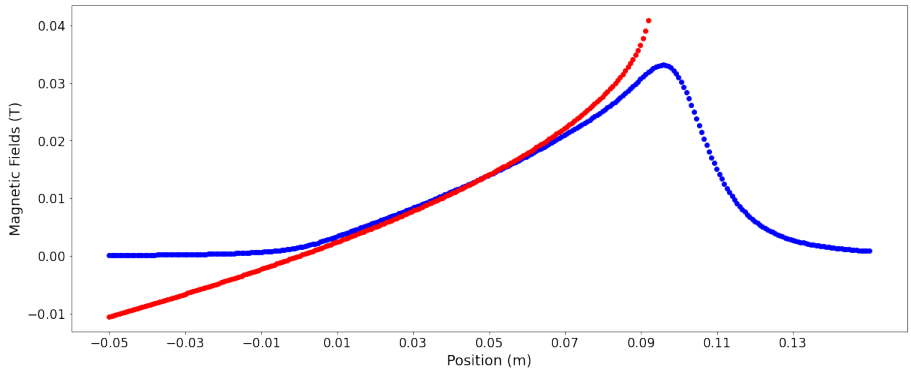

Figure 2.14: **Magnetic Field of Lithium Slower**. The graphs are produced by increasing the current by a factor of 7.5 .

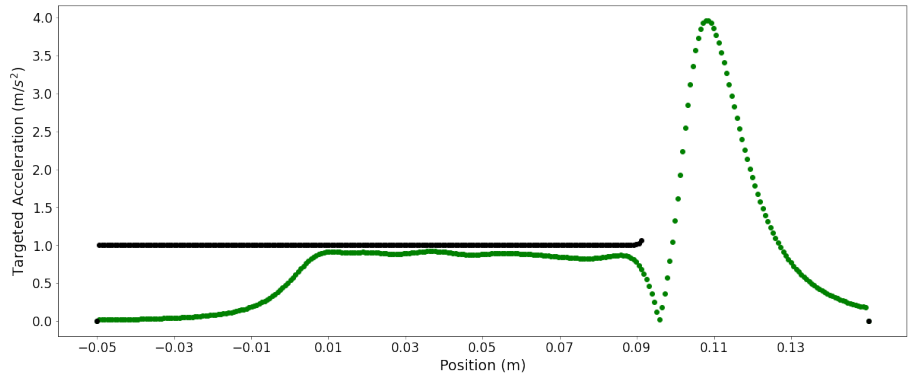

Figure 2.15: **Targeted Acceleration of Lithium Slower**. The green line doesn't exceed the maximum acceleration indicated by the black line.

Chapter 3

Electronics

Introduction

To achieve our goals of cooling down the atoms and using them to study quantum thermalization, we have to build electronics for safety and control. In this chapter, we will cover the three circuits that I worked with in the lab: Interlock, AOM driver, and Current controller.

3.1 Interlock

An interlock is a safety device that keeps both people and equipment safe. It reads in values from sensors, compares them to a safe range, and then sends a digital signal to a switch to control whether the equipment is on or off.

3.1.1 Example Use Cases

We will briefly discuss two cases where this interlock will be used. To start with, high current wires that produce magnetic fields must be water cooled so that they don't get overheated. To achieve that, we measure the water flow in a sensor. If the flow rate is lower than a certain threshold, then the wire isn't cooled properly; as a result, the interlock will send a 0V signal to cut off the power supply. Otherwise, it will keep sending 5V to keep

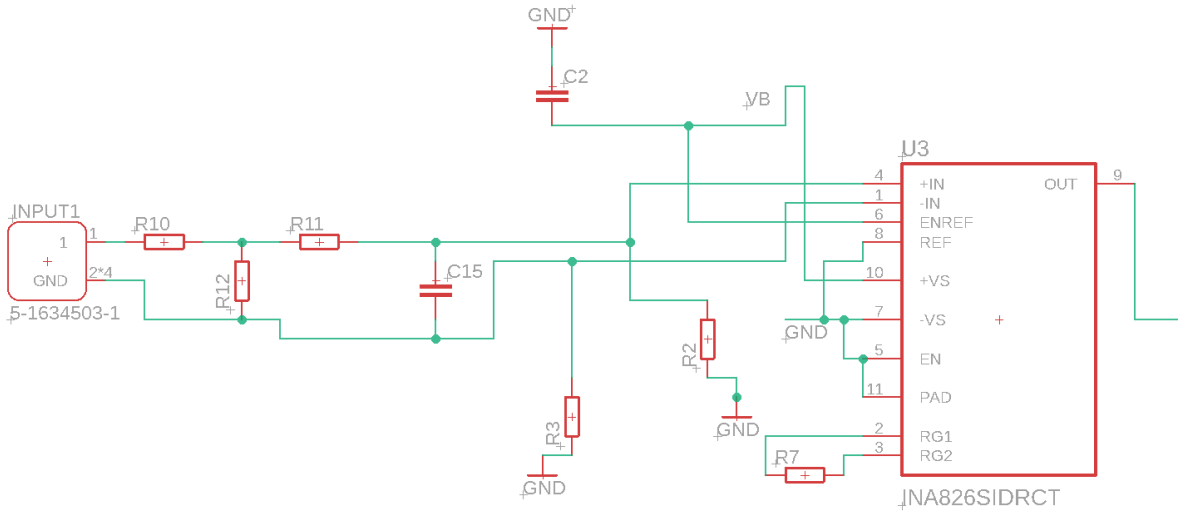

Figure 3.1: **Input Part of the Circuit**. The input of the circuit is followed by a voltage divider for scaling and then by a low-pass filter. Pull-down resistors are R2 and R3, and C2 is just a bypass capacitor.

the current flowing.

A photonic crystal fiber can carry high-power infrared light. The fiber can get burned from the runaway heating that happens when the power entering the tip of the fiber doesn't exit from the end. As a result, we will measure the power of the input and of the output of the fiber by photodiodes. If the difference exceeds the safety threshold, we will send 0V to the AOM to stop the light. Otherwise, the 5V will keep the AOM on.

3.1.2 The Circuit

In this circuit, we will explain some basic concepts like the separation of grounds. The circuit will be divided into four parts: the input, the code, the output, and the power. The code is applied to an Arduino Uno.

The Input

The first step is to read the input signal while isolating the interlock's ground from the ground of the circuit where the signal comes from. The purpose of the isolation is to avoid ground loops. The ground of a circuit is the reference voltage for any signal in the circuit. A ground loop is formed when two points are connected to the same reference voltage but have different voltages. It may appear confusing to know that different points of the ground, which is the reference voltage in this case, can have different voltages, but there are several causes responsible for the problem. Two known causes of many are the common impedance coupling and electromagnetic induction from environmental disturbances. To understand common impedance coupling, it is crucial to understand that wires ideally have zero resistance, but practically they do have very small resistance that can cause some issues. Common impedance coupling happens when two circuits share the same ground path as shown in figure 3.2. The wire that connects the right and left circuits to the ground has a resistance of RG instead of the ideal zero resistance. The resistors R1 and R2 can be thought of as loads of each circuit. When a current I1 resulting from source V1 and its load flows through RG, a voltage difference across RG will affect the reference voltage of the right part of the circuit; the voltage across R2 decreases as I1 increases. Although both circuits were connected to the same ground, the right circuit will see a ground of a different voltage due to the voltage difference across RG; thus, a ground loop is created.

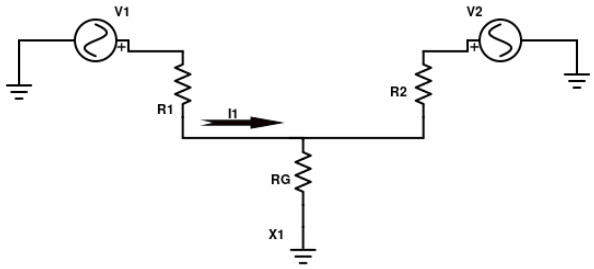

Figure 3.2: **Common Impedance Coupling**. Two circuits with different voltage sources are connected to the same ground. The current I1 from the first circuit affects the reference voltage of the second circuit.

If we thought of the sources as two circuits and send a signal between them as shown in figure 3.3, a loop is formed that can conduct current easily as a result of electromagnetic induction from any environmental disturbances. A common noise is the 60 Hz of the AC electricity in the wall.

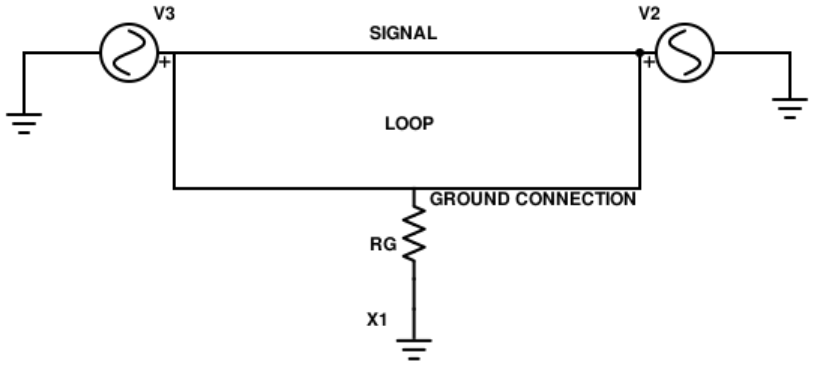

Figure 3.3: **Electromagnetic Induction in a Ground Loop**. The loop created between the two circuits can conduct current from electromagnetic induction.

To solve the ground loop issue, we used an instrumentation amplifier, which is U3 in figure 3.1. The signal sent to the interlock is referenced to the ground of the source circuit. Since the difference between the signal and the ground is the actual signal, an instrumentation amplifier is used, which outputs the difference between its inputs; the inputs are the signal and its ground. Since the instrumentation amplifier (inamp) is supplied by the interlock's power and ground, the output will be referenced to this ground; thus, the grounds are separated.

The circuit has some additional features that can be seen in the schematic. The features include a low-pass filter at the start for unwanted noise. Another feature is the voltage divider at the input of the inamp to control our scaling. It is placed before the inamp because of the inamp's rails. The rails of an inamp are the positive and negative power supplies that supply it. These voltages will also be the highest and lowest voltages that the inamp can output; as a result, the inputs should be scaled to be within the rails. The voltages of the rails are $\pm$6V since the Arduino Uno reads up to 5V; the extra 1V is to avoid clipping of the signal, which was found when the circuit was powered by 5V.

It is common practice to add a pull-down resistor at the inputs so that the inamp reads zero when no signal is connected. A pull-down resistor is a resistor that is connected between the input and the ground. When no signal is connected, no current passes through the resistor; as a result, no voltage difference is created, which makes the input of the inamp connected to the ground. Without the pull-down resistor, the inamp would read just fluctuations when no specific voltage is connected. Finally, bypass capacitors were

connected to have a better DC power supply to the inamp; their specifications and values are from the inamp's datasheet. A bypass capacitor allows a path for the AC noise ripple to the ground directly, which better cleans the DC signal. To understand why the AC ripple will choose the path of the capacitor, recall that the impedance of the capacitor is $\frac{1}{\omega C}$.

The Code

The processing of the information given by the input signal is done by a code written for the Arduino Uno, a microcontroller board. The code includes three parts. One part is simply measuring the inputs using AnalogRead(), comparing the difference to the safe threshold, and finally outputting either 5V or 0V to control the circuit. AanalogRead() is the function used to read an analog input to the Arduino Uno.

The second part is responsible to calculate the ratio of the output to the input measurement and send it as a signal; the ratio will show how well coupled the light is to the fiber and can be used to achieve better coupling. The code instructs the Arduino Uno to send a Pulse-Modulated Width (PWM) signal whose duty cycle is the ratio. The PWM technique is designed to use digital means to send analog signals; it sends a 500Hz signal with a duty cycle of your choice. The duty cycle is the fraction of one period of time of the signal where the signal is 5V. For example, a 75% duty cycle means that 1.5ms of the whole 2ms will be 5V. To elaborate how the ratio results from the duty cycle, the voltage of the signal is on average $0.75 \cdot 5 = 3.75V$; then the ratio between the output and the input would be $\frac{3.75}{5}$. The goal of the output part of the circuit is to get a constant voltage for the average instead of the varying signal; the process will be shown later.

The third and most difficult part of the code is making the Arduino faster. It is important to understand the factors that affect the speed. One factor is the functions used in the code and their implementation time. For example, AnalogRead() takes some time to be performed; thus, increasing the number of this function in your code tends to increase its running time and thus decreases the frequency bandwidth, which is the maximum frequency that the Arduino can respond well to. Serial.begin() is another function that is necessary to establish a communication between the Arduino and the computer. In our case, it is used to know the analog values read by the Arduino. This function tends to decrease the speed, so it is usually removed to increase the frequency bandwidth after testing the precision of the measurement.

To understand how to speed up the Arduino, one should know how it generally works. The Arduino's clock is 16MHz, which means that the Arduino Uno can perform up to 16 million instructions per second. One never observes such a high speed since simple functions usually have a lot of safety and validation code that takes a significant amount of the clock available. The goal of the speeding part of the code is then to lower the number of instructions needed or to remove any default limits designed to the speed of certain functions.

AnalogRead() uses an Analog-to-Digital converter(ADC) to read the analog inputs; the ADC converts an analog input to a 10-bit digital value. The ADC has a sampling rate determined by the Arduino's clock and a prescale register. The prescale factor is just a number from a certain set that controls the clock frequency for the ADC. For example, a prescale of 128 gives a sampling rate of 9600Hz. To see that, the clock frequency of the ADC is the 16MHz divided by the prescale factor, 16MHz/128 = 125kHz. The sampling rate is determined by how many clocks or instructions are needed to perform the conversion; 13 clocks are needed for the Arduino Uno. Therefore, the sampling rate is 125kHz/13 = 9600Hz. By default, the Arduino is set to 9600Hz while it can be faster, so the objective of the code is to choose an appropriate prescale factor that gives a faster sampling rate.[68] Note that the word "appropriate" was said since a higher sampling rate may lower down the precision. A table that shows the sampling rate for every prescale factor is shown in figure 3.4.

Table 1: Prescale register

Prescale	ADPS2 ADPS1 ADPS0	Clock freq (MHz)	Sampling rate (KHz)
2	0 0 1	8	615
4	0 1 0	4	307
8	0 1 1	2	153
16	1 0 0	1	76.8
32	1 0 1	0.5	38.4
64	1 1 0	0.25	19.2
128	1 1 1	0.125	9.6

Figure 3.4: **Table of Prescale Factors**. The table shows the prescale factors with their corresponding sampling rate and clock frequency.This table is taken from ref [68].

The Output

The output of the circuit is designed to optimally send signals to any receiving device; it includes two outputs: the ratio and the controlling signal. Each output goes through an opamp that acts as a buffer to avoid too much drawn current from the Arduino if it ever had to do that. Recall that the opamp has a very high input impedance so that it will never draw too much current from the Arduino's output and very low output impedance so that whatever load connected to the opamp can draw the current it needs. The opamps are U1 and U2 in the schematic shown in figure 3.5.

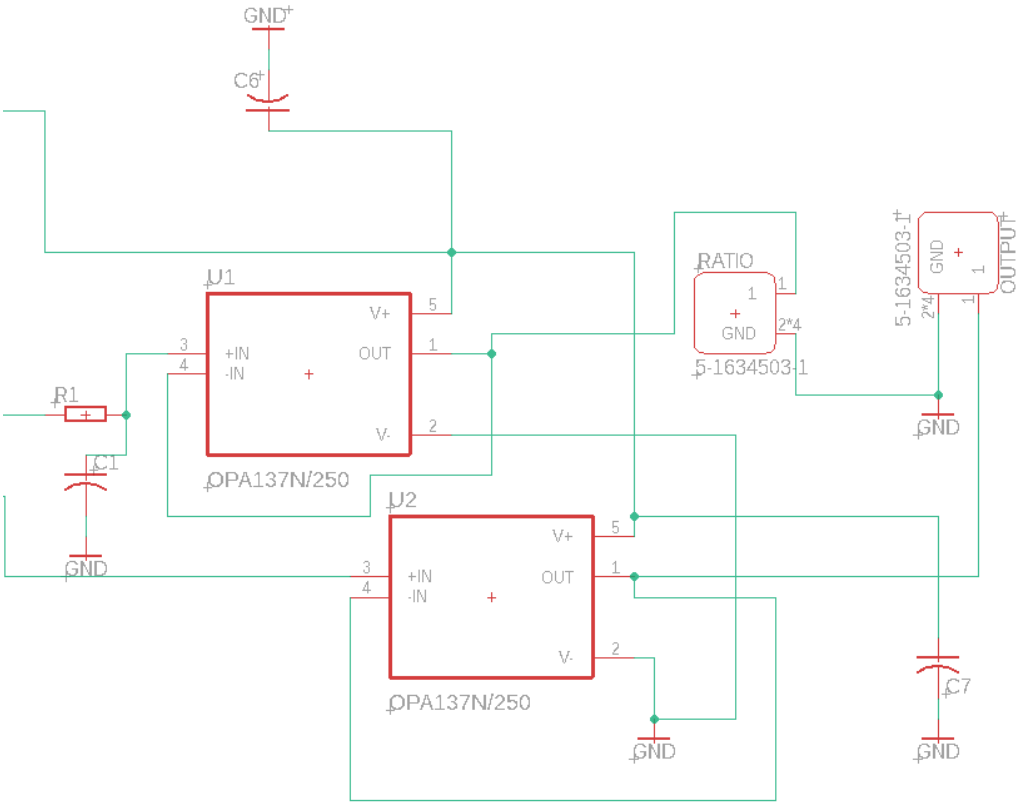

Figure 3.5: **Output Part of the Circuit**. The output part of the circuit has two opamps U1 and U2. The opamp U1 is the one used for the ratio, so a low-pass filter can be seen at its input.

Only for the ratio output, the opamp has an aggressive low-pass filter at its input; it

has a cut off frequency of about 10Hz. The purpose of the low-pass filter is to have a DC voltage equal to the ratio. To understand that, recall that any signal can be decomposed into sinusoidal waves of different frequencies according to Fourier transform; the DC voltage is a signal of frequency zero. The low-pass filter allows all signals below 10Hz to pass through. The 10Hz was a rough good estimate that satisfied two points. One point is that it is lower than 60Hz, which is a common noise caused by the AC electricity in the wall. The second point is that the 10Hz is compatible for optimizing the coupling since a human eye samples about 30 frames per second (30Hz), to which a human usually have a slower decision making response. Therefore, something between 10Hz and 25Hz would be a good frequency for optimization.

It is important to note the reason why we didn't isolate our output ground from our Arduino; in other words, why we didn't put an optoisolator or an inamp to isolate the Arduino's ground to whatever circuit we are sending our signal to. The reason is that there is only one output. We justify the only one output statement by arguing that the DC value output will be connected to a voltmeter that won't affect our circuit in any way. Since there is only one output, the Arduino's ground, which is floating, will connect to the ground of the receiving circuit. Recall that we isolate the ground to avoid ground loops; the ground loops only happen if we had non-floating different grounds from different circuits. However here, we only have a floating ground that connects to a non-floating ground, so this isn't a problem.

The Power

The first iteration of the circuit was powered by two different supplies, which was inconvenient. The Arduino was powered by the USB connection to the computer, and the electronics of the board such as the inamps used a DC power supply. Since the Arduino has a 5V pin that can be used to power the electronics, we thought of using it to make the interlock more compact.

When the circuit was tested with a 5V power supply, it showed some clipping of the signal, but the clipping disappeared for 5.5V. Thus, the 5V supplied by the Arduino was not enough and needed to be converted to a 5.5V or more. One way to achieve this conversion is by using a buck booster, which is a device that can scale up or down a DC voltage. The buck booster in the interlock turns up the voltage to 12V, and then a linear regulator is used to clean up the power supply, to reduce noise, and to lower the voltage down to 6V. Going from 12V to 6V seems like a waste of a lot of power, which is indeed the case. The

buck booster we used is easy to implement, so we favored that over heat dissipation since the circuit doesn't draw a lot of current. Recall that the power dissipated is proportional to the current drawn multiplied by the voltage difference, $P = \Delta V \cdot I$.

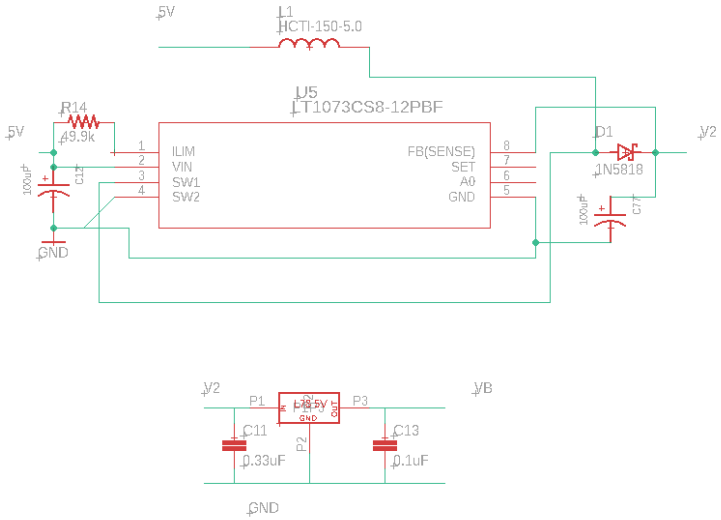

Figure 3.6: **Power Part of the Circuit**. The buck booster is shown at the top while the linear regulator is shown at the bottom. All the extra components are from the datasheet

The top circuit in figure 3.6 is the buck booster which increases the voltage to 12V. The configuration around this component is taken from the datasheet. The linear regulator is the bottom component.

3.1.3 Testing Speed and Precision

The final step is to test the interlock to show the speed up and its effect on precision. The test is performed by observing the Arduino's response to an input of 5V square wave of different frequencies while the second input is terminated, which is an another way to say zero volts. If the interlock performs well, then the output response signal will be a similar 5V square wave of the same frequency. It will also have a π phase since it will output 5V when the difference between the inputs is zero and 0V when the difference is 5V. The response signal is always red in the figures while the input signal is blue.

Note that we care about a steady, accurate response frequency. There would also be a phase difference that corresponds to a delay to the response signal. Its importance depends on the application. To elaborate more, if there was a 1kHz maximum response frequency and a phase difference of π, then the interlock would react 0.5ms late to the failure; this delay might be harmless for some applications. On the other hand, an accurate frequency shows how efficiently the Arduino can spot a signal with its sampling rate.

Clock speed vs Response Frequency

In this test, we prove the speeding up by checking how well the response frequency agrees with the input frequency as we change the prescale factor. The test fails when there is a difference of about 100Hz between both signals.

In the first case, we set the clock frequency to 0.5MHz by choosing a prescale factor of 32. We find that the highest frequency that it can stick to fairly close is 3.1kHz and could never reach 3.2kHz; note that the measurement was done on a span of 6ms. Both cases can be seen in figures 3.7 and 3.8. Note that the response signal in the 3.1kHz case has a steady phase difference and follows the input well. On the other hand, the phase difference of the 3.2kHz is changing over the span, and it doesn't follow the signal well as can be seen at -0.5ms of the measurement graph in figure 3.8. We used the oscilloscope in the Moku instrument to send and measure the signal.

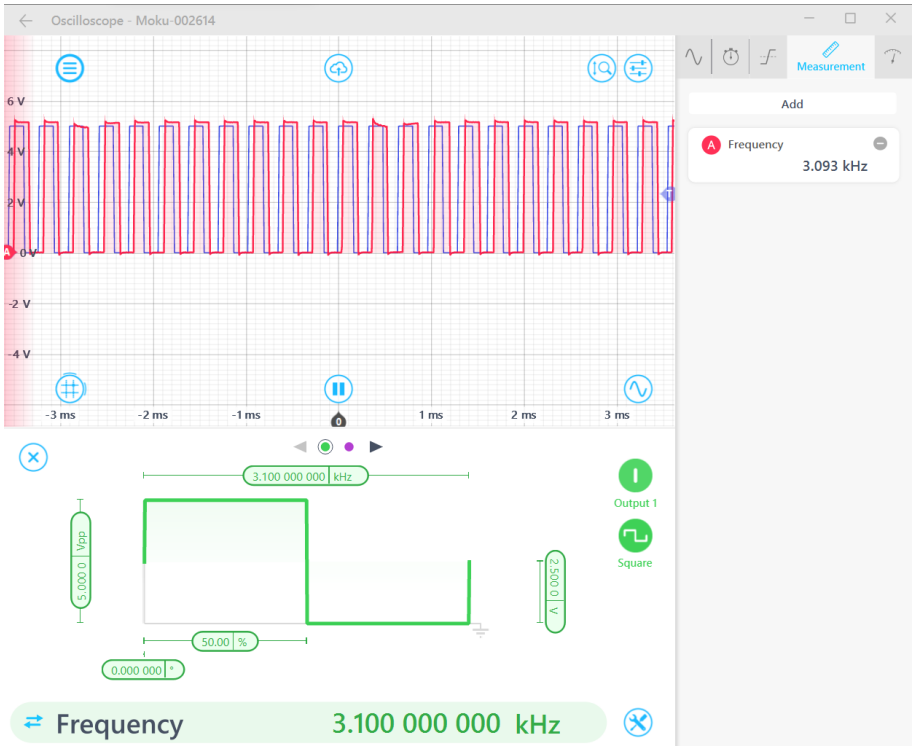

Figure 3.7: **First case limit**. We set a measurement for a prescale of 32 and with a square wave of 3.1kHz. On top right, the frequency of the red signal (Arduino's response to the blue signal) is measured.

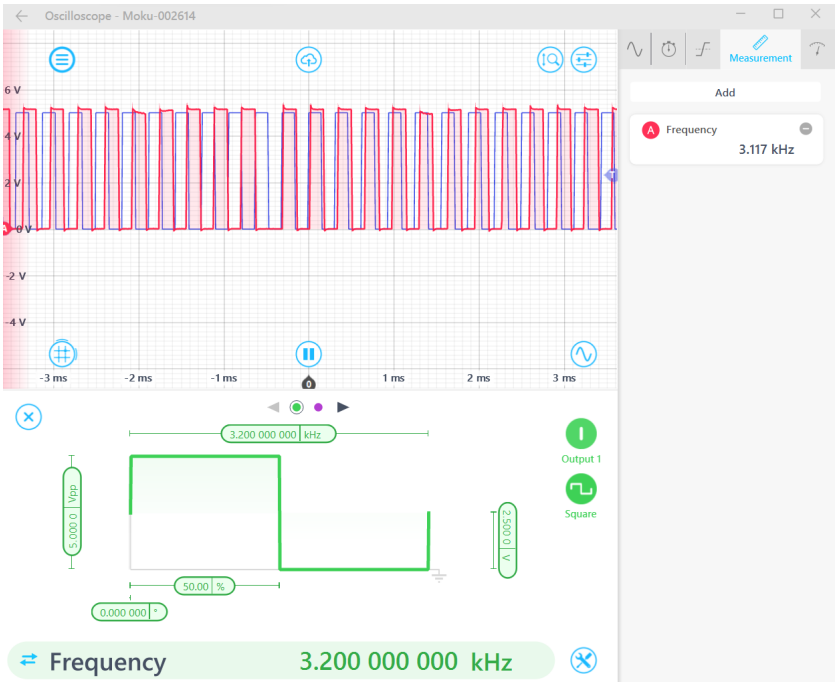

Figure 3.8: **First Case Failure**. The measured frequency didn't reach 3.2kHz, the frequency of the sent square wave.

In the second case, we set the prescale factor to 16, which corresponds to a clock frequency of 1MHz. In figure 3.9, it can be seen how the response frequency reached 3.3kHz, which shows the speed up of the Arduino. Note that 3.3kHz isn't the highest frequency that the Arduino with a 16 prescale factor can respond to. We just wanted to show the speed up as we increase the clock frequency.

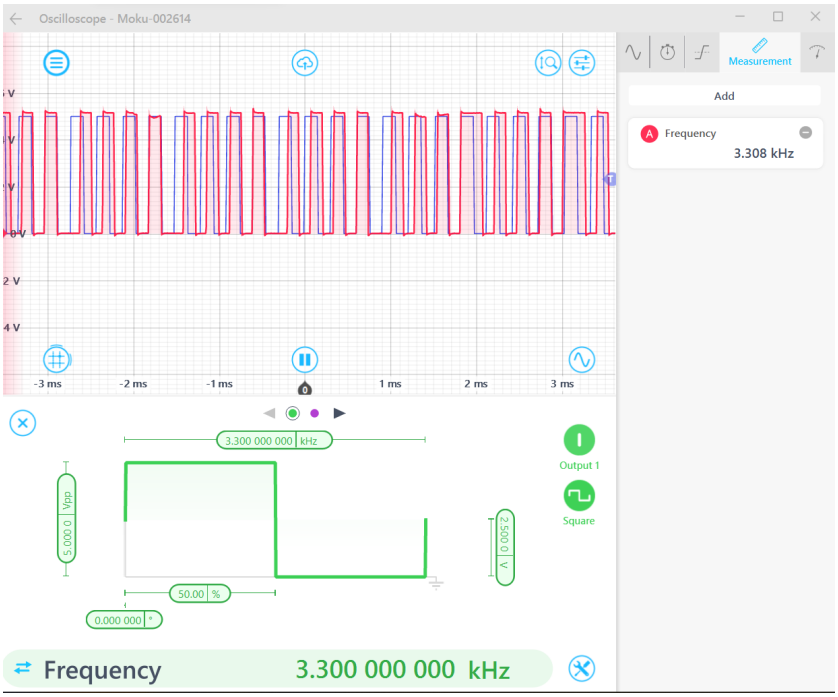

Figure 3.9: **Speed Up in Second Case**. We set the prescale factor to 16 and send a square wave with a frequency of 3.3kHz, which was responded to by the Arduino.

Clock speed vs Precision

Unfortunately, increasing the clock speed comes at the cost of reducing precision. In this test, we show the reduction in precision. Serial.begin() is left to observe the Arduino's measurement value, which can be seen in the right column of figures 3.10 and 3.11. The second input will be measured since it is terminated; it is the easier choice to show the decrease in precision. We will compare between prescale factors of 8 and 16. It can be seen in the first case that the reading is pretty precise by reading all the ones that come out in the COM3 window, which is what the Arduino reads. The one translates nearly to 0V; you can see these ones in the right window of COM3 in figure 9. In the second case, it can be seen that there a lot of other numbers than one. In summary, one should find the right combination between precision and speed when modifying the Arduino for an application.

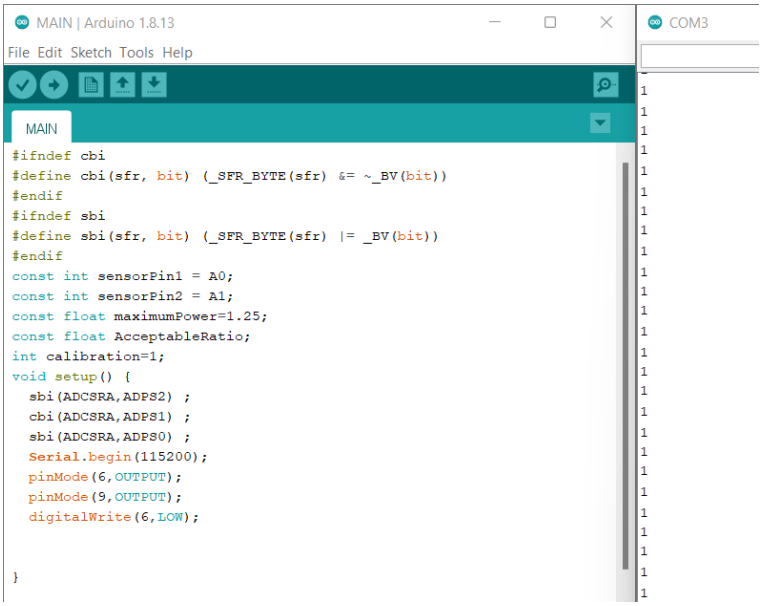

Figure 3.10: **Precision of 16 Prescale Factor**. The read values are on the right of the figure under COM3 while the window shows the code for setting the prescale factor.

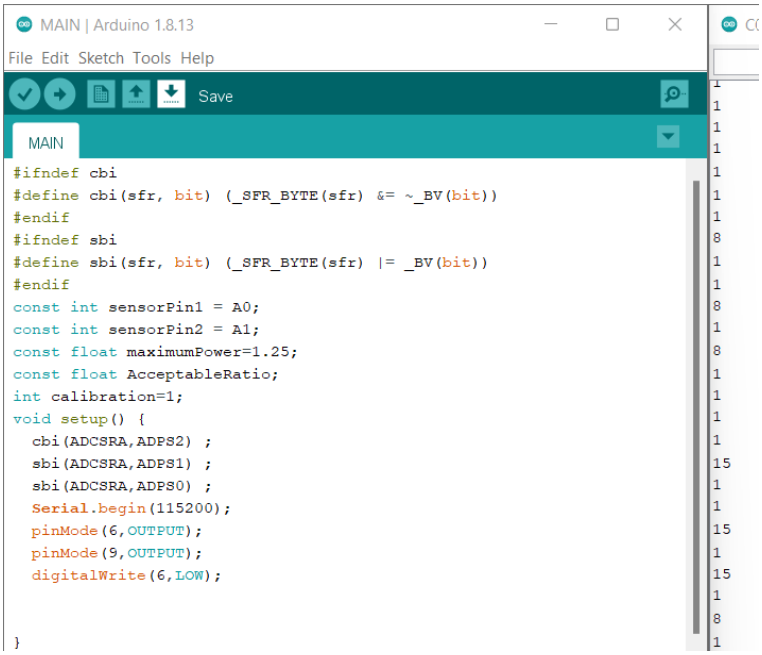

Figure 3.11: **Precision of 8 Prescale Factor**. Readings on the right column are not precise compared to the previous setting.

3.2 AOM Driver

In the introduction, the stages of cooling were introduced, and it was discussed how they all required lasers, which need to be controlled. The circuit that provides such control is the AOM driver. Through sending RF electrical signals, the AOM driver controls the frequency and the amplitude of the sound waves created by a transducer. The transducer's sound waves are sent into a crystal to make it behave like a diffraction grating. The 1st order diffracted light is what we care about; both its frequency and amplitude can be controlled by this driver.

The circuit was designed in the Dysprosium lab in MIT, and we modified it because we needed a greater amplitude range. We increased the dynamical range from 25 dB to 50 dB to have a better evaporative cooling. The range of 50 dB means that you can change the power by a factor of 10^5. Why do we need this much scaling? The reason is that after subdoppler cooling, lithium would have a temperature in the range of 60 μK[60], and this temperature would needed to be cooled down even more to about 10 nK for some experiments. This scaling is about 10^4, but a scale of 10^5 gives some buffer for the nonidealities in the lab.

Another modification is the addition of an external RF port such that we can use external RF sources to send signals. The advantage of having an external source is that it would have lower phase noise. Such stability and precision will allow creating lattices for atoms.

In this section, the theory behind the AOM's control on the laser and the modifications done to the circuit will be explained. Finally, we will discuss the results.

3.2.1 AOM's Control on Light

The whole system consists of two devices, the AOM and the AOM driver. The acousto-optic modulator (AOM) is a device that controls the frequency and amplitude of light. The device consists of a crystal and a transducer that sends sound waves through the crystal. On the other hand, the AOM driver controls the frequency and amplitude of these sound waves; it does that by sending an RF signal to the transducer so that it creates a sound wave with a frequency and amplitude equal to those of the RF signal. In summary, there are three kinds of waves. The first kind is the RF electrical signal sent by the AOM driver

to control the sound wave of the transducer. The sound wave, which is the second type, controls the third type of waves, the laser.

The AOM depends on the acousto-optical effect, where the compressions and the rarefactions caused by the sound waves alter the index of refraction of the crystal. It can be understood from its analogy to the Bragg diffraction, which explains the x-ray diffraction in crystals. In Bragg diffraction, the light waves hit planes of atoms that constructively and destructively interfere as they get reflected from these planes of atoms. Unlike the discontinuous change in density that are caused by the atomic planes, the sound waves are sinusoidal functions that provide continuous changes in the density; however, the same treatment of how the waves interfere can be applied. The diffracted angle is given by $\sin\theta = (m\lambda/2\Lambda)$, where λ is the light's wavelength, and Λ is the acoustic wavelength. You can get a general sense of the AOM from the figure below.

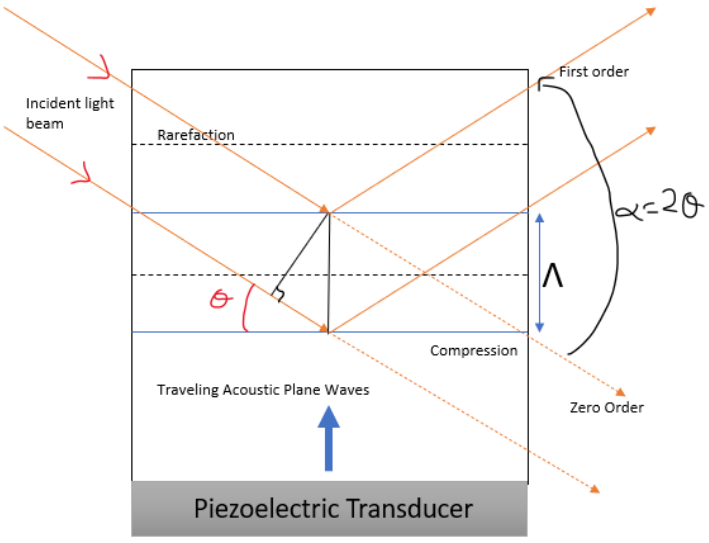

Figure 3.12: **Diffraction of Light**. The first-order diffracted light is created as the incident beam travels through the AOM. [52]

Other than the angle of diffraction, the amplitude of the diffracted beam is controlled by the amplitude of the RF signal sent by the AOM driver. Recall that the amplitude and

frequency of the RF signal are as the same as the ones of the sound wave. Frequency can also be controlled since the sound waves are moving unlike the atomic planes, which are at rest. The frequency gained is equal to the frequency of these sound waves; you can think of it as a Doppler shift that results from the light hitting periodic barriers moving at the same speed of these waves.[52][53] The AOM that we use is G&H AOMO 3200-1214.

3.2.2 RF Basics and modifications on the circuit

First Modification

To understand the first modification of the circuit, it is important to understand what a mixer is and how it is used in the circuit. A mixer is a three-port component that modulates frequencies by multiplting input signals; it usually has the cross symbol as seen in figure 3.13. The three ports are called LO, IF, and RF. The LO (local oscillator) is always an input. The second input out of the IF and RF is chosen based on the application.

Figure 3.13: **Mixer**. Shown is the basic symbol of the mixer [54]

To see how it works, suppose you have two signals $S_1 = A\cos(\omega_1 t + \phi)$ and $S_2 = B\cos(\omega_2 t)$. If you multiply both of them and use the product sum rule:

$$S_1 \cdot S_2 = \frac{AB}{2}(\cos[(\omega_1 + \omega_2)t + \phi] + \cos[(\omega_1 - \omega_2)t + \phi])$$

The purpose of the mixer is to be able to modulate the signal while preserving properties like its phase, which is unchanged in the product formula. Choosing IF or RF as the second input determines if the modulation is upconversion or downconversion. In upconversion, LO and IF are the inputs, which output two signals with the sum and the difference as their frequencies: $f_{rf1} = f_{lo} - f_{if}$ and $f_{rf2} = f_{lo} + f_{if}$. It is known as an upconversion for the following reason. The frequency of LO is usually much higher than that of IF, which results in two frequencies greater than that of IF. It is a downconversion when LO and RF are used because the IF would have a frequency equal to the difference of the inputs'

frequencies and lower than both of them $f_{if} = |f_{lo} - f_{rf}|$. Both cases can be seen in the figure.[54][55] Since the IF is used for outputting low frequencies, usually you would find in mixers that the IF's bandwidth allows lower frequencies than the RF's bandwidth; DC signal can be an input and output of the IF port but not for the RF port.

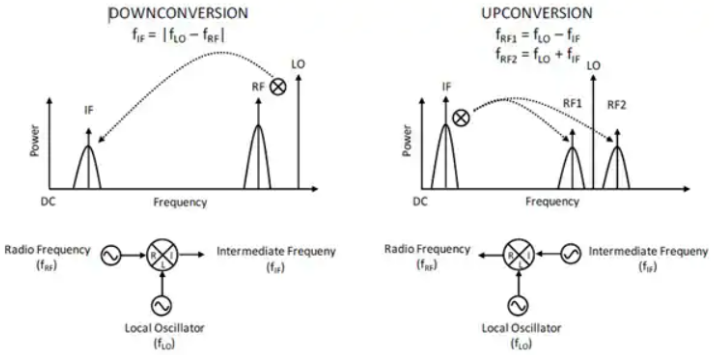

Figure 3.14: **Downconversion and Upconversion**. The processes of downconversion is shown on the left, and the upconversion process is on the right. The figure is taken from ref [54].

After understanding the mixer, its functionality in the circuit will be explained. It is used to scale the RF signal that comes out of the VCO (voltage controlled oscillator), an RF component that outputs an RF signal with a frequency depending on the voltage applied. The mixer scales the signal without changing its frequency by using a DC voltage in the IF port while the VCO signal is sent to LO. It results in a signal that is the multiplication of the DC value to the signal.

The operation of the mixer is just a part of the whole story. The missing part that will help in understanding the first modification is the mixer's isolation. When the DC signal is turned way down to 0V, there would still be some signal passing through because of the non-ideal isolation. The isolation of our mixer ADEX-10H is 55 dB between RF and LO when IF is terminated at 50Ω. This isolation is specified for signals between 100 MHz and 500MHz, which means that RF will have a a power of -55 dBm if LO was at 0 dBm. Our first modification was to add another mixer so that less signal passes through due to a higher isolation from the two mixers. However, by adding another mixer as can be seen in the printed circuit board(PCB) of figure 3.16, the dynamical range of 50 dBm that we wanted was not reached. One additional mixer increased the dynamic range from the

reported 25dBm to 37dBm. Figure 3.15 shows the older PCB design[1] with one mixer.

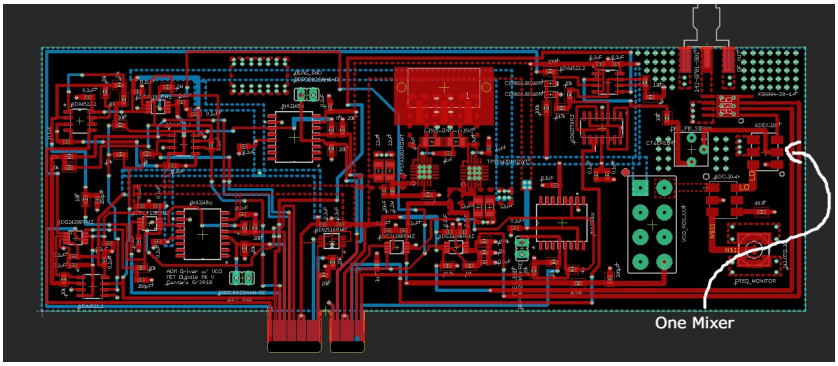

Figure 3.15: **Original Design**. Only one mixer was used in this circuit.

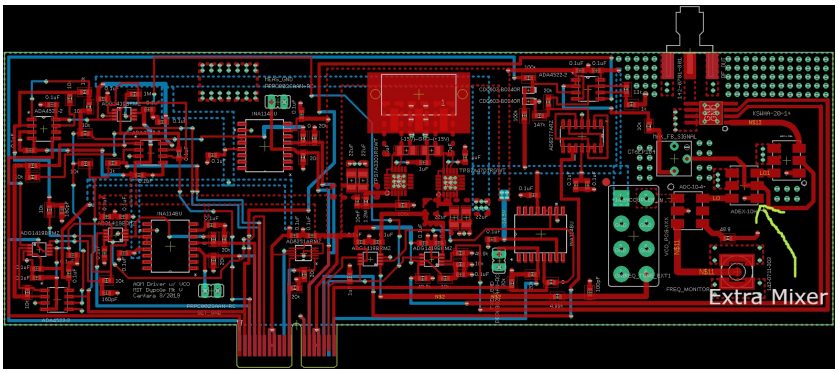

Figure 3.16: **First Modification Design**. It can be seen that an extra mixer was added.

Second and Final Modification

The second modification depends on a basic concept of RF electronics; it is the concept of treating RF signals as waves. By waves, I mean that impedance matching between two points is important since the impedance is analogous to the index of refraction. Incorrect matching of impedance may lead to reflections of your signal. To think of the modification, our next task was to learn how to make sure that our traces in the circuit are 50Ω, which was done by considering two points. First, the routing of the traces in a PCB need to avoid right angles. To have the ideal paths, the traces should be curved from one point

[1]The software used for the design is Eagle.

to another in a way that the radius of curvature is at least three times larger than the trace width. The curved traces in the final design of the circuit can be seen in figure 3.18. Second, we needed to know how to calculate the impedance of our traces. We did that using the calculator on PCBway and modified our circuit to match that. The thickness of the board, the width of the trace, and the height of the trace are all factors that affect the impedance. Figure 3.17 shows the parameters of a microstrip, which is a certain way to manufacture traces. Note that a PCB may have different layers; one of them can be a fixed voltage or ground. The thickness parameter is usually the distance between the trace and the adjacent layer with a fixed voltage.

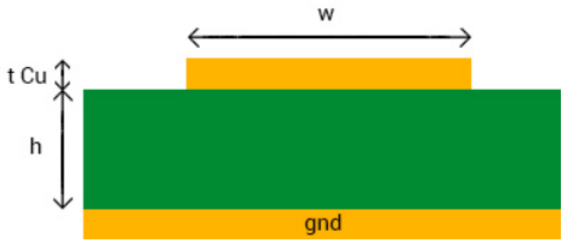

Figure 3.17: **Microstrip Trace**. One of the possible ways to create a PCB trace. The variable h is the height of the dielectric between the trace and the ground. The variable w is the trace's width, and the t Cu is the trace's height. The figure is taken from ref [57].

Some details should be discussed about how we designed the board. One of the problems that we faced from the first modified circuit was that we needed a thicker board to better fit the PCI connector on our faceplate. First, we thought about simply increasing the board's thickness; however, the impedance increases as the thickness increases. The only way to effectively change the impedance after changing the thickness is to change the width of the trace. Given the default parameters of PCB way for the dielectric constant and track height, a thickness of 2mm will need about 150mil width for the traces, which is insanely big. The other solution was to make a 4-layer board. Luckily, it was common practice in RF PCB design to make the transmission lines and electronic components on the first layer while the ground on the second layer. Having the ground on the second layer made it easier to have the right impedance with a relatively good width. In our case, the board had a full thickness of 2mm, and the width of the traces is 13mil. We asked PCBway also to make sure that our design had a 50Ω impedance. You can compare the physical board to our design in figures 3.19 and 3.18, respectively. The RF part is highlighted inside a box.

Another thing to consider when designing an RF circuit is to minimize coupling and parasitic inductance. To start with, the coupling increases as the lines get closer to each other and the more parallel they are. We tried our best to make the RF lines as far apart from each other and to avoid parallel lines. For the parasitic ground inductance, we added multiple vias in the RF portion of the circuit between the top layer and the ground on the second layer and fourth layer. The vias help not only in preventing parasitic inductance but also in RF coupling between lines. The fourth ground layer was added because we thought that it may give some EM shielding.[56][57]

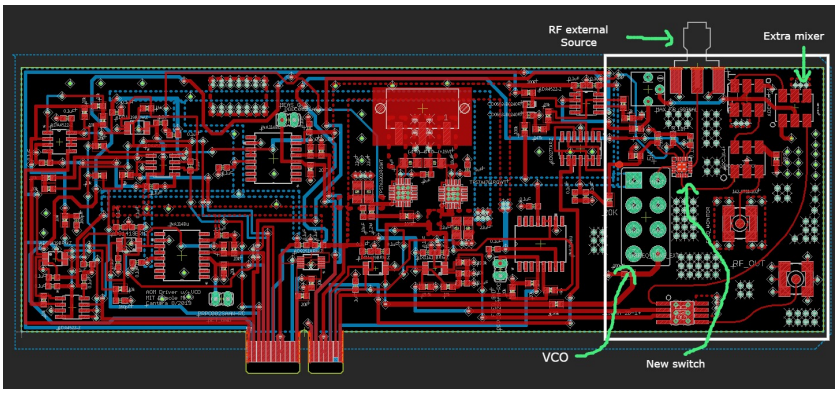

Figure 3.18: **Final Design**. The box contains the circuit's RF part. An RF switch and an SMA for the external RF source are added. The extra mixer was also kept.

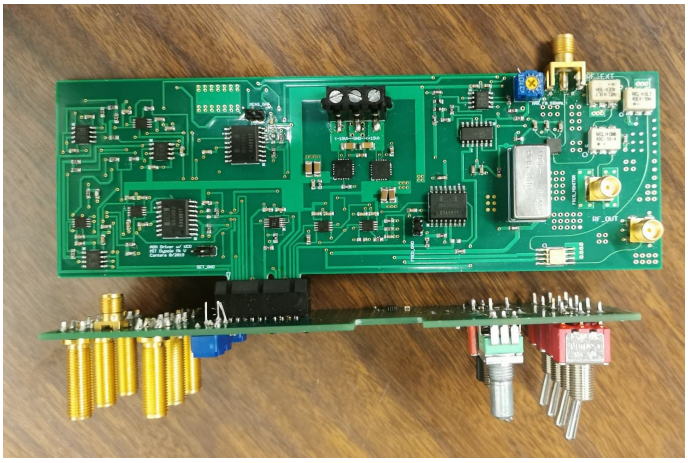

Figure 3.19: **Physical Circuit**. The physical circuit is shown for comparison to the software's design. The attached circuit below is the faceplate used to control the driver circuit.

An Extra Feature

In our circuit, we wanted to be able to drive our AOM with an external RF signal source with low phase noise. One of these external sources is the Windfreak's SynthHD Pro. The main reason is that usually the linewidth of our signal is more stable and precise in the Windfreak; the difference will be shown in the results section. This feature also would enable us to have a greater range of frequencies that can be used (10MHz to 24GHz[2] for the Windfreak) than what the VCO can supply. Our VCO is a POS-300+ from mini-circuits and is designed to have a linear tuning from 150MHz to 280MHz.

To do that we simply added a switch, which is an HSWA2-30DR+. This switch has an operating range from DC to 3000MHz and an isolation between 44 and 64dB depending on the frequency. With such a switch, we were able to use an external RF signal; you can see the switch and the external signal port in figure 3.18.

3.2.3 Results

In this section, the results of the dynamical range and the linewidth of our circuit will be shown. Our circuit is tested by measuring the signal using a spectrum analyzer. The

[2]The coupler and mixer can withstand up to 1000MHz, so 1000MHz would really be the threshold here

circuit is powered by a voltage of ±15V. Furthermore, the circuit is made of two parts: a faceplate for control and the main AOM driver, which includes all the RF and electronic components. On the faceplate seen in figure 3.20, two potentiometers are responsible for the signal's amplitude and frequency, and the middle switch shifts between internal RF signal (VCO) and the external RF signal (Windfreak). The rest of the switches and potentiometers are related to other technicalities and a feedback loop that works well from the original circuit and is beyond the scope of this section.

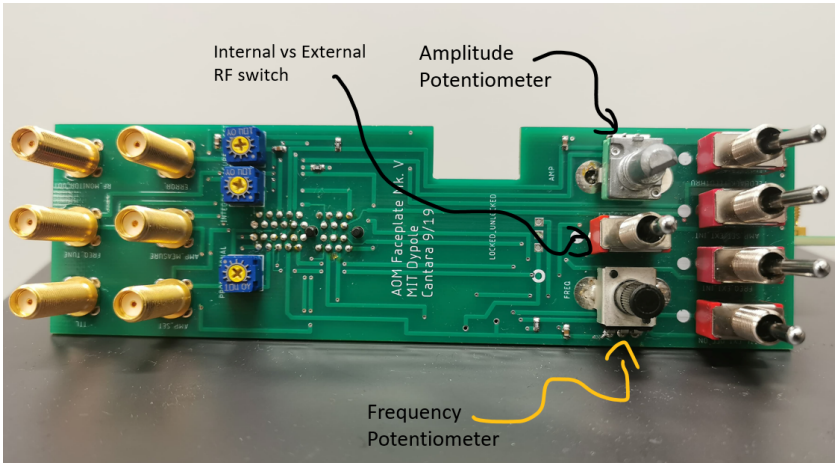

Figure 3.20: **Faceplate**. The AOM driver's faceplate that contains the potentiometers used to control the frequency and amplitude of the signal and a switch to exchange between RF external and internal signals.

Dynamical Range

The main purpose of the modification is to increase the dynamical range. After the first modification, it can be seen that the dynamic range is about 37 dB. In the original design from MIT, it was about 25 dB. For the second modification, it can be seen that a dynamic range of about 57 dB is reached, which is indeed more than what we wanted. The test was done using the internal RF signal, not the Windfreak.

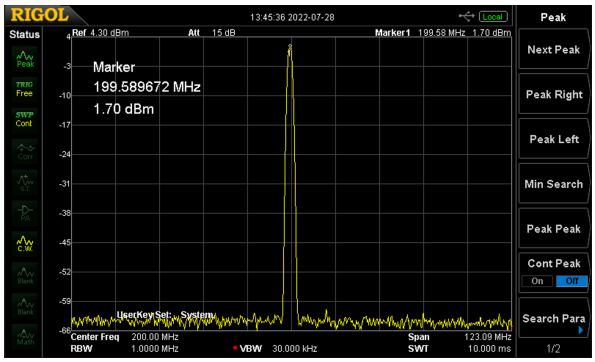

(a) Highest Power

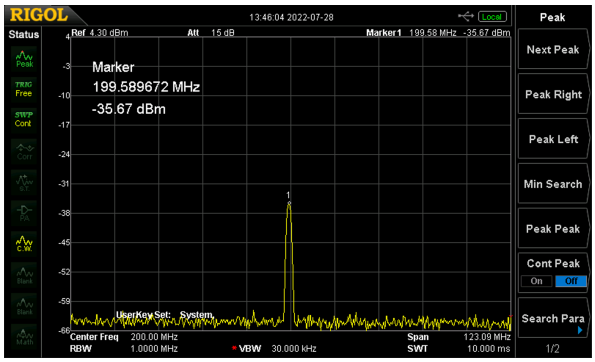

(b) Lowest Power

Figure 3.21: **Dynamic Range of the First Modification**. A dynamic range of 37.4 dB is seen for the first modification. The highest power is 1.7 dBm, and the lowest one is -35.7dBm.

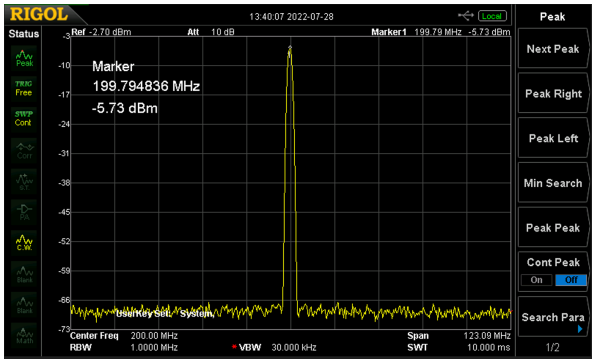

(a) Highest Power

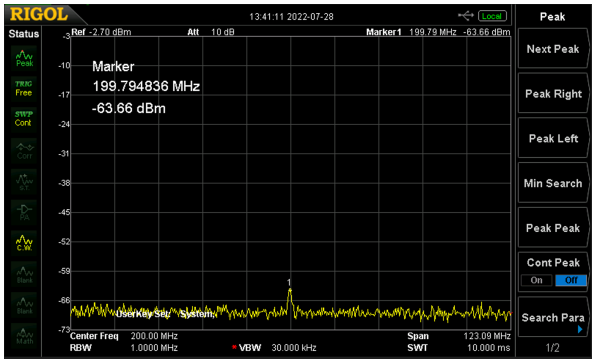

(b) Lowest Power

Figure 3.22: **Dynamic Range of the First Modification**. A dynamic range of 57.9 dB for second modification: the highest power is -5.7 dBm, and the lowest one is -63.7 dBm.

Linewidth

Besides the extra range of frequencies not provided by the VCO, the main advantage of the WindFreak, our external RF source, is the narrower linewidth and better carrier stability. Linewidth is the width between the two frequencies, at which half maximum of the amplitude is achieved. The linewidth of both the VCO's signal in the circuit and the external signal will be measured.

Before any measurement, it is important to explain the concepts of resolution bandwidth(RBW) and video bandwidth(VBW) in a spectrum analyzer since these were used to measure the linewidth. RBW (Resolution Bandwidth) is the ability to distinguish between two frequencies of the same amplitude. Figure 3.23 gives a helpful example.

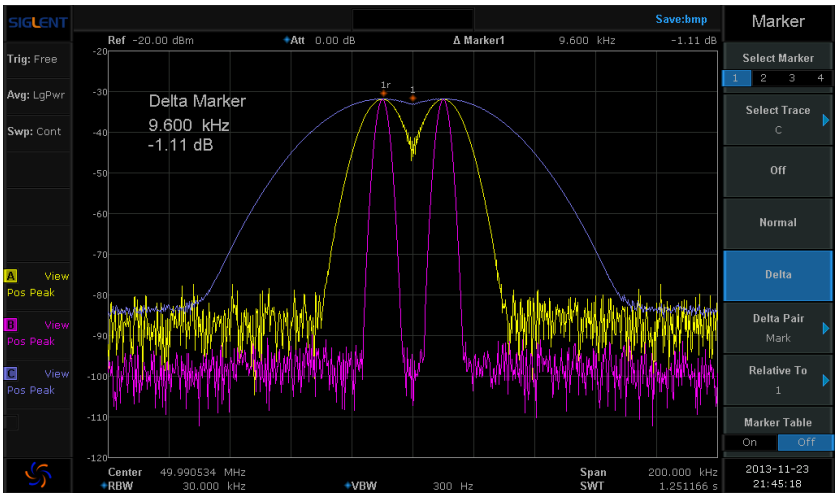

Figure 3.23: **RBW Illustration**. All signals are separated by 20kHz. RBW for blue is 30kHz, for yellow 10kHz, and for pink 3kHz. The lowest RBW has the best distinction of the two signals. The figure is taken from ref [59].

The two signals are separated by 20kHz; the RBW in the graphs are 30kHz, 10kHz, and 3kHz, which are represented by blue, yellow, and pink, respectively. For the blue case, the two frequencies are seen as one since the RBW is larger than the difference between them. The distinction becomes clearer as the RBW decreases; the pink signal has a better resolution than the yellow one. An interesting detail is that the noise floor decreases as RBW decreases. On the other hand, VBW's main effect is to clean up the signal from the noise fluctuations by taking its average because it acts as a time-domain low-pass filter

after taking the measurement. It is usually used to detect small peaks by smoothing down the fluctuations.[59] In summary about the noise, decreasing RBW lowers the noise floor while the VBW lowers the fluctuations of the noise. Now, in our measure of the VCO's signal, the lowest RBW where we had a stable signal is 300Hz while the VBW is 10kHz. It is stable in a sense that we can get a clean good signal because VCO's signal usually keeps drifting. We froze the signal to measure the linewidth, which is about 330Hz in these settings. The linewidth of 330Hz is just above the resolution available, which means that the VCO might have a better linewidth measurement. However, it is difficult to obtain this more accurate measurement because the signal isn't stable at all for a lower RBW.

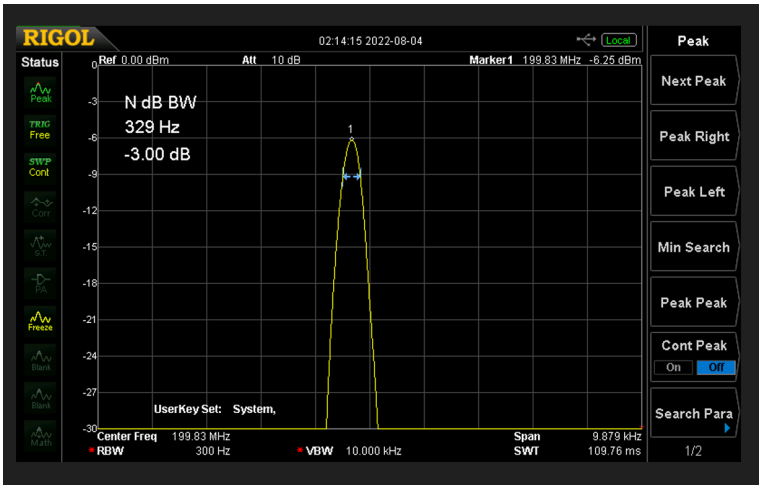

Figure 3.24: **Linewidth of VCO**. it is 329Hz for a 300Hz RBW, 10kHz VBW, and a span of about 10kHz.

For the Windfreak, we can measure the linewidth at 10Hz for both RBW and VBW; you can see the parameters at the bottom of the spectrum analyzer screen. Unlike the VCO's signal, the Winfreak's signal didn't drift at all. In these settings, the linewidth is 12Hz in a span of 200Hz. A linewidth of 12Hz for a 10Hz RBW means that the Windfreak may have even a better linewidth. This shows that the windfreak is more precise and also more stable.

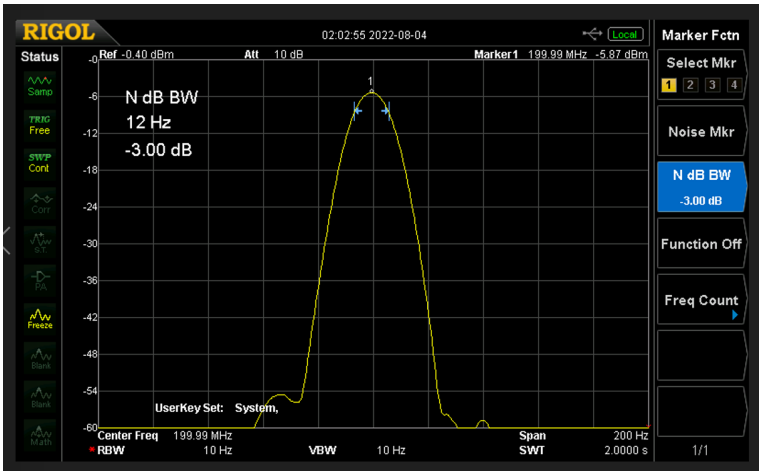

Figure 3.25: **Linewidth of Windfreak**. it is 12Hz for 10Hz RBW and VBW and a span of 200Hz.

3.3 Current Driver

As was seen in the general outline of cooling the atoms, the first step is to use a Zeeman slower, which has a specific coil configurations and a certain constant current. Having a constant current can be a challenge, and this challenge needs to be overcome since it will be faced in many other applications as well like the Feshbach coils and the 2D MOT, which are future projects. Why is having a constant current considered to be a challenge? The reason is that parameters determining the current change over time. For example, current heats the wire, and the heating changes the resistance, which leads to increasing the voltage to have the same current. Another factor is the relaxation of parameters in some electronic components over time.

Given these reasons, a current controller is needed to adjust to the changes happening. The best way to deal with changes of a signal is through feedback loops, so this circuit is about implementing two feedback loops to change two different variables of the system. The system is made of a sense resistor, a power supply, and a MOSFET. Of the two feedback loops, one changes the MOSFET's gate voltage to control the current, and the other feedback loop controls the voltage of the power supply to control the heat dissipated.

One might argue that using a current source is simply sufficient to have a constant

current independent of the resistance of the load instead of going through the trouble of building a current controller. The problem of using a current source is that it is also a source of noise. On a different note, we need a current source that can be controlled digitally, which we would have from the setpoints of the feedback loop. In this section, we will talk about MOSFETs and PI control. After understanding these building blocks, we will explain our design and show results. We use the Vishay SOT-227 MOSFET, so we will always refer to its paramters when we explain the MOSFET.

3.3.1 MOSFET

Background

A metal–oxide–semiconductor field-effect transistor (MOSFET) is the first building block since the current is mainly controlled from this device. It is a semiconductor device with three ports: drain, source, and gate; the ports are shown below in the simplified electrical symbol of a MOSFET. Without jumping into the deep details, understanding the reason behind the names of the ports will give a good enough understanding of how the MOSFET operates. The names source and drain are named for the reason that the electrons typically flow from the source to drain, which means that the current flows in the opposite direction from drain to source. This implies that the source usually has the lower voltage of both ports, so we will always assume that it is at ground. The voltage between the drain and source will be denoted as V_{DS}. The name gate comes from the idea that a MOSFET doesn't conduct current until a voltage is applied to the gate; in other words, the voltage opens the gate for the current to flow. It is important to know that the gate-source voltage V_{GS} must exceed a certain threshold voltage V_t to allow current to flow. In our MOSFET, the threshold is typically 2.9V; it can be between 2.2V and 3.8V. Note that our MOSFET is an n-type, which needs a positive gate voltage to allow current to flow. On the other hand, a p-type needs a negative voltage.

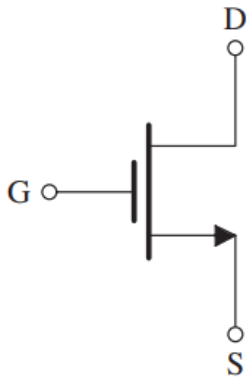

Figure 3.26: **MOSFET**. n-type MOSFET Symbol. The figure is taken from ref [58].

Next thing to consider is what will be the relations between the current flowing, V_{GS}, and V_{DS} because these relations will explain our choice of parameters. Instead of V_{GS}, the overdrive voltage $V_{OV} \equiv V_{GS} - V_t$ is the value of interest since current will be conducted only if $V_{GS} > V_t$. The relations of the three variables can all be summarized in the following graph, where V_{OV} is held fixed.

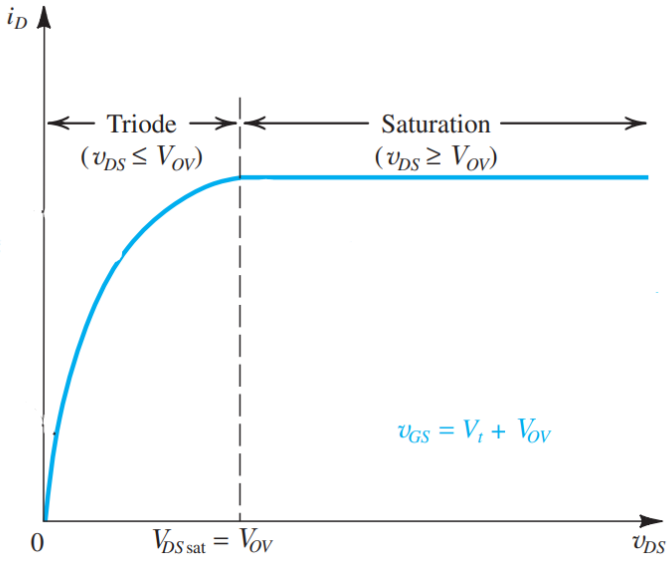

Figure 3.27: **Current vs** V_{OV}. A linear relation exists for low V_{DS}. For $V_{DS} \geq V_{OV}$, the current enters a saturation regime. The figure is taken from ref [58].

At a very small V_{DS} compared to V_{OV}, there is a linear relationship between the current and the voltage as if the MOSFET acts as a normal ohmic resistor; however, the linearity starts breaking as it increases. As it increases past V_{OV}, the current saturates and doesn't increase anymore; in other words, the resistance of the MOSFET increases as V_{DS} increases to keep the current constant. Here is something that needs to be noted about the design, V_{DS} should be chosen such that it is just above V_{OV} because the current would be the most stable at that state resulting in a stable magnetic field. Furthermore, it needs to be just above V_{OV} and not way higher than that because such a higher voltage will waste power and heat the MOSFET for no good reason. Remember $P = VI$. Finally, decreasing V_{OV} while maintaining the condition of $V_{DS} > V_{OV}$ will decrease the current but will remain in the saturation regime.[58]

Design

After understanding the operation of the MOSFET, it is time to discuss factors related to our design. There are two voltages that need to be specified in our system. The first voltage is V_{GS} supplied by one of the feedback loops. The other voltage is V_{DS}. This voltage will also be controlled by one of the feedback loops. Depending on the graph shown below for the MOSFET we are using, we need to choose a certain V_{DS}, at which we keep our MOSFET, so that the maximum V_{GS} gives us that largest current we want. We estimated that we will start with a range of 50A to test our circuit; the 50A range is a good range for not using water cooling. Since we have three plots for different temperatures, we decided to use the 25C plot because our lab will be temperature controlled at 22C. We think that this temperature would ideally be achieved by water cooling the circuit if we decided to have much higher currents. As a result, 4.2V is the voltage chosen. Even without using water cooling, a 50A will give a power of about 200W, which will increase the temperature of the MOSFET for a thermal resistivity of 0.23 by $0.23 \cdot 200 = 46$C. The temperature will be less than 100C, which is our rough estimate for using water cooling; consequently, we can use a heat sink that cools the 46C down to 22C through convection. If we found out that working with high currents needed less V_{GS}, it will be easy to change the setpoint volatge in our circuit.

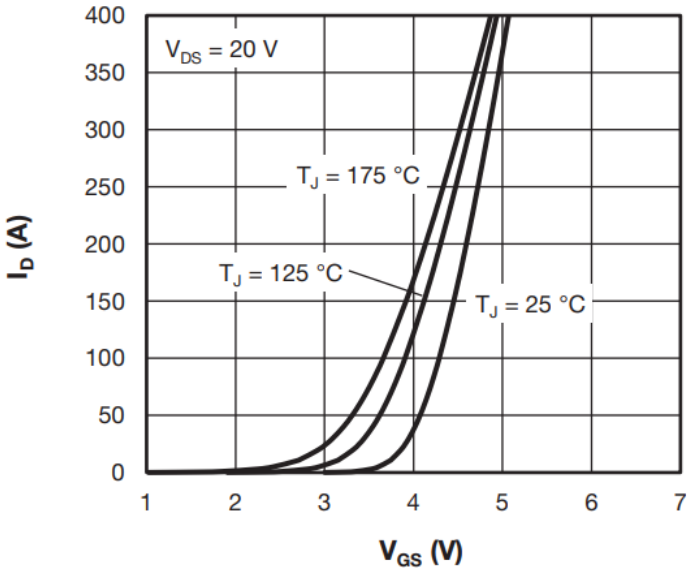

Fig. 5 - Typical Transfer Characteristics

Figure 3.28: **Current vs V_{GS} at different temperatures**. The graph is taken from the datasheet. The voltage V_{DS} is held fixed at 20V.

3.3.2 PI control

We stated that we will need two feedback controllers. One will control the gate voltage for modulating the current and, therefore, the magnetic field. The other one is to control V_{DS}. The voltage V_{DS} is controlled to keep the heat dissipation low. One way to perform the feedback loops is by implementing a PI control, which can be described by the following diagram.

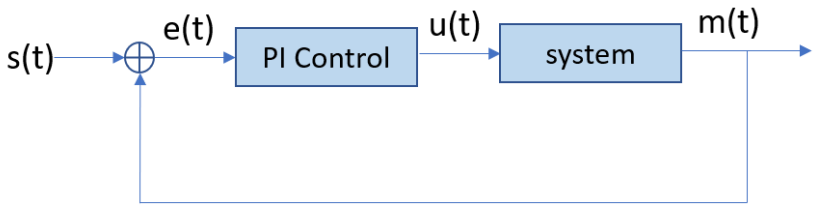

Figure 3.29: **A General Schematic for a Feedback Loop**. s(t) is the setpoint, m(t) is the measurement, and e(t)=s(t)-m(t) is the error signal. The signal u(t) is sent to the system after e(t) is processed in the feedback loop.

A system sends an output depending on the input signal it is receiving. For example in a MOSFET with a fixed V_{DS}, the gate voltage is the input while the current is the output. In the graph above, the input signal is $u(t)$. The measured output signal is $m(t)$, which can be any value indicating the current in our example. As will be seen, we measured a voltage difference across a resistor to know the current. The goal of the PI feedback loop is to control $u(t)$ so that the measured value $m(t)$ matches the setpoint value $s(t)$ that we choose. In our same example here, the setpoint sets the wanted current. When there is no feedback loop, the setpoint becomes equal to the input signal $s(t) = u(t)$; this process is known as the feedthrough. In case of a feedback, the setpoint gets processed to be a input signal.

The PI feedback sets the measured value $m(t)$ by controlling the signal $u(t)$. This input signal is controlled based on the error signal $e(t)$, which is the difference between the setpoint and the measured value $e(t) = s(t) - m(t)$. How the PI control exactly responds to the error signal is described in the following equation:

$$u(t) = \left(k_p e(t) + k_I \int_0^t e(\tau) d\tau \right) \tag{3.1}$$

The constant k_p is the proportional gain constant, and k_I is the integral constant. The role of each term in this equation will be explained in the following sections.

Background

Proportional

Proportional gain is the first term of equation 2: $u(t) = k_p e(t)$. The integral term will be ignored to understand the role of the proportional term alone; in other words, $k_I = 0$. Assuming k_p is positive, the feedback loop tends to increase the signal $u(t)$ when the difference or error is positive indicating that the measured value is lower than the setpoint; in other words, the feedback loop increases $u(t)$ to decrease the error. In contrast, the proportional part will decrease the signal when the error is negative.

The proportional control has some characteristics. One of them is that the steady-state of the measured system will be at an offset from the setpoint. Without an offset, the measured value will be equal to the setpoint resulting in a zero error and therefore a zero $u(t)$ that will never drive the system. Another characteristic is the rise time that tends to decrease as the proportional gain increases because the error will already be large and scaled to be larger once the feedback is started. A larger k_p will decrease the rise time but may also result in an overshooting in the start of the feedback if it was large enough. Finally, the larger the proportional gain the more time it takes until the oscillations dampen out because of its high response to even small changes. In summary, k_p has different effects that can be seen. As k_p increases, the rise time decreases, the overshoot may result, the offset decreases, and finally the oscillations increase to reach a steady-state[61]. Figure 3.30 shows some of these characteristics.

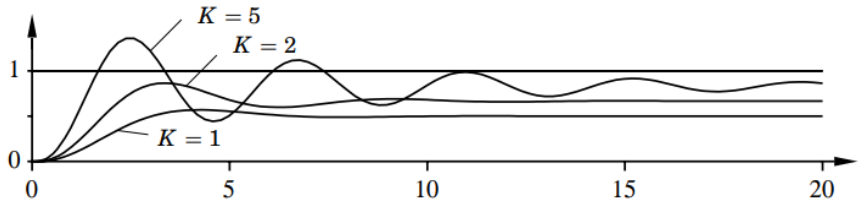

Figure 3.30: **Different Proportional Gains**.Reaction of different proportional gains to a sudden change (y=0→y=1) that starts at t=0 (x-axis). The figure is taken from ref [61]. There is a clear overshooting for $k_p = 5$, and it also oscillates for a longer time until it reaches a steady state. It can also be seen that $k_p = 2$ has a shorter rise time than that of $k_p = 1$.

Integral

After understanding the proportional-only control, it is time to understand the effect of an integrator. The main result of an integrator that it removes the offset produced by the proportional part of the feedback. From equation 2, the integration of the feedback keeps memory of the error and keeps adding it each time until the error reaches zero. Increasing k_I tends to increase the oscillation until it reaches the steady-state.

A popular main problem about the integral gain is the wind up phenomenon. Since the integral part is a continuous summation of the error, the error might be so large that it drives the system to its limit. If the limit doesn't change the sign of the error, then the error will keep growing non-stop; this never ending growth of the error is known as wind up. The problem was solved in our circuit by the ability to make $k_I = 0$ and therefore to restart the integrator [61].

Design

Proportional

The design of the proportional part of the feedback controller was taken from the AOM circuit. It was simply an opamp that has a variable scaling. You can see the design in figure 3.31.

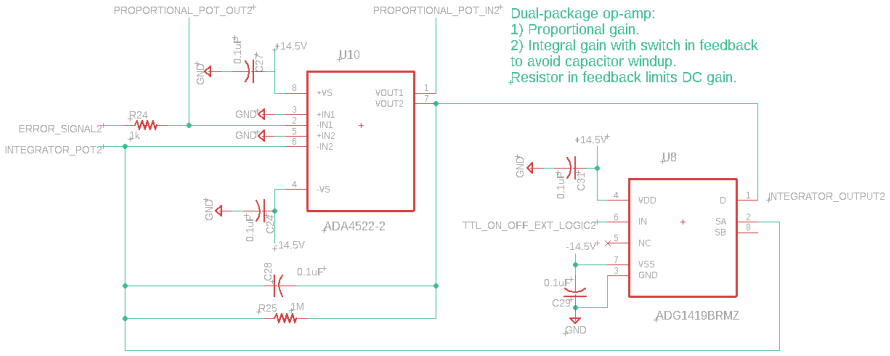

Figure 3.31: **Proportional and Integral Parts of the Circuit**. Component U10 is an opamp used for the proportional and integral gain and connected to a switch to avoid the wind up of the integrator.

As you can see, a dual-package opamp was used for the proportional and the integrator part of the feedback control. Focusing only on the proportional part of component U10, you can see that the error signal passes through a 1kΩ resistor "R24" to the negative input "-IN1" of the first channel of the opamp. To perform an inverting scaling on the signal, you should connect another resistor between the output "VOUT1" and the negative input "-IN1"; therefore, a potentiometer was connecter between "PROPORTIONAL_POT_OUT2" and "PROPORTIONAL_POT_IN2" to achieve a variable scaling. The end result is the proportional feedback part of the circuit that can have its gain tuned by the potentiometer $K_p = -\frac{R_{pot}}{1\text{k}\Omega}$. To find the best range for a potentiometer, we kept trying which one worked best. For the gate feedback, 10kΩ was good enough.

Integrator

It is well known how to build an integrator using an opamp, and it is exactly how it was done in the AOM circuit. You can see the configuration in the same figure. The error signal goes through a potentiometer, which isn't seen in the figure, to the negative input "-IN2" of the second channel of the opamp, and a capacitor is connected between this input "-IN2" and the output "VOUT2". This configuration alone without the 1MΩ resistor is the integrator configuration. The resulting output is $v_I(t) = -\frac{1}{CR_{pot}} \int_0^t v_{error}(t)dt$. As you can see, it has a gain of $-1/CR$. Note that the R is from the potentiometer, which makes the integral gain tunable. The problem of this configuration is the infinite gain of the DC signal since the capacitor cuts the wire and effectively acts like an infinite resistor for the DC signal. One way to avoid this common problem is adding a high resistor, which is the 1MΩ in our circuit, to provide a path for the DC signal and to lower the infinite gain. Of course, the infinite gain is unpractical; realistically it just means that the output voltage will rail out.

Finally, a switch was added after the opamp so that we avoid the wind up situation explained previously. The whole point of the switch is to short circuit the capacitor and its parallel resistor to discharge the capacitor and to have a zero output. The wind up problem is solved because the discharge of the capacitor will allow the integration to start over without any memory of the error before.[58]

3.3.3 Circuit Design

After explaining the building blocks for our design, it is the time to show how everything is put together. Our circuit's goal as we said before is to control current up to 50A. The

way we would do that is to use a power MOSFET. A power MOSFET works in principle the same way as a normal MOSFET but differs in its design so that it can withstand very high currents. Controlling the gate voltage under a fixed V_{DS} will control the current; keep in mind to make $V_{DS} \geq V_{OV}$ to have the stable regime for your current. As step 1 of our thinking process, we are going to have our current by controlling the gate voltage, so that's our first output to be controlled by the feedback loop. To keep it at the stable regime, we would also want to control V_{DS}. The power supply's voltage is divided upon three components as can be seen in figure 3.32: the MOSFET, the sense resistor, and the load, so the task would be to control the power supply's voltage to achieve the constant wanted V_{DS}. This would be achieved by the second feedback loop. In summary, we need two feedback loops, and the schematic below shows the general idea. In each of the next sections we will talk how we designed the feedback for the gate and the supply.

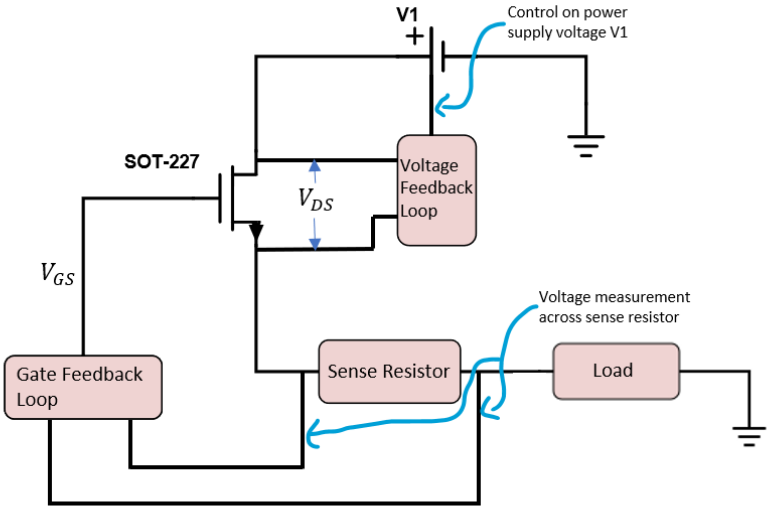

Figure 3.32: **General Schematic for Current Controller**. A MOSEFT is connected to a sense resistor then to the load. The volatge feedback loop measures V_{DS} and controls V1. The gate feedback loop measures the voltage of the sense resistor that indicates the current and controls the gate voltage V_{GS}.

Gate

Design thought

The feedback loop should have two inputs, the measure and the setpoint, and one output, which is the gate voltage. The setpoint determines the current. It is also always compared to the measurement; therefore, we have to decide on the way to perform the measurement. We decided to measure the voltage across a sense resistor; the voltage indicates the current from the simple Ohm's law. Instead of a normal resistor, a sense resistor is perfect for the application since it is designed in a way to withstand high current while keeping its parameters relatively the same because of the low temperature coefficient. A valid question would be how to determine the value of the resistor. It should be chosen to have the best possible precision for the current. The best precision is achieved when the range of current wanted maps to a range of voltage equal to the whole positive supply voltage of the circuit, which is 15V. For example, if we are interested to have a current in the range of no current to 15A, then this needs to map to 15V; therefore, a 1Ω sense resistor is the best one to use $15\text{A} \cdot 1\Omega = 15\text{V}$. In addition to precision, the sense resistor can be chosen to have an easy value for convenience; it makes the mapping from voltage to the current wanted easily done. For example, having 1Ω is better than having 0.85Ω.

For the output, we send a voltage to the gate to achieve the current we want; the voltage would be the $u(t)$ in figure 3.29. Sending the voltage to the gate is more complicated than it seems; the voltage charges the input capacitor of the MOSFET. The input capacitance of the MOSFET is the sum of the capacitance between gate and source and between gate and drain. As a result, our ability to charge and discharge the capacitor determines the bandwidth of the feedback loop. How fast a capacitor gets charged depends on the resistor connected to it as it is known from the common RC circuit. Ideally, a wire with no resistance is the fastest way, but opamps usually have a finite maximum amount of output current known as short current, which can be found in the datasheet. The short current determines the resistor needed; consequently, the resulting RC circuit will determine the bandwidth. Finally, the input capacitor will need to be discharged at some point to decrease the gate voltage, so we connected a pull down resistor to the capacitor as a way to discharge.

Actual Circuit

The actual design can be easily understood from the following sketch.

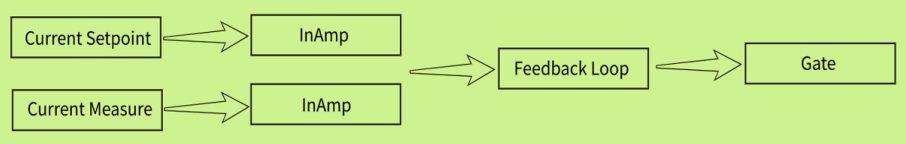

Figure 3.33: **Gate Feedback Schematic**. A schematic for the gate feedback part of the circuit shows how the signal is processed. The signal goes through inamps for ground isolation and processed by a feedback loop before being sent to the Gate input of the MOSFET.

First the setpoint and the voltage measurement across the sense resistor are both sent through an inamp of its own; the inamp ensures that the grounds are separated as was explained before in the interlock circuit. The difference is then sent to a feedback loop that is created using integrators and scaling opamps like the ones in the previous sections. Finally, the output signal gets sent to the gate. A picture of the circuit design is below with the gate part highlighted.

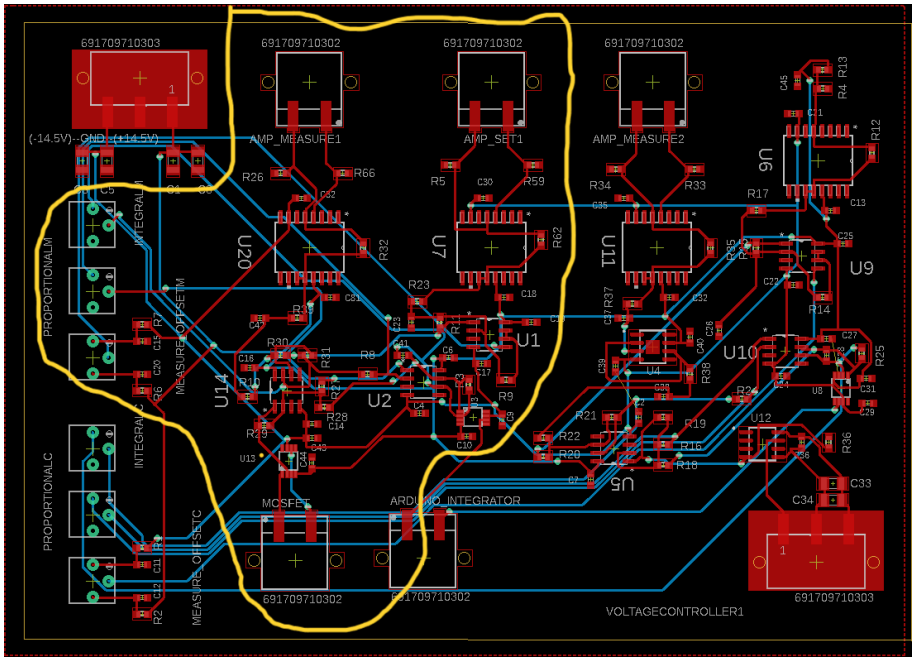

Figure 3.34: **Gate Feedback Part of Circuit**. The gate feedback part of circuit is the highlighted part. On the top you can find two inputs for the measurement and setpoint. At the bottom, there is the output. On the left, three potentiometers are used for the feedback loop. In the middle, you can find the IC components responsible for the proportional and integral parts.

As explained before, the signal charges the input capacitor of the MOSFET and needs to go through a resistor to achieve the maximum short current; this input resistor is not soldered on the board but connected at the output of the circuit before reaching the MOSFET. Determining the resistance requires knowing the short current, which can be known from the opamp's datasheet. The opamp used is OPA2156; it has a short-circuit current of 100mA. Since the circuit is powered by a 15V, the 15V would be the highest rail of the opamp and, therefore, its highest output. As a result, you would need at least a resistor of 150Ω to achieve the maximum allowed short current. The RC circuit created from the resistor and the MOSFET's capacitor will have a time constant that would determine the highest frequency the feedback can respond to. The time constant is $\tau = R{\cdot}C = 150\Omega{\cdot}17.3\text{nF} = 2.6\mu\text{s}$, which sets the highest frequency to $f = \frac{1}{2\pi{\cdot}2.6\mu s} = 60\text{kHz}$. The capacitance value comes from the datasheet of the power MOSFET we are using: SOT-227.

Furthermore, another resistor of about 1.5kΩ is connected from the capacitor to the ground so that it can discharge. Finally, we added a switch for the integrator's capacitor to discharge once we turn it on; this switch is controlled by an Arduino. An arduino introduces a lot of noise, so we are planning to control the IC switch with physical switches.

Results

The main goal of the following test is to determine the bandwidth of our feedback loop. Testing the circuit was done by setting the voltage of the supply to 4.2V. The supply voltage connects to the MOSFET's drain and then to a 1Ω sense resistor. The setup is shown below.

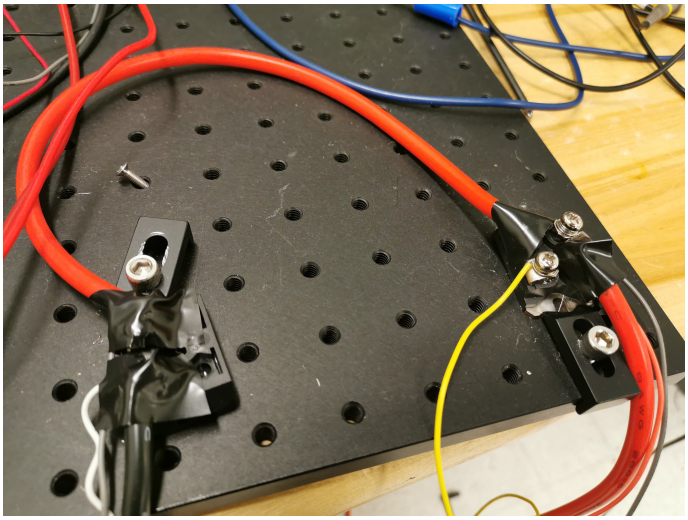

Figure 3.35: **Part 1 of the Current Controller Setup**. Part of the setup for testing the bandwidth of our feedback loop. One can see the Mosfet on the right part of the picture while the sense resistor is on the left.

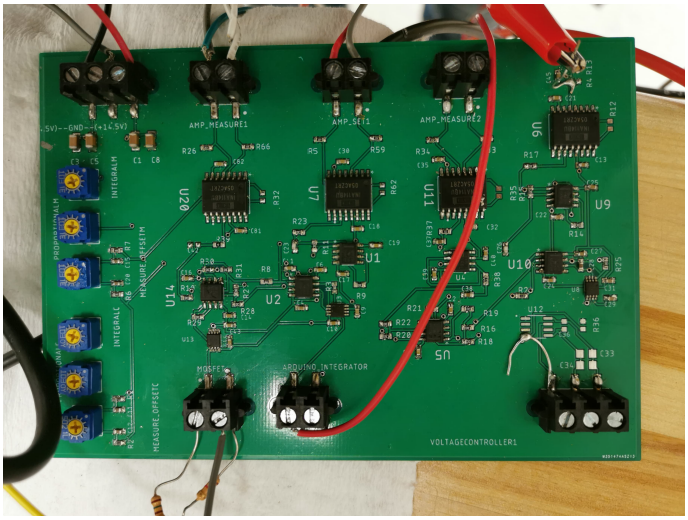

Figure 3.36: **Part 2 of the Current Controller Setup**. The other part of the setup is the soldered current controller connected to the MOSFET and sense resistor.

In figure 3.36, we plug everything to our circuit and measure how good we can match a setpoint frequency. Surprisingly, we were able to reach 91kHz or even a bit more; it is surprising since our cutoff frequency is 61kHz. We set our setpoint to 1V, which means 1A with the 1Ω resistor, and have a modulation of 370mV which is a change of 370mA. You can see the results below with different frequencies.

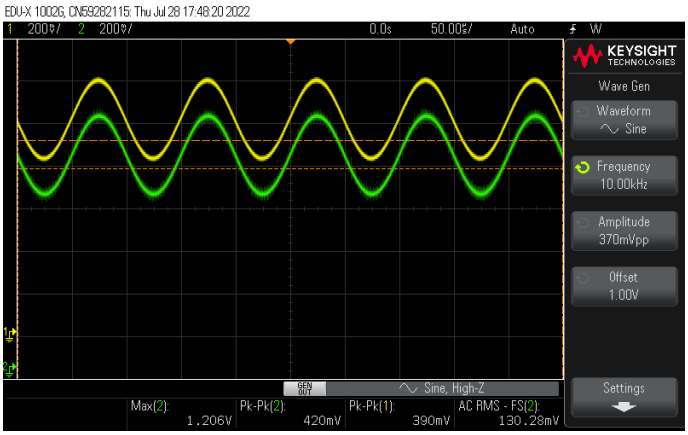

Figure 3.37: **Test 1: Frequency of 10kHz**. Grounds are not aligned on the oscilliscope to show the perfect alignment of both signals.

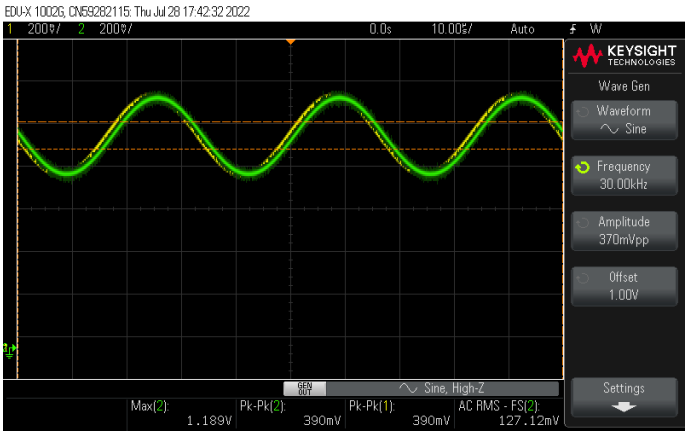

Figure 3.38: **Test 2: Frequency of 30kHz**. The signals align pretty well.

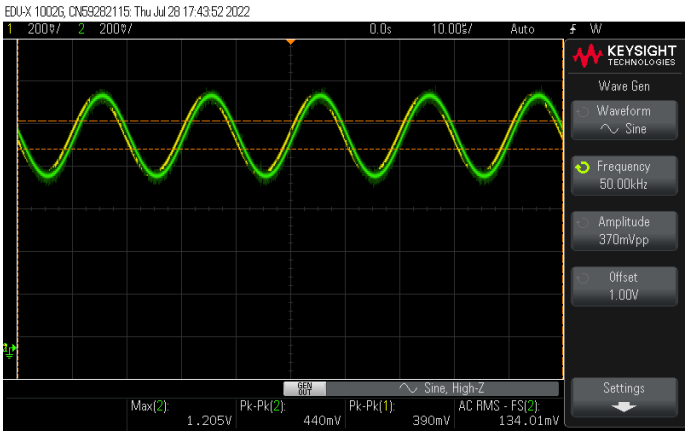

Figure 3.39: **Test 3: Frequency of 70kHz**. The signals still aligned for higher frequency.

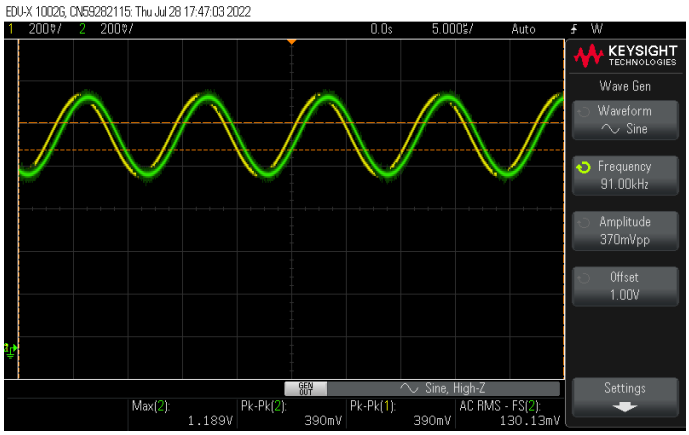

Figure 3.40: **Test 4: Frequency of 91kHz**. One can start noticing a small difference.

Power Supply

Design thought

The other feedback loop is to maintain the supply across the MOSFET's V_{DS}. To keep V_{DS} constant, one should control the voltage given by the power supply since part of it is taken by the sense resistor and the load, which may affect V_{DS} through factors like relaxation or thermal fluctuations. Unlike the previous feedback loop, this one has only one input, the measurement, and one output. The setpoint is designed to have a fixed voltage about 4.2V as we explained why before. As was seen in the general schematic, the measurement was taken over the MOSFET, not the whole circuit of the sense resistor , the load, and the MOSFET. The reason is the graphs depend on V_{DS}. The output is a signal that controls the power supply, which is BK precision 1693; 1V of the signal maps to 3V for the supply. Our aim is that the feedback loop would have at least 10Hz of bandwidth mainly because thermal fluctuations are slow.

Actual Design

The other part of the feedback is highlighted below. The setpoint voltage of 4.2V is set inside the circuit by a voltage divider that acts on the 15V that powers the current controller. You can see that in figure 3.41 where the purple arrow is pointing in the top right corner. The measurement with the in-circuit setpoint goes through the same stages as the inputs of the gate feedback loop. The output is then sent directly to remote controller

at the back of the power supply that controls its voltage; each 1V of the control signal $u(t)$ maps to 3V from the supply.

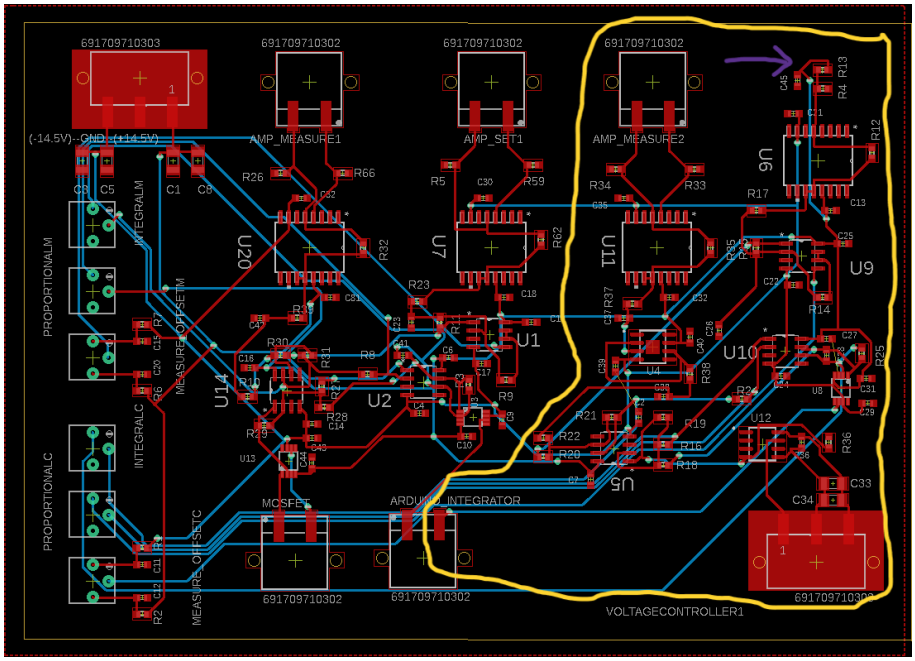

Figure 3.41: **Power Supply Feedback Part of Circuit**. The output is at the bottom. The arrow indicates the voltage divider used for the setpoint. The only input is at the top beside the arrow from the left.

Testing

The goal of our test to find what is the bandwidth of the feedback loop. The feedback has a 4.2V DC set point. Having a setpoint of a constant value forced us to look for a new variable to modulate with different. This variable was the gate voltage. To summarize the process, we modulate the gate with various frequencies and check the highest frequency, at which V_{DS} remain at 4.2V. Unfortunately, the feedback loop didn't work. A main problem is the overshooting from the integrator; it always turns off the power supply when the mapping exceeds 15V, which is the highest voltage the power supply can supply. Debugging is still in the process while we also think of an alternative way to control the power supply.

Chapter 4

Thermalization

4.1 Introduction

Statistical mechanics was a breakthrough that described how the macroscopic properties of the system emerged from the microscopic view of the system. Unlike statistical mechanics, these results were first derived from the very general, abstract laws of thermodynamics that didn't provide any reasons or interpretation of the microscopic point of view. Taking the ideal gas as an example, the laws of thermodynamics and the empirically derived equation of state $PV = kNT$ were used to derive different macroscopic properties such as entropy. In statistical mechanics, an ensemble of microstates satisfying certain macroscopic constraints is averaged over to give the macroscopic properties of the system. For an ideal gas, these constraints can be the volume and number of particles while the properties can be pressure and entropy.

Although statistical mechanics provided the microscopic point of view, it didn't provide any insight into how the dynamics of the system reach the equilibrium state; in other words, how is the ensemble of states connected to the unique state that is measured at a certain time? Unfortunately, the connection between statistical mechanics and the more fundamental classical mechanics isn't clear although some ideas were proposed. A popular idea that shows the connection is the ergodic hypothesis. The ergodic hypothesis is used to explain the microcanonical ensemble, which is a type of statistical ensemble used to describe an isolated system with constant energy. A basic postulate of statistical mechanics is the assumption that all the accessible systems in a phase space have equal probability. In the microcanonical ensemble, the accessible states are the states with equal energy.

The ergodic hypothesis states that the statistical ensemble average of the microstates in a phase space is equal to the long time average of the observable along the trajectory in the same phase space. This trajectory is created by the Hamiltonian dynamics for an initial state. The trajectory visits each region in the phase space that satisfies the macroscopic constraints, and it will spend time in a region proportional to its volume, from which the equal probability postulate can be seen. The ergodic hypothesis can be proven to a few systems; however, the time limit needed for the proof grows exponentially in the number of degrees of freedom, which makes it unpractical because different observables need less time to be measured.[1][9][10]

The ergodic hypothesis works only when there are no invariant quantities other than the total energy.[13] Additional invariant quantities will provide less accessible volume in the phase space for the trajectory. Some systems in one-dimension that have the same number of invariant quantities as degrees of freedom were found not to thermalize, or to be described by the microcanonical ensemble.[1] Evidently, invariant quantities have a great effect on the dynamics of a system. It is therefore worthwhile to classify classical systems into two classes known as integrable and non-integrable systems. Integrable systems have the same number of independent conserved quantities $(I_1, I_2, I_3, ...)$ as the number of degrees of freedom. The independence and conservation of these quantities to a certain system with the Hamiltonian H can be mathematically shown by the Poisson brackets:

$$\{I_j, H\} = 0, \quad \{I_j, I_k\} = 0, \quad \text{where} \quad \{f, g\} = \sum_{j=1,N} \frac{\partial f}{\partial q_j}\frac{\partial g}{\partial p_j} - \frac{\partial f}{\partial p_j}\frac{\partial g}{\partial q_j} \tag{4.1}$$

Integrable systems tend not to thermalize since they have simple dynamics from the Arnold-Liouville theorem, which shows a simple equation of motion that results from a canonical transformation to action-angle coordinates. Unlike integrable systems that visit only part of the phase space, non-integrable, or chaotic, systems have the number of degrees of freedom more than the number of conserved quantities. Having more degrees of freedom than conserved quantities leads the system to explore most of the phase space, so it seems that chaotic exploration of the phase space allows the ergodic hypothesis to be valid and therefore allows thermalization.[1] Chaos can be characterized by the Lyapunov exponent, which quantifies the sensitivity of the trajectory to an initial state. The exponent quantifies the difference between two trajectories at a later time of two initial states with a negligible difference. For example, the initial conditions of x_0 and $x_0 + \epsilon$ will have their difference quantified in the following way:

$$\Delta x(t) = \epsilon\, e^{\lambda t}$$

where λ is the Lyapunov exponent. A chaotic system will have a positive exponent, which will lead to exponential growth in the difference.[11] On the other hand, an integrable system has all its Lyapunov exponents equal to zero and consequently is not chaotic; there are two zero exponents for each constant of motion.[12]

Unlike classical mechanics, quantum mechanics is always linear. A small difference between two initial states will always be the same as time evolves. It can be seen from the overlap of two states under the time evolution U: $\langle\psi(t)|\phi(t)\rangle = \langle\psi(0)|\, U^\dagger U\, |\phi(0)\rangle = \langle\psi(0)|\phi(0)\rangle$. Therefore, the important question is how the observable thermalizes without any chaotic behavior like that of classical mechanics. An observable is said to thermalize if it can be described by the microcanonical ensemble, which is equal to the canonical ensemble in the thermodynamical limit where the fluctuations are negligible. Another question would be the effect of conserved quantities on quantum thermalization. After all, the integrability had a clear effect on the dynamics of a classical system in its phase space. One promising idea that explains the thermalization process is the Eigenstate Thermalization Hypothesis (ETH). It simply states that each eigenstate is a thermal state, which agrees with the microcanonical ensemble, and that thermalization happens as the system loses its coherence. We refer the readers to the following review about ETH to understand more about the topic and the studies made to validate it[1]. Another promising idea is the idea of dividing the system into a subsystem and a bath to understand the dynamics.[4] We plan to explore the second approach for various reasons that we will be discussed after covering most of the relevant studies and experiments.

The question of thermalization is important in the most important aspect of connecting statistical mechanics to quantum mechanics. After establishing the connection, it may shed some light on quantum thermodynamics and may give us a better understanding. We may even gain a better understanding of the thermodynamics in black holes, which is partially quantum. Using cold atoms, not only black holes but also cosmological phenomena can be studied since some experiments showed how similar physics was observed in cold atoms.[35,36] Thermalization can be tested very well in our labs for multiple reasons. The experiments will be very well isolated and very well controlled. We can quench our Hamiltonians in any way we want. Many experiments already were done and provided information that greatly enhanced our understanding of this topic. We plan to add to these experiments through novel techniques to gain a better understanding of the physics behind thermalization. To do so, we will discuss important points in this chapter. First, we will formulate the problem well so that we know what questions exactly we are addressing. We will then provide a review of the most important experiments that were made on this

topic. Some experiments were done using the Lieb-Liniger model as their system due to its integrability. We are interested in this model since our first experiments will be simulating it while resolving several technical problems that plagued previous experiments. We will also briefly shed some light on the Bose-Hubbard model to show an important technique that we are planning to use in the Lieb-Liniger model; this implementation is a longer-term goal. In the end, we will provide our theoretical approach to study thermalization and our novel planned experimental improvements that will be implemented in the future.

4.2 The Problem

The main goal is to understand when the expectation value for a quantum initial state is equal to that of a canonical or microcanonical ensemble. Statistical mechanics is usually used to describe equilibrium states; as a result, the better question would be the following. When the expectation value of the initial state reaches a stationary state, is this expectation value equal to that of the statistical ensemble? If a system reaches a stationary state, then a very long time average will make the result of this stationary state emerge since the system will be close to this state most of the time. Mathematically, the problem is described by the following equation:

$$\lim_{T\to\infty} \frac{1}{T} \int_0^T \langle\psi(t)|\hat{O}|\psi(t)\rangle \, dt \stackrel{??}{=} \mathrm{Tr}(\hat{\mathrm{O}}\hat{\rho}_{\mathrm{c}}]) \tag{4.2}$$

where $\hat{\rho}_c$ is the canonical ensemble, and we set $\hbar = 1$:

$$\hat{\rho}_{\mathrm{c}} \; = \frac{1}{Z} e^{-\beta \hat{H}} = \frac{1}{Z} \sum_{\alpha} e^{-\beta E_\alpha} |\alpha\rangle\langle\alpha| \tag{4.3}$$

where $H\,|\alpha\rangle = E_\alpha\,|\alpha\rangle$, $\beta = \frac{1}{k_{\mathrm{B}}T}$, and $Z = \mathrm{Tr}(\mathrm{e}^{-\beta\hat{\mathrm{H}}})$ is the partition function. The variable $k_{\mathrm{B}} = 1.380 \cdot 10^{-23}$ J/K is Boltzmann's constant.

4.2.1 The Setup

To equilibrate, one should first start from an out-of-equilibrium state. To achieve this state, the standard way is to prepare an initial eigenstate for your system of a certain Hamiltonian that is then quenched or changed suddenly such that the eigenstate isn't an eigenstate anymore. The system consequently will show some dynamics. Mathematically,

one starts with a ground state $|\psi_0\rangle$ for an initial Hamiltonian H_0, where $H_0 |\psi_i\rangle = E_i |\psi_i\rangle$. After a sudden quench from $H_0 \to H$ with a new set of eigenstates $\{|\phi_i\rangle\}$, the expectation value of an observable is calculated by expanding the initial state $|\psi_0\rangle$ in the set of the new eigenstates $\{|\phi_i\rangle\}$ and then applying the time evolution to it. The expansion takes the following form:

$$|\psi_0(t)\rangle = \sum_m c_m \mathrm{e}^{-i\epsilon_m t} |\phi_m\rangle$$

where $H |\phi_i\rangle = \epsilon_i |\phi_i\rangle$. The observable is as follows:

$$O(t) \equiv \langle\psi(t)|\hat{O}|\psi(t)\rangle = \sum_{m,n} c_m^* c_n e^{i(\epsilon_m - \epsilon_n)t} O_{mn} \tag{4.4}$$

$$= \sum_m |c_m|^2 O_{mm} + \sum_{n \neq m} c_m^* c_n e^{i(\epsilon_m - \epsilon_n)t} O_{mn} = \mathrm{Tr}(\hat{\mathrm{O}}\hat{\rho}_{\mathrm{D}}) + \Delta\mathrm{O(t)} \tag{4.5}$$

where $O_{mn} = \langle\phi_m| \hat{O} |\phi_n\rangle$, and $\hat{\rho}_D = \sum_i |c_i|^2 |\phi_i\rangle \langle\phi_i|$ is known as the diagonal ensemble. If a system equilibrates, one can then use the infinite time average of equation 4.2 to find the stationary state [1]:

$$\lim_{T\to\infty} \frac{1}{T} \int_0^T \langle\psi(t)|\hat{O}|\psi(t)\rangle \, dt = \sum_m |c_m|^2 O_{mm} = \mathrm{Tr}(\hat{\mathrm{O}}\hat{\rho}_{\mathrm{D}}) \tag{4.6}$$

Although the time average gives a constant quantity, it doesn't mean that the system may equilibrate; the system may keep oscillating around this constant value. One way to validate the equilibration process is to study the infinite time average of the fluctuations of the system $(\Delta O(t))^2$. In many studies, the fluctuations are observed to be small in the equilibration process.[7] The problem of whether an observable reaches a stationary state or not is known as the problem of equilibration, which is the first part of the problem of **quantum thermalization**.

Proving that the fluctuations are small in a long time average shows that most times the expectation value can be predicted by the diagonal ensemble; this kind of equilibration is known as equilibration on average. Another definition for equilibration is known as equilibration during an interval. In this second kind of equilibration, the expectation value is close to the diagonal ensemble during all the time of this interval. The interval is bounded from below by the relaxation or dephasing time and from above by the recurrence time, where the state returns to its initial state after a long time evolution.[14] If one has to choose between the two definitions, we prefer the second one because measurements can be

done to better study a finite interval of time than an infinite time average. A measurement that takes a long time can average out any fluctuations, but a very short measurement can probe the fluctuations well and validate the definition of equilibration during intervals. The following equation resembles equilibration while taking measurements into account:

$$\frac{1}{T_m}\int_t^{t+T_m} \langle\psi(t')|\hat{O}|\psi(t')\rangle\, dt' = \sum_m |c_m|^2\, O_{mm} = Tr(\hat{O}\rho_D) \quad T_d < t < T_r$$

where T_d is the dephasing time after which equilibration takes place. The dephasing time shows the time that a system takes to lose its coherence. The variable T_m is the measurement time of the observable, and T_r is the recurrence time. More details about these times will be discussed later.

The second part of the problem is the thermalization itself. In other words, does the expectation value of the stationary state agree with that of the statistical ensembles? In other words, is the following equation true? [4]

$$Tr(\hat{O}\rho_D) \stackrel{??}{=} Tr(\hat{O}\rho_c)$$

A stronger statement would be the equality of the distribution for the observable for both results, which can be calculated for the projectors of $\hat{O}$. In a time-of-flight measurement, one can measure the momentum distribution and therefore the projectors of momentum. In the following sections, we will study each part of the problem alone.[7]

4.2.2 Thermalization

We will start with the second part since it is a prerequisite to understand the different phases in an equilibration process. Integrability has a large role in this part of the problem. The definition of integrability is a subject of debate; however, a standard definition that is sufficient for the following discussion is the existence of conserved observables I_k that commute with the Hamiltonian $[H, I_k] = 0$ and among themselves $[I_k, I_m] = 0$. The commutation relations are the quantum analogue of the Poisson brackets in equation 4.1. It is believed that the conserved observables are usually local and extensive.[1][8][37]

Let's restate our problem. If an expectation value of an observable equilibrates, does the reached stationary state provide the same prediction as a canonical or microcanonical ensemble? Furthermore, if a system was integrable, what would be the role played by the

conserved quantities? Starting with the latter question, it makes sense that a system that has conserved quantities should keep these quantities conserved if the quenched Hamiltonian still commutes with these quantities. In other words, if the system equilibrates, our measurement of these observables or our "information" of the system shouldn't change; therefore, the equilibrated state should still have a memory of these initial conserved quantities and is completely unbiased in any other way. This state is usually found by Jaynes' Principle of Maximum Entropy. In this context, being unbiased means that the uncertainty, which is quantified by Shannon entropy, should be maximized while meeting the constraints of conserved quantities. In classical statistical mechanics, the entropy, which is just proportional to Shannon entropy by Boltzmann's constant, should be maximized yielding the canonical ensemble if energy is the only conserved quantity. In the quantum case, the Von Neumann entropy, $S = -\operatorname{Tr}(\rho \ln \rho)$, is the quantity maximized. Having extra conserved quantities I_k other than the energy introduces extra Lagrange multipliers in the exponent. Mathematically, assuming that a set of observables $\{I_k\}$ commute with the Hamiltonian with a known expectation value $\langle \hat{I}_k \rangle$, then the following density operator known as the Generalized Gibbs Ensemble (GGE) maximizes the Von Neumann entropy:

$$\hat{\rho}_{\mathrm{GGE}} = \frac{1}{Z} \exp\left(- \sum_m \lambda_m \hat{I}_m \right) \tag{4.7}$$

where $Z = \operatorname{Tr}\left(\exp\left(-\sum_{\mathrm{m}} \lambda_{\mathrm{m}} \hat{\mathrm{I}}_{\mathrm{m}}\right)\right)$. The Lagrange multipliers associated with each conserved quantity are chosen such that [2-3,8]:

$$\operatorname{Tr}\left[\hat{I}_m \hat{\rho}_{\mathrm{GGE}}\right] = \left\langle \hat{I}_m \right\rangle (t = 0)$$

It may seem that the idea of maximizing entropy is trivial and known already, so what is too special about Jaynes' Principle? The idea is that previously entropy was an empirical result of studying things like the Carnot engine or thermodynamical systems generally. The positive change of entropy always haunted scientists who tried to find an explanation using the more fundamental classical mechanics. But, here is the thing: what if maximizing the uncertainty or entropy is already a fundamental thing from the start? By reversing the way physics problems are treated, statistical inferences may provide new insight, quoting Jaynes in her paper: "In freeing the theory from its apparent dependence on physical hypotheses of the above type, we make it possible to see statistical mechanics in a much more general light". The generalized gibbs ensemble is exactly the reward of this treatment. After all, recall that the way gibbs ensemble, or canonical ensemble, was derived is different from the way of maximizing entropy.

Furthermore, Jaynes' principle gives us a way to derive ensembles for *pure* quantum systems. Generalized gibbs ensemble was shown in various numerical and experimental studies after a pure quantum system relaxes.[1, 30, 33, 39] When the energy is the only conserved quantity, it was observed that the gibbs ensemble, also known as the canonical ensemble, was the result.[34, 47-49, 51] So to answer our previous questions, an equilibrated state satisfies a canonical ensemble if the energy is the only conserved quantity and agrees with the generalized gibbs state if other conserved quantities exist. The generalized gibbs ensemble answers the second question about the effect of commuting observables. But there is still a remaining question: how exactly do these states emerge? To elaborate more, what is special about the eigenstates or their probability distribution after the quench to agree with these ensembles? One promising answer for the non-integrable systems is the ETH; however, it is a hypothesis that would need to be proved. The subsystem-bath approach may also carry a potential answer.

4.2.3 Equilibration

We discuss the first part of the problem. Before even considering the stationary states, one should check if the system equilibrates. Does $\Delta O(t)$ vanish in equation 4.4? One way to approach the problem is to think that the quantity $\Delta O(t)$ is made up of different vectors $v_{\alpha,\beta}$ in the complex plane, and they rotate with different angular frequencies G_α.

$$\Delta O(t) = \sum_{\beta}(\sum_{\alpha} v_{\alpha,\beta})e^{-iG_\beta t} = \sum_{\beta} Z_\beta e^{-iG_\beta t} \tag{4.8}$$

where $v_{\alpha,\beta} = c_m^* O_{m,n}\, c_n$ such that $G_\beta = E_n - E_m$ is an energy gap, and Z_β is the sum of all v_α that shares the same energy gap. The energy gap G_β determines how fast Z_β rotates in the complex plane. From this point of view, a system equilibrates when all these vectors distribute uniformly in the complex plane such that their sum is negligible. This process of redistribution over the complex plane depends on two major points: the distribution of energy gaps and the number of vectors. A small number of vectors will make the whole expectation value oscillate instead of equilibrating; think about a superposition of only two states and how it causes the expectation value to oscillate. Furthermore, more vectors will provide a longer time for them to realign. This process eventually happens and is known as recurrence; however, recurrence time increases exponentially as the number of vectors increases. Having many vectors is equivalent to having a larger system and a larger quench.[14] The distribution of energy gaps is also important since it is the rotation speed of these vectors on the complex plane. In the extreme case where the energy gaps are very close to each other, it will take a very long time to notice any appreciated angular

distance between the vectors.[7] Figure 4.1 below shows the equilibration dynamics for an XXZ model.[15]

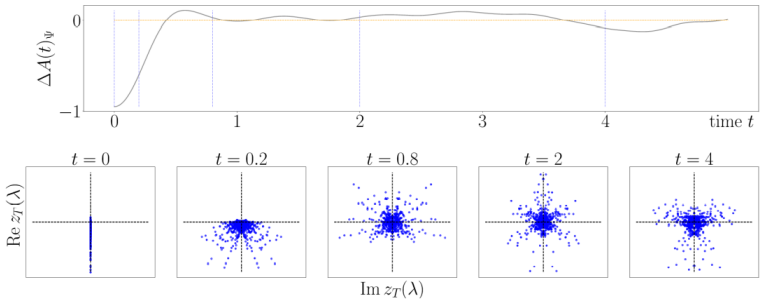

Figure 4.1: **Equilibration dynamics for an XXZ model**. The deviation of the expectation value of $\hat{A}$ from that of the diagonal ensemble is seen in the figure above while the vector representation is below. It is seen how the vectors redistribute well around the origin. The figure is taken from ref [15].

In the absolute sense of approaching an infinite time average or in the definition of equilibration on average, large quantum systems do equilibrate. A study showed that an infinite time average of a finite non-degenerate Hamiltonian shows that the fluctuations are bounded by the effective dimension:

$$\sigma_A^2 \equiv \lim_{T\to\infty} \frac{1}{T}\int_0^T (\mathrm{Tr}(\hat{\mathrm{A}}\hat{\rho}(\mathrm{t})) - \mathrm{Tr}(\hat{\mathrm{A}}\hat{\rho}_{\mathrm{D}}))^2 \mathrm{dt} \leqslant \frac{\|\mathrm{A}\|^2}{\mathrm{d_{eff}}}$$

where $\|A\| = \sup\left\{\sqrt{\langle v\,|A^\dagger A|\,v\rangle} : |v\rangle \in \mathcal{H} \text{ with } \langle v \mid v\rangle = 1\right\}$, $d_{\text{eff}} = \frac{1}{\sum_k \mathrm{tr}(P_k\rho(0))^2}$ is the effective dimension, and $\hat{P}_k$ is the Hamiltonian's projector. The effective dimension is a measure of how spread the initial state is in the new eigenbasis after the quench. The more spread the system is the tighter the bound is. Note that for a pure state $d_{\text{eff}} = \mathrm{tr}\,(\rho_D^2)^{-1}$. One might argue that equal expectation values don't mean that the density states can't be distinguished; therefore, the study also derived a bound for distinguishability, whose bound was proportional to $(d_{\text{eff}})^{-1/2}$. Bounds were also derived for subsystems.[5] A later study relaxed the non-degenerate assumption and, even more, derived a finite average bound for distinguishability and fluctuations of expectation values for both the full system and a subsystem.[6] From these studies, one can conclude that the equilibration depends on a critical quantity, which is the effective dimension. The effective dimension reflects the first point of the distribution of vectors on the complex plane; a small number of d_{eff} means that

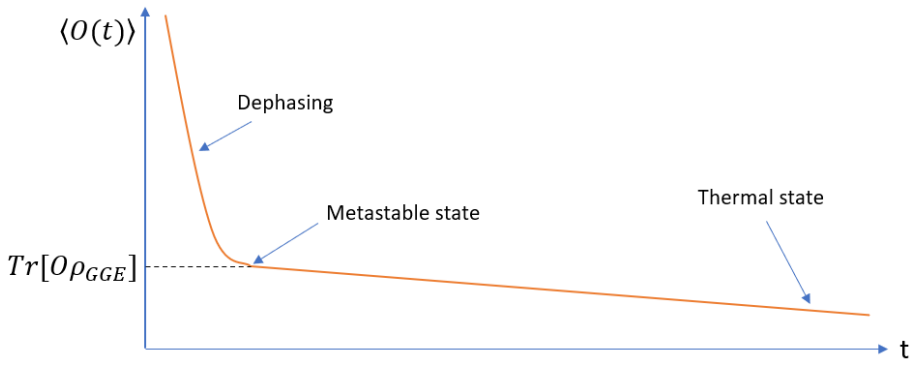

Figure 4.2: **Equilibration Process**. The orange shaded region shows the dephasing phase. Right after the dephasing at the tick in the time axis, the system is in the prethermal state that can be described using the generalized gibbs ensemble. The system later decays slowly to its thermal state.[8,18]

a few vectors are revolving which will result in oscillations of the expectation values. It is discussed in several studies that d_{eff} is usually large for large systems.[16,17] In summary, the goal of these studies just show that equilibration happens.[7]

However, the problem with these equilibration studies is that it doesn't provide any practical time scales for the equilibration process. In general, there have been three time scales if the system was near-integrable. By near-integrable, it is meant that the conserved quantities are very weakly broken $[I_k, H] = \epsilon$. The first one is dephasing, which is usually fast. In dephasing, the system loses any coherence between its states. The second step is a metastable state known as prethermalization, where the system has a memory of its very weakly broken conserved quantities. The generalized gibbs ensemble describes this state. After that, the system decays slowly to reach a thermal state during the third phase.[8] The process is shown in figure 4.2. What is interesting is that the canonical ensemble appears at a much longer time when the integrability is very weakly broken. This behavior leads to the question if such perturbation will lead to a quantum version of KAM theory. Another question is whether the thermal state will emerge sooner if the conserved quantities were better broken, which was answered by two experiments that will be discussed later.[34,47]

4.3 Lieb-Liniger and Bose-Hubbard Models

Lieb-Liniger and Bose-Hubbard models are systems that can be created efficiently in the lab, and they provide key insights into the problem of thermalization. For these reasons, we will now discuss some key studies and experiments that were done about these two systems. After the discussion of these systems, we will provide the arguments of why we are interested to study the problem in the subsystem-bath approach.

4.3.1 Lieb-Liniger Model

The Lieb-Liniger is a 1D Bose gas with contact interactions or dirac-delta potential function. The theoretical problem was tackled and solved in 1963 before any experimental implementation.[19] This model is an integrable system that doesn't thermalize. The non-thermalization can be intuitively seen from the contact potential, which only allows particles to exchange momenta. In this section, the theoretical background of the model will be discussed. Then, we will discuss the main experiments done using this model to understand thermalization.

Theoretical Background

The Hamiltonian of the Lieb-Liniger model is written in terms of the bosonic field operators that satisfy the following commutation relations [21]:

$$\left[\Psi(x), \Psi^\dagger(y)\right] = \delta(x-y)$$
$$[\Psi(x), \Psi(y)] = \left[\Psi^\dagger(x), \Psi^\dagger(y)\right] = 0$$

The second quantization of the Hamiltonian is the following:

$$H = \int dx \left[\frac{\hbar^2}{2m}\partial_x\Psi^\dagger(x)\partial_x\Psi(x) + \frac{g_{1D}}{2}\Psi^\dagger(x)\Psi^\dagger(x)\Psi(x)\Psi(x)\right] \tag{4.9}$$

where $g_{1\mathrm{D}} = \alpha \cdot g$ is the 1D interaction strength. The constant $g = \frac{4\pi\hbar^2 a}{m}$ is the coupling strength that is proportional to the 3D scattering length a, and α is some constant that depends on the physical setup. The scattering length can be positive or negative depending on the applied Feshbach resonance discussed in chapter 1.[20] In our case, we assume a

positive scattering length $g > 0$. Another way to specify your systems is through the dimensionless quantity known as the Lieb parameter:

$$\gamma = \frac{m g_{1\mathrm{D}}}{\hbar^2 n_{1\mathrm{D}}} \tag{4.10}$$

where $n_{1\mathrm{D}}$ is the linear density.[25] The solution shown in 1963 used what is known as the Bethe ansatz. To understand what is the Bethe ansatz and the physics behind it, one should first understand the two-particle case.

Two-particle Case

The Hamiltonian of the two-particle case is the following:

$$H = -\frac{\partial^2}{\partial x_1^2} - \frac{\partial^2}{\partial x_2^2} + 2c\,\delta\left(x_2 - x_1\right) \tag{4.11}$$

where $c = g_{1\mathrm{D}} m/\hbar^2$. If there was no interaction at all $g_{1\mathrm{D}} = 0$, the solution to the Hamiltonian would be trivial; it will just be a symmetric wavefunction made of plane waves. Adding a contact potential makes things a little tricky. If $x_1 \neq x_2$, then the particles won't be in contact and would have normal plane wave solutions. However if $x_1 = x_2$, then the particles would be in contact, and we would expect that there will be some kind of momenta exchange between them that depends on the coupling $g_{1\mathrm{D}}$. The way to deal with the dirac delta is similar to the standard way to solve the dirac delta potential in a first quantum mechanics course; the dirac delta results in a boundary condition that determines the change in the first derivative of the wavefunction.[22] To get the familiar boundary conditions, one transforms the coordinates to the center-of-mass frame: $R = \frac{x_1+x_2}{2}$ and $r = \frac{x_2-x_1}{2}$. The Hamiltonian would then be:

$$H = -\frac{1}{2}\frac{\partial^2}{\partial R^2} - \frac{1}{2}\frac{\partial^2}{\partial r^2} + c\,\delta(r)$$

Integrating around r:

$$\lim_{\epsilon\to 0}\int_{-\epsilon}^{\epsilon} dr\ \left[-\frac{1}{2}\frac{\partial^2}{\partial R^2}\psi(r,R) - \frac{1}{2}\frac{\partial^2}{\partial r^2}\psi(r,R) + c\delta(r)\psi(r,R)\right] = \lim_{\epsilon\to 0}\int_{-\epsilon}^{\epsilon} dr\, E\psi(r,R)$$

Resulting in the following boundary condition equation:

$$\begin{aligned} -\frac{1}{2}\frac{\partial}{\partial r}\psi(r)\Big|_{r=0^-}^{r=0^+} + c\,\psi(0) &= 0 \\ \left(\frac{\partial}{\partial x_2} - \frac{\partial}{\partial x_1} - c\right)\psi\Big|_{x_2=x_1+0} &= 0 \end{aligned} \tag{4.12}$$

Now, the goal is to find a solution that satisfies both the boundary condition in equation 4.12 and the Hamiltonian without the dirac delta in equation 4.11 since satisfying the boundary condition is satisfying the dirac delta. The solution to the Hamiltonian is given by the Bethe ansatz:

$$\psi(x_1, x_2) = Ae^{-i(\lambda_1 \cdot x_1 + \lambda_2 \cdot x_2)} + Be^{-i(\lambda_1 \cdot x_2 + \lambda_2 \cdot x_1)} \tag{4.13}$$

The solution is merely a superposition of two plane waves, where the exchange of the variables x_1 and x_2 implies the elastic exchange of λ_i's between the two particles; furthermore, the exchange of λ_i's is proportional to the coupling strength c according to equation 4.12. Note that λ_i is known as the rapidity in literature and not strictly a momentum of one particle since $\psi(x_1, x_2)$ is not an eigenstate for $p_i = -i\frac{\partial}{\partial x_i}$; however, these rapidities can be measured for freely expanding bosons after turning off the trap. This solution clearly solves the Hamiltonian, and now we should satisfy the boundary condition. Plugging this solution into equation 4.12 results in:

$$\frac{A}{B} = \frac{i(\lambda_2 - \lambda_1) + c}{i(\lambda_2 - \lambda_1) - c} \tag{4.14}$$

Equations 4.13 and 4.14 are our solution to the problem with λ_i's as our free parameters that usually be specified depending on the boundary conditions of the system, i.e. periodic or a particle in a box.[23,25]

The General Solution

The solution for N particles can be generalized; the details of the solution can be found in the following reference [24]. Without going through the derivation of the solution in equation , a few properties of the solution should be pointed out.

$$\begin{aligned}\psi(x_1, x_2, ...) = &\left\{ N! \prod_{j>k} \left[(\lambda_j - \lambda_k)^2 + c^2 \right] \right\}^{-1/2} \\ &\times \sum_{\mathcal{P}} (-1)^{[\mathcal{P}]} \exp\left\{ i \sum_{n=1}^{N} x_n \lambda_{\mathcal{P}_n} \right\} \prod_{j>k} [\lambda_{\mathcal{P}_j} - \lambda_{\mathcal{P}_k} - ic \cdot \mathrm{sgn}(x_j - x_k)]\end{aligned} \tag{4.15}$$

First, $[\mathcal{P}]$ denotes the parity permutation of the set of rapidities allowed $\{\lambda_i\}$; this term is necessary since we are taking all the combinations of how the rapidities are exchanged between the particles. Second, the wavefunction is symmetric in the position variables

$\psi(x_1, x_2, ...) = \psi(x_2, x_1, ...)$; this symmetry is expected since we are dealing with bosons. The sign function in the solution below allows such symmetry. Finally, the wavefunction is antisymmetric in the rapidities $\psi(\lambda_1, \lambda_2, ...) = -\psi(\lambda_2, \lambda_1, ...)$; this fermionic behavior towards the rapidities is a byproduct of the boundary condition imposed by the dirac delta.[24] In my opinion, physically this antisymmetry makes sense since it prevents particles to have the same probability distribution and thus to be in contact at all times. To elaborate more, if the particles were in a box and were all in the ground state, then the overlap between the particles would be maximized, which should be prevented by the dirac delta contact potential.

Conserved Quantities

The Lieb-Liniger is an integrable system. Intuitively it can be seen from the wavefunction where it shows clearly the exchange of rapidities by assigning the same λ's to different variables x_i. Ideally, the system will never thermalize in a sense of reaching the Maxwell-Boltzmann distribution for the momentum. After understanding the physics of the system, it is natural to ask the more formal question of what the conserved quantities are. One can simply show that the number of particles $N = \int dx\, \Psi^\dagger(x)\Psi(x)$ and the total momentum $P = i\int dx\, \left[\partial_x \Psi^\dagger(x)\right] \Psi(x)$ are conserved quantities through their commutation with the Hamiltonian (12):

$$[H, N] = [H, P] = [N, P] = 0$$

Since the set of rapidities doesn't change at all, then it makes sense that any function $f(\lambda)$ that takes these rapidities as eigenstates will be a conserved quantity: $\hat{f}\,|\psi(\lambda_1, \lambda_2, ...)\rangle = (\sum_i f(\lambda_i))\,|\psi(\lambda_1, \lambda_2, ...)\rangle$. Simple examples of f are P and H:

$$\hat{P}\,|\psi(\lambda_1, \lambda_2, ...)\rangle = (\sum_i \lambda_i)\,|\psi(\lambda_1, \lambda_2, ...)\rangle$$

$$\hat{H}\,|\psi(\lambda_1, \lambda_2, ...)\rangle = (\sum_i \lambda_i^2)\,|\psi(\lambda_1, \lambda_2, ...)\rangle$$

$$\hat{P}_n\,|\psi(\lambda_1, \lambda_2, ...)\rangle = (\sum_i \lambda_i^n)\,|\psi(\lambda_1, \lambda_2, ...)\rangle$$

where $\hat{P}_n$ is just an operator with the shown eigenvalue. As can be seen, the Lieb-Liniger model has an infinite number of conserved quantities.[25] An infinite conserved quantities lead to the question if they will all appear in the GGE. I would argue that only the $\hat{P}_n$'s would appear since any operator $\hat{f}$ can be written in terms of this so-called basis. To see

how the expansion happens, we start with the following equation:

$$\begin{aligned}\hat{f}\left|\psi(\lambda_1,\lambda_2,...)\right\rangle &= (\sum_i f(\lambda_i))\left|\psi(\lambda_1,\lambda_2,...)\right\rangle \\ &= \sum_{n=0}^{\infty}\sum_{i=0}^{N}\frac{f^{(n)}(0)}{n!}(\lambda_i)^n \\ &= \sum_{n=0}^{\infty}\frac{f^{(n)}(0)}{n!}\sum_{i=0}^{N}[(\lambda_i)^n] \\ &= \sum_{n=0}^{\infty}\frac{f^{(n)}(0)}{n!}\hat{P}_n\left|\psi(\lambda_1,\lambda_2,...)\right\rangle\end{aligned}$$

One can see how each conserved quantity can be written in terms of $\hat{P}_n$'s.

Approximation: Luttinger Liquid Model

At a certain regime, the 1D Bose gas can be treated as a quantum Luttinger liquid. The Luttinger liquid model provides a general description of the low-energy properties of a wide range of 1D systems. The Luttinger liquid shares some main properties including defining a sound velocity and having a gapless, linear-dispersing excitation.[26] The low-energy physics of these 1D systems can be described using a density field operator $\hat{n}(x) = \Psi^\dagger\Psi$; it is not surprising to use a density operator to describe a quantum fluid since intuitively classical fluids are described by the density. To validate the use of the density field operator, one should check that the density fluctuations can indeed be small in certain regimes. These fluctuations can be studied using a quantity known as the density-density correlation function $S(x_2,t_2,x_1,t_1) = \langle\hat{n}(x_2,t_2)\hat{n}(x_1,t_1)\rangle$. In a homogeneous systems, only the differences in distance $x = x_2 - x_1$ and in time $t = t_2 - t_1$ matter, so we can write $S(x,t) = \langle\hat{n}(x_2,t_2)\hat{n}(x_1,t_1)\rangle = \langle\hat{n}(x,t)\hat{n}(0,0)\rangle$. The density-density correlation function shows the fluctuations since it appears in the variance in density at a specific point r:

$$\mathrm{Var}(\hat{n}(\mathbf{r})) \equiv \left\langle\hat{n}(\mathbf{r})^2\right\rangle - \langle\hat{n}(\mathbf{r})\rangle^2 = S(0,0) - \langle\hat{n}(\mathbf{r})\rangle^2$$

By using the commutation relation, the density-density correlation can be written in terms of the popular 2nd-order correlation function $g_2(x)$:

$$S(x) = \left\langle\Psi^\dagger(0)\Psi^\dagger(x)\Psi(x)\Psi(0)\right\rangle + \delta(x)\left\langle\Psi^\dagger(x)\Psi(0)\right\rangle = n^2 g_2(x) + \delta(x)\left\langle\Psi^\dagger(x)\Psi(0)\right\rangle$$

where,

$$g_2(x) = \frac{\left\langle \hat{\Psi}^\dagger(0)\,\hat{\Psi}^\dagger(x)\,\hat{\Psi}(x)\,\hat{\Psi}(0)\right\rangle}{\left[\langle \hat{n}(x)\rangle\,\langle \hat{n}(0)\rangle\right]^{1/2}}$$

Usually, the correlations are studied using the quantity $g_2(x)$ to get rid of the divergent term $\delta(0)\cdot n$, or another way would be to discretize the real space [31]. In figure 4.3, the quantity $g_2(x)$ is shown for different strengths of g or, more precisely, $\gamma = c/n_{1D}$. The weak interaction has no oscillations and changes slowly showing low density fluctuations. Such low interactions at low energy levels allow us to transform our field operators into a density $\hat{n}(z)$ and a phase $\hat{\phi}(z)$ field operators: $\hat{\Psi}(z) = e^{i\hat{\phi}(z)}\sqrt{n_{1\mathrm{D}} + \hat{n}(z)}$. This transformation allows us to simplify our system into the Luttinger liquid model, which can be diagonalized easily using a Bogoliubov transformation, and to study correlation functions efficiently, which was done in an essential experiment that proved the generalized gibbs ensemble.[39]

Inserting the preceding transformation into equation 4.9:

$$\begin{aligned}\hat{H} &= \frac{\hbar c}{2}\int dz\left[\frac{K}{\pi}\left(\frac{\partial\hat{\phi}(z)}{\partial z}\right)^2 + \frac{\pi}{K}\hat{n}(z)^2\right] \\ &= \sum_k \hbar\omega_k \hat{a}_k^\dagger \hat{a}_k\end{aligned} \tag{4.16}$$

where $\omega_k = ck$ is a linear dispersion relation, $c = \sqrt{gn_{1\mathrm{D}}/2m}$ is the speed of sound, and $K = \sqrt{n_{1\mathrm{D}}(\hbar\pi)^2/4g_{1\mathrm{D}}m}$ is the Luttinger parameter. This is Hamiltonian of the Luttinger liquid model. The diagonalization is achieved using the following transformation of the Fourier components of the phase and density field operators:

$$\begin{aligned}\hat{n}_k &\sim \left(\hat{a}_k(t) + \hat{a}_{-k}^\dagger(t)\right) \\ \hat{\phi}_k &\sim \left(\hat{a}_k(t) - \hat{a}_{-k}^\dagger(t)\right)\end{aligned}$$

Unlike the conserved quantities of the Lieb-Liniger, the conserved quantities here are $N_k = \hat{a}_k^\dagger\hat{a}_k$ for each mode k. The advantage of the Luttinger-liquid mode is the easy way to calculate the correlation functions. Here is a 2nd-order correlation function for two different systems labeled l and r:

$$g_2(z_1, z_2) = \frac{\left\langle \Psi_l(z_1)\,\Psi_r^\dagger(z_1)\,\Psi_l^\dagger(z_2)\,\Psi_r(z_2)\right\rangle}{\left\langle |\Psi_l(z_1)|^2\right\rangle\left\langle |\Psi_r(z_2)|^2\right\rangle} = \langle \exp\left[i\Delta\phi(z_1) - i\Delta\phi(z_2)\right]\rangle$$

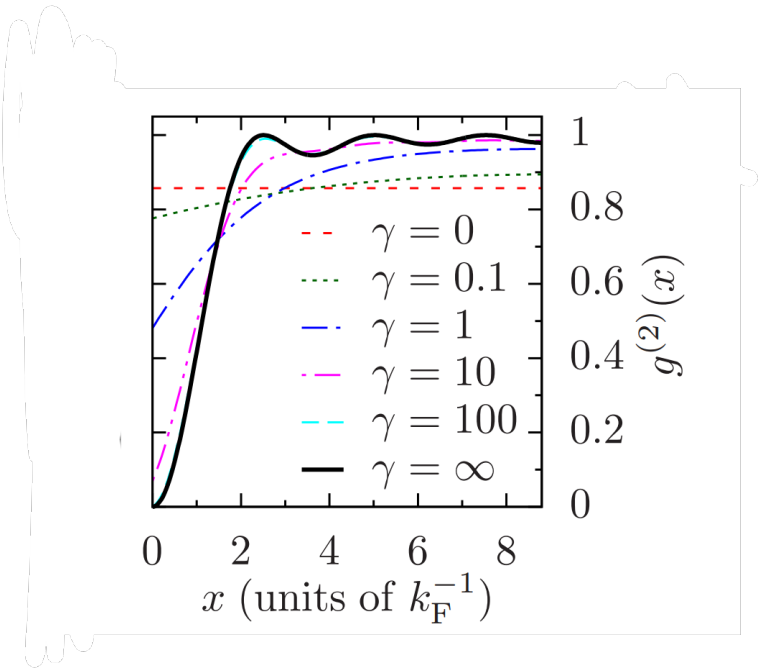

Figure 4.3: **Correlations between $g_2(x)$ and γ.** The 2nd-order correlation function is graphed for different strengths with respect to x in the units of $k_{\mathrm{F}} = \frac{2\pi}{L}\frac{N-1}{2}$, where L is the size of the system and N is the number of particles. It can be seen that there are small fluctuations for the weaker interactions while the infinite one has many ripples with an anticorrelation during the interval near the origin. The weak fluctuations justify the approximation of using density field operators to describe the system.The figure is taken from ref [23].

where $\Delta\phi(z_1) = \phi_l(z_1) - \phi_r(z_1)$. Finally, weakly interacting Bose gas is a vague description unless two quantities are compared to each other. The approximation works well when $\gamma << 1$. This can be seen by comparing different lengths: $\sqrt{\gamma} = d/\xi$, where $d = 1/n$ is the interparticle distance and $\xi = \hbar/\sqrt{mng_{1\mathrm{D}}}$ is the correlation length. It is the regime where the interparticle distance is much lower than the correlation length. This regime is known as the quasicondensate regime, a known term in the literature. [27]

Experimental and Numerical Studies

The experiments that have been made can be divided into three categories. One is showing the integrability of the Lieb-Liniger model. The second category of experiments studied

if integrability can be described using GGE. Finally, the last set of studies showed how integrability can be broken.

Integrability

Quantum Newton's Cradle

In a breakthrough experiment done to show the integrability of the Lieb-Liniger model, a quantum Newton's cradle was created by Kinoshita. This experiment showed the non-thermalization of two colliding Bose gases that had equal, opposite momenta. We start by briefly talking about the setup of the experiment. The setup is the part of the experiment that specifies the Hamiltonian and determines its parameters. In this case, the Lieb parameter γ is determined by the density and the confinement of bosons. They are confined strongly in the transverse direction and weakly in the axial direction. Regarding the transverse direction, the 1D Bose gas was created by loading a Bose-Einstein condensate of rubidium atoms into a 2D optical lattice, which created the transverse confinement of the Bose gas. Being loaded into a lattice means that we are creating an array of 1D Bose gases, where only ensemble averages, or expectation values, are accessible in a measurement. The confinement provided by the lattice can be described by a harmonic oscillator with an angular frequency $\omega_\perp$. The first excited energy level $\hbar\omega_\perp$ would be greater than any energy scale in our system to make sure that the bosons are in the transverse ground state and consequently one dimensional. The transverse confinement also determines the constant α of $g_{1\mathrm{D}}$ in equation (4.10), setting $\alpha = \frac{m\omega_\perp}{2\pi\hbar}$. This detail shows that the strength of the interaction $g_{1\mathrm{D}}$ is controlled by the confinement of the transverse direction. On the other side, the axial direction is trapped weakly using a crossed-dipole trap, where its size can easily be changed optically (just by moving the lens) [28]. An anharmonic oscillator will be created due to the nature of the gaussian beam, and the axial oscillation period of this oscillator is controlled by the trap's size and power. The size of the trap determines the linear density, which is another parameter to tune in the Lieb parameter. In the experiment, the Lieb parameter is set in the Tonks–Girardeau regime $\gamma >> 1$ since the three-body decay is minimized in this regime.[38] In summary of the setup, the interaction strength $g_{1\mathrm{D}}$ is determined from the transverse trap while the density is controlled by the axial trap.

Studying the thermalization of a system requires putting it out of equilibrium, which was done by applying two pulses of standing waves on the loaded 1D Bose gas. These two pulses divide the atoms into two Bose gases of equal, opposite momenta $\pm 2\hbar k$, where k is

the wavevector of the standing wave.[29] The states of these bose gases can be described by a coherent state. Interestingly, the two coherent states of the Bose gases will keep oscillating and colliding with each other along the axial anharmonic trap. As stated in the paper, these collisions will have a total energy of $8(\hbar k)^2/2m = 0.45\hbar\omega_\perp$, which will not cause any excitations in the transverse direction. Since the trap is anharmonic, the coherent states will dephase with time causing the atoms to spread along the tube and consequently to have less linear density, which will increase the Lieb parameter.

After oscillating for a time t, the 1D Bose gas is released from the crossed dipole trap and allowed to expand in 1D for 27 ms before taking a picture from the transverse direction; the long time expansion is necessary for the time-of-flight measurement of the momentum. The momentum distribution $f(p)$ of these measurements never had a gaussian distribution that is expected from a canonical ensemble; therefore, one can conclude that the system never thermalizes as fast as a 3D Bose gas, which showed thermalization in the observation time limit of the experiment.

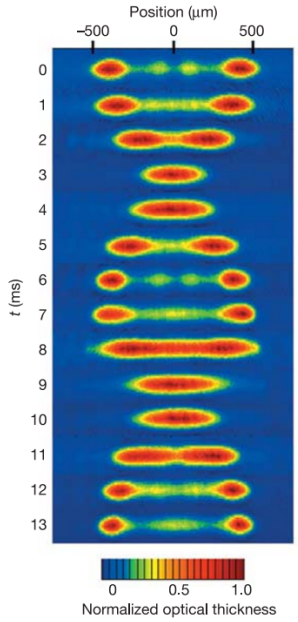

(a) Absorption image after the expansion due to turning off the dipole trap.

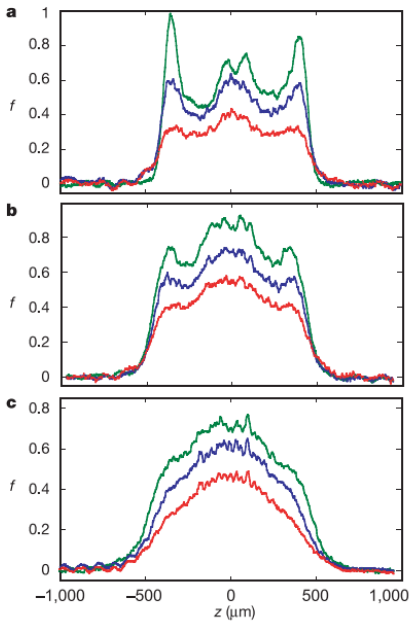

(b) Momentum distribution after processing the absorption images.

Figure 4.4: **Quantum Newton's Cradle**. (a) The absorption image is taken for the first full oscillation of the Bose gases. It is clear that the collisions still maintained two distinct Bose gases; thus, the system didn't thermalize. Note also the narrower peaks of the last picture at the bottom compared to the first one at the top; this change in spatial density is due to the dephasing of atoms caused by the anharmonicity of the trap. (b) This is the expanded momentum distribution for three different Lieb parameters $\gamma = c/n_{1D}$: $\gamma = 4$ for figure a, $\gamma = 1$ for figure b, and $\gamma = 0.62$ for figure c. The green curve is the average $f(p)$ for one oscillation while the blue and red curves are the distribution at given instants of time when the atoms have dephased. Notice how the distributions always have the same shape, which reflects the contact interaction. Since the curves never reached a gaussian one, the system didn't thermalize. The figures are taken from ref [51].

Although this experiment showed the integrability of the Lieb-Liniger model, it has a few limitations. One limitation is the dephasing due to the anharmonicity, which shows that the change of the momenta distribution is due to the technical details as well as to the interactions of the system. Mixing both wouldn't help us to see the role of the

contact interactions purely on our system. Another limitation was the loss of atoms that didn't allow long time observations of the system. Such limitation doesn't show if the near-integrable system thermalizes at the end; it just shows that it doesn't thermalize on the same time scale as an equilibrium Bose gas. In figure 4.4b, the red curves in (b) and (c) correspond to an observation at time t=40τ, where τ is the period of the system.[51]

Prethermalization in 1D Bose Gas

Not reaching a gaussian distribution is not the only property of integrable systems. Another property is reaching a prethermal state that doesn't describe thermal equilibrium. A hint of the prethermal state can be seen in the quantum Newton's cradle experiment when the momentum distribution didn't have much change in its shape between the red and blue curves in figure 4.4b. As much as this is a good hint, another experiment was needed to study the equilibration process discussed in the theoretical background section to observe a prethermal state. In an interference experiment that will now be discussed, the equilibration process was shown indicating a prethermal state for the 1D Bose gas; furthermore, it partially validates the generalized gibbs ensemble.

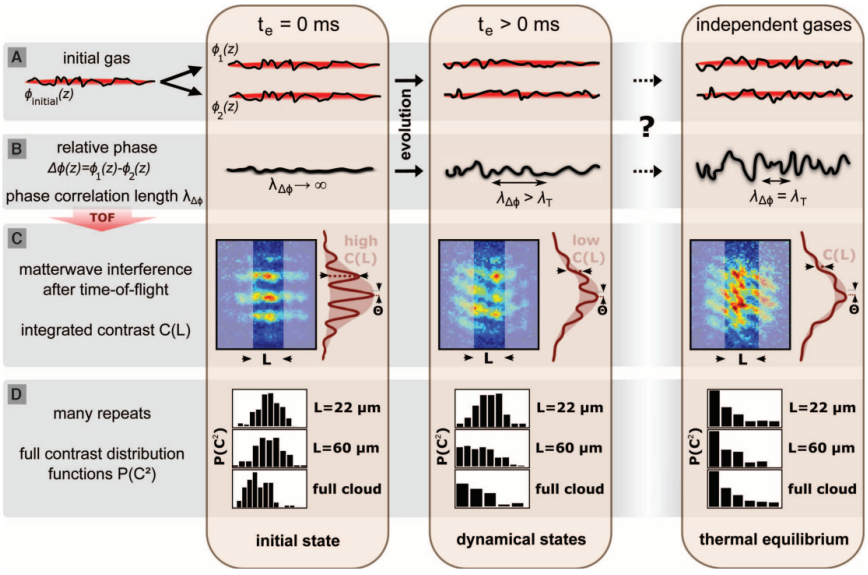

Figure 4.5: **Experimental Protocol**. (A) The initial gas is split quickly such that both gases have identical phase profiles at $t = 0$. At later times, the phases of each Bose gas will evolve in time until they are completely independent of each other as in independent gases. (B) The way to study the evolution of the phase profiles of each subsystem is through their phase difference. It is expected at thermal equilibrium that the phase difference profile becomes uncorrelated. (C) The interference contrast is measured by fitting a sine function with a gaussian envelope. The locally displaced interference pattern is the result of the differences in the local relative phase. (D) After many measurements of the contrast, one can have a probability distribution of $\hat{C}^2$. The figure is taken from ref [33].

Starting with the setup, the experiment starts by creating a 1D Bose gas of ^{87}Rb in the quasicondensate regime, which is described by the Luttinger-liquid model. The 1D gas was prepared in an elongated microtrap on an atom chip. We will not discuss any details about the atom chip since our setups will entirely be created optically. The main goal of the experiment was to study the equilibration process and to check if the prethermal phase exists. Since the thermal state of 1D Bose gas is characterized by completely random local phases, one way to study equilibration is to start with a well known phase along the 1D Bose gas and study how the local phases evolve. This way was done by taking 1D Bose gas and by quickly splitting it into two 1D Bose gases, which have almost identical phase profiles. Later, the 1D Bose gases are left to evolve in time before measurement. Once the goal is about studying phases, one usually aims for interference measurements

and quantities to probe the system. In our case, the quantity of interest that will probe the phase fluctuations is the mean squared of the interference contrast C, which has its equation shown below. The interference contrast can be measured from the interference fringes as seen in the experimental protocol illustrated in figure 4.5.

$$\hat{C}^2 = \left| \int_{-l/2}^{l/2} \mathrm{e}^{-\mathrm{i}\hat{\phi}_\mathrm{s}(z)} \right|^2 dz$$

Studying the thermalization of a system requires putting it out of equilibrium, which is inherently found in the splitting process. The splitting process was done much faster than the speed of traveling correlations $t_{\mathrm{split}} < \xi/c$, where $\xi = \hbar/mc$ is the healing length. Thanks to the quick splitting, each small segment of the 1D Bose gas undergoes independent splitting that causes a binomial distribution of the density of particles between the two resulting Bose gases; the binomial distribution is known as quantum shot noise and introduces energy only to the *relative* degrees of freedom. Thus, studying the contrast, which probes the *relative* phase, is perfect for studying the dynamics. After some evolution time, the measurement is done by turning off the trap and allowing the Bose gases to expand and interfere in a time-of-flight. Figure 4.6 shows the measurement process.

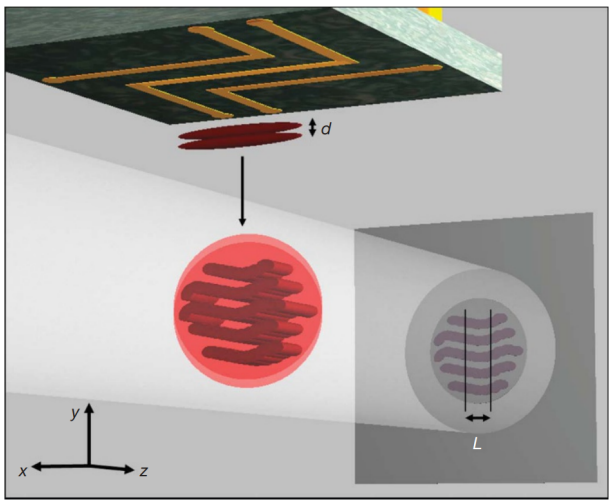

(a) The measurement process of imaging after a time-of-flight interference and of taking a length integration L from the image.

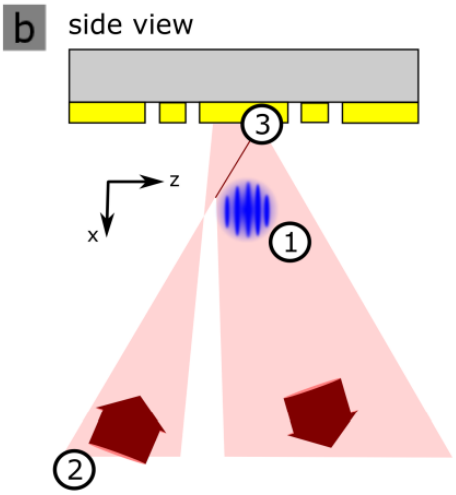

(b) A reflection imaging method.

Figure 4.6: **Measurement Method**. (a) The measurement is done by turning off the trap and allowing the Bose gases to expand as they fall due to gravity. The interference is imaged by sending a beam through the cloud onto a CDC camera. The beam is sent in the transverse direction of the 1D Bose gas in this picture, which is taken from another experiment that used the same technique. The subfigure is taken from ref [32]. In the experiment we are reviewing, the beam is sent longitudinally to integrate the absorption amplitude along the axial direction. The downside of longitudinal imaging is the time needed for collecting a data set of each integration length L. (b) Another measurement scheme is a reflection imaging method, where the length integration is done post-processing. In step 1, the 1D gases fall, expand, and interfere. In step 2, a beam is sent with a specific focus such that it passes once through the gases upon reflection in step 3 in the image. The subfigure is taken from ref [33].

Unlike the quantum Newton's cradle experiment, there was only one 1D Bose gas that allows us to measure the entire distribution of the observable instead of just the expectation value, which allowed the computation of $\langle \hat{C}^2 \rangle$ from the data of the interference contrast . One can see the equilibration process in figure 4.7. The measured observable $\langle \hat{C}^2 \rangle$ showed a rapid decay at the start due to dephasing. A prethermal state was then reached that was described pretty well by a gibbs ensemble of an effective temperature given by $T_{\text{eff}} = \frac{\hbar n_{1D} c \pi}{4K}$; furthermore, the effective temperature was independent of the initial state

temperature. To understand the reason, recall the conserved quantities N_k of each mode k of the Luttinger liquid model discussed in section 4.3.1. The reason for the effective temperature is that each relative mode k was given equal energies $E_k = \frac{\hbar n_{1D} c \pi}{4K}$ by the quantum shot noise; as a result, one can extract a temperature using the equipartition theorem. Since the single temperature used to describe the whole prethermal state is not the same temperature as the initial state, it can be thought of as a GGE with a single Lagrange multiplier λ_k. All the thermal energy before is given to the common mode degrees of freedom. After prethermalization, a further slow decay is observed that leads the system to thermalization; however, its rate corresponds to that of the technical heating of the system. This correspondence makes it inconclusive to determine if a near-integrable system relaxes further toward a thermal equilibrium on its own. In summary, a prethermal state exists for integrable systems. In the inset of figure 4.7, the experiment also showed the probability distribution for different integration lengths. Surprisingly, the smaller the system the better it retains a memory of its initial conditions as can be seen from the non-vanishing peak in small lengths. It can also be seen how the red curve representing the generalized gibbs ensemble reaches the blue thermal curve faster in the full cloud. This may hint toward how GGE is better for describing smaller subsystems.[33]

Generalized Gibbs Ensemble

After one year of Kinoshita's results, Rigolt et al. were able to show that an integrable system of hard-core bosons in 1D lattice can reach an equilibrium state that can be described by GGE; his work supports the idea that the GGE can describe integrable systems.[30] Based on similar studies, a follow-up experiment of the prethermalization one was done to verify the existence of a prethermal state. Although an effective temperature, which is not equal to that of the initial state, was used to describe the prethermal state and was seen as a hint of GGE, one would able to surely verify the existence of the GGE if a state with multiple Lagrange multipliers was created.

In the previous experiment, the splitting process was too fast that the quantum shot noise gave the same energy to all relative modes k; the equal energies given are the reason for the same effective temperature for all Lagrange multipliers. Therefore, changing the splitting process may result in having different Lagrange multipliers to different occupation numbers N_k, and the change in the splitting process is the main ingredient to measure a GGE with multiple Lagrange multipliers.

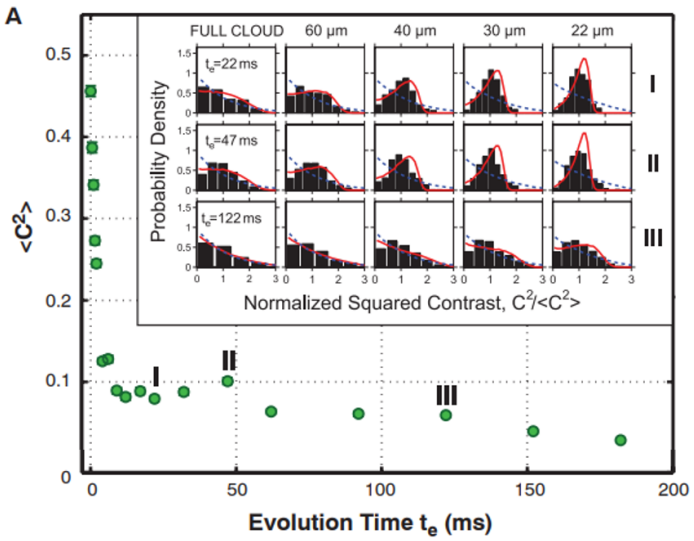

Figure 4.7: **Experimental Observation of Equilibration Process**. In this figure, a fast decay due to dephasing is observed in phase I. In phase II, a quasi-steady state is reached where it experiences very slow decay. In phase III, the system slowly decays further at the same rate as the heating of the system; thus, the approached thermal state isn't known to be from the near-integrability or the technical heating of the system. The inset shows the distribution of the data compared to that of a thermal state represented by the blue curve and a GGE represented by the red curve; these are done for different lengths of the 1D Bose gas. The figure is taken from ref [33].

The experiment was again done on an atom chip using rubidium atoms. It was also studied in the quasicondensate regime. After the splitting and some time evolution t, the measurement was done by time-of-flight interference as before; however, the data was used at this time to compute the correlation functions, which can be used to determine the Lagrange multipliers for the occupation modes.

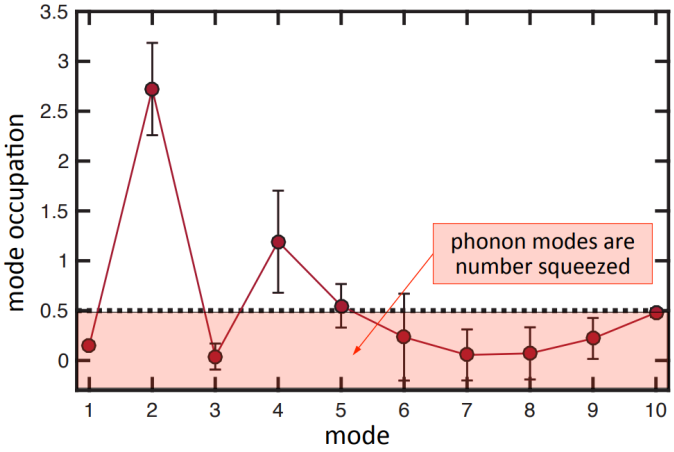

Figure 4.8: **Observation of Different Lagrange Multipliers**. The figure shows the occupation numbers N_k (in units of $\hbar\omega_k/\mu$) of the quasi-particle modes, where μ is the chemical potential and ω_k is in equation 4.16. The even occupation numbers increases with respect to that of the initial splitting protocol represented by the dashed line. On the other hand, a decrease is seen in the odd modes. Different occupation numbers indicate different Lagrange multipliers.The figure is taken from ref [8].

Freely fitting the occupation number N_k to explain the experimental data results in the graph in figure 4.8. The different splitting process or the modified quench protocol results in an increase in the even mode occupation numbers compared to that of the initial splitting while a decrease is seen in the odd ones. Different occupation numbers lead to different Lagrange multipliers; thus, the GGE is observed.[39]

Breaking Integrability

Dipolar Quantum Newton's Cradle

The art of experimental physics can be viewed as a way of creating a knob to control an intriguing physical phenomenon; things will never be well understood until we explore all regimes and poke every detail in the interesting physics. After verifying the integrability, prethermalization, and the GGE, it is only natural to think about how to break integrability. How one would have a knob to switch smoothly between integrability and non-integrability or, in other words, between having a prethermal state and just directly

reaching a thermal state. One experiment tried to achieve this knob by using dipole-dipole interaction (DDI) since its strength can be controlled based on the direction of the applied magnetic field. In a three-body interaction involving a DDI, the momenta of particles may change in a diffractive way instead of just swapping momenta as in the integrable case. Not much details of the DDI will be discussed since these won't be used for cesium and lithium atoms due to their low dipole moment. The setup of the experiment was similar to that of the original quantum Newton's cradle. A BEC of dysprosium atoms, which were chosen because of their large dipole moment, was loaded into a 2D lattice to create an array of 1D Bose gases. Note that the DDI can diffract momenta while not having the three particles in the same tube; two particles may collide in one tube while having a long-range DDI with a particle in another tube. The 1D Bose gas was put out of equilibrium in the same way by applying two pulses of standing waves to create two Bose gases with equal, opposite momenta, where their collisions will never excite any atoms to the excited transversal state. After the pulses, the Bose gases are left for some time evolution at a specific direction of the magnetic field that tunes the interaction. Figure 4.9a shows a schematic of four 1D Bose gases with an interaction strength that varies based on the angle between the magnetic field and the direction connecting different tubes.

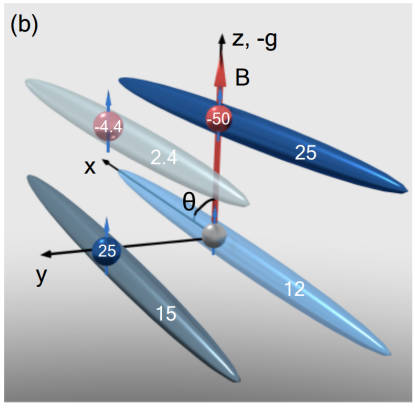

(a) A schematic of four 1D gases with a defined magnetic field that tunes the interaction.

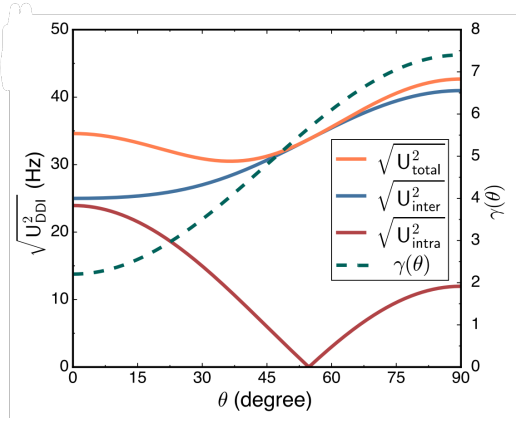

(b) Strength of different kinds of DDI.

Figure 4.9: **The Role of the Magnetic Field in the Setup**. (a) The magnetic field defined by the angle θ between its direction and the axial axis of the tubes controls the interaction. The numbers on the sphere indicate the pair-wise DDI strength while the numbers on the tubes indicate the integrated DDI strength. It can be seen that the interactions between the tubes are not isotropic. (b) The graph shows the interaction strength of different types of DDI as a function of θ. Intratube DDI energy U_{intra} is the interaction between the atoms in the same tube; it vanishes at 55°. The intratube interaction energy reflects the DDI strength coming from all nearby tubes. The energy U_{total} reflects the strength coming from both the intertube and intratube interactions; it shows us that the integrability-breaking interaction can never be turned completely off. Finally, the DDI has a short range interaction that affects the contact strength in the Lieb-Liniger model. The figures are taken from ref [34].

The measurement is done by first deloading the lattice slowly compared to the band excitation timescale but fast compared to the 3D trap thermalization timescale. It is done slowly with respect to the band excitation state to perform an adiabatic mapping from the quasimomentum states to the real momentum states. After the mapping, the whole trap is turned off for a time-of-flight measurement. Unlike the original quantum Newton's cradle, it was not a 1D expansion since releasing the confinement alleviates any effects due to the interactions. The momentum distribution was measured for multiple directions of the magnetic field. Regarding the momentum distributions, figure 4.10a shows the results. It shows that the system always thermalizes; this thermalization always takes a different duration depending on the angle, and its timescale is always longer compared to a 3D gas

that experiences that same quench.

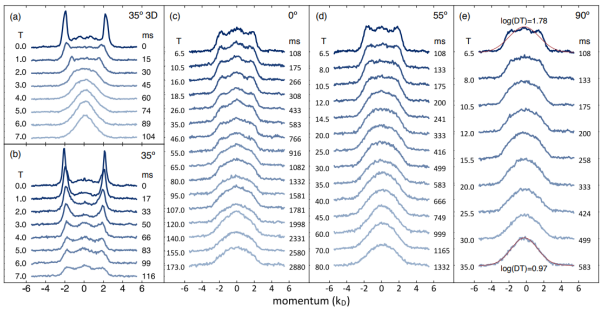

(a) The evolution of the momentum distribution in time for different magnetic field directions denoted by θ

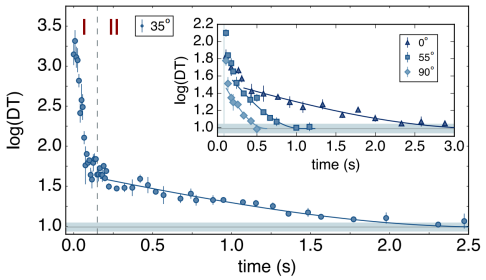

(b) Time evolution of the observable DT, which is a distance-to-thermalization of the measured momentum distribution. It is the distance to the closest gaussian fit.

Figure 4.10: **Momentum Distribution Results**. (a) The evolution of the momentum distribution at different times at different θ's. All the momentum distributions reach a thermal distribution mainly because the DDI interactions strength can never be completely turned off as can be seen in figure 4.9b. (b) The graph shows the equilibration process defined by two regimes. Regime I defines the fast dephasing phase. At the end of this regime, the system can be described using GGE. In regime II, the system keeps decaying to a thermal state. The inset shows the decay for different angles in this regime. The figures are taken from ref [34].

Furthermore, the study compared each momentum distribution at each time to the closest gaussian fit; this distance is known as the distance-to-thermalization metric. This observable was studied and plotted as can be seen in figure 4.10b. It can be seen that the graph is divided into two regions. In region I, a fast decay due to dephasing is seen. It was concluded that this dephasing is due to anharmonicity in the presence of interactions but in the absence of high-energy collisions like the head-on ones here. This can be seen as a limitation similar to that of the original quantum Newton's cradle since the dephasing is not purely due to the interactions of the system. In region II, the experiment was able to show that the further decay was due to the near-integrability since the rate at the start of this region was different from the heating of the system. How fast a thermal state can be reached depends on the direction of the magnetic field that causes the perturbation to the Lieb-Liniger model. A limitation of this experiment is the lack of a complete turn-off of the perturbation as can be seen in figure 4.9b. In conclusion, the integrability can be

broken in the Lieb-Liniger model, and the relaxation towards a thermal state happens in a near-integrable system.[34]

Breaking Integrability through Transverse Excitations

Another way to break integrability is through the excited transverse states, which can contribute to redistributing the momenta distribution. This quantum Newton's cradle experiment is a significant improvement of the original one for the following reasons. The first reason would be the negligible loss of atoms that allowed them to observe up to 10 times more oscillations than the original one. A second reason is the use of transverse states to break integrability. It was shown that a near-integrable system as that of the original experiment eventually reaches a thermal state. Another result is the faster decay toward thermal equilibrium as more atoms access the transverse excited states.

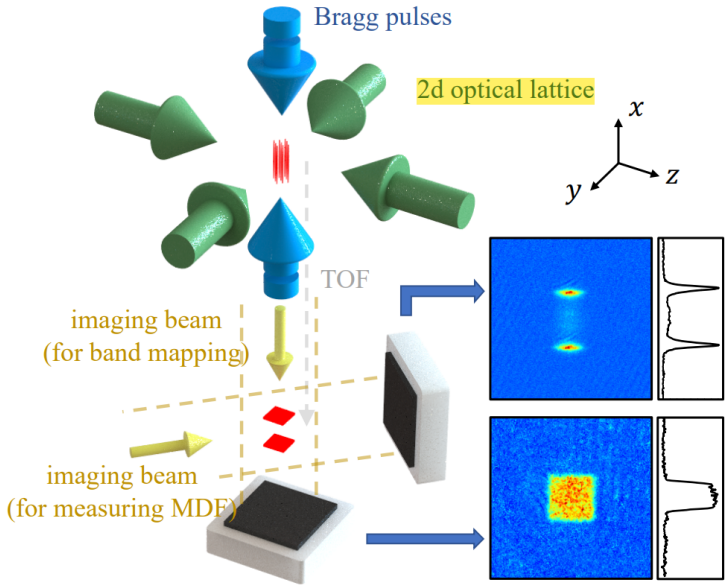

Figure 4.11: **Experimental Setup**. A 2D lattice is created in the y-z plane, where its eigenstates can be solved by Bloch's theorem. The Bragg pulinteractionthe x-direction diffract atoms to opposite, equal momenta states. After time-of-flight expansion, imaging through either the longitudinal or the transverse direction is done. The longitudinal direction shows the population of atoms in the transverse state while the transverse direction measures the longitudinal momentum distribution. The figure is taken from ref [47].

Starting with the experimental setup, a 2D optical lattice was created using two standing waves that are detuned from each other to avoid interference. The lattice lasers also provide a weak axial confinement, creating the 1D tubes. To take the system out of equilibrium, a sequence of Bragg pulses, which are two standing wave pulses, is sent to diffract the atoms among a series of momentum states $\pm 2n\hbar k$, where n is just an integer. Instead of having only $\pm 2\hbar k$, access to higher momentum states allows the control of the fraction of atoms that can get excited in the transverse harmonic confinement. To measure the momentum distribution, a time-of-flight expansion is followed by imaging in either the longitudinal or transverse direction. Figure 4.11 shows the setup of the system. Longitudinal imaging is used to measure the fractional population of atoms in the transverse states. Transverse imaging is used to measure the longitudinal momentum distribution.

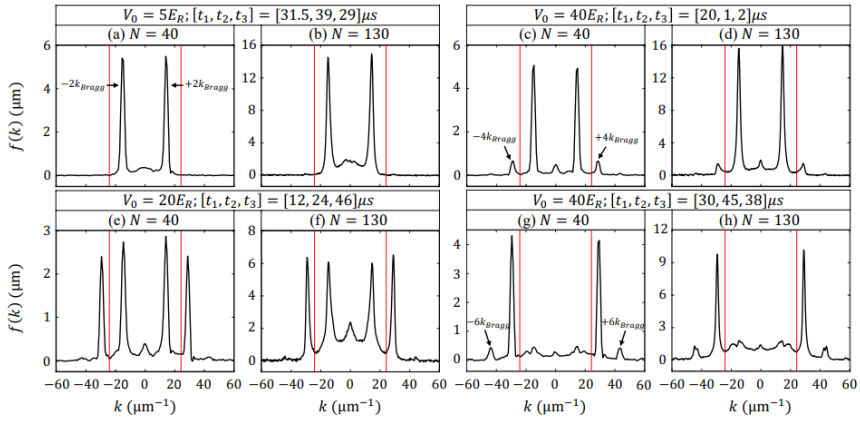

Figure 4.12: **Initial Momentum Distributions**. The initial longitudinal momentum ditribution is experimentally measured for different Bragg pulse sequences. A Bragg pulse sequence is defined not only by the wavevector k_{Bragg} but also by the pulse intensity V_0 in units of $E_R = (\hbar k_{\text{Bragg}})^2/2m$. It is also important to specify the time sequence for the duration of the pulses denoted by t_1 and t_3 and the duration of the gap between them t_2. In the figure, the vertical line corresponds to the threshold momentum k_{th}, at which two atoms can populate the excited state $E_{th} = 2\hbar\omega_\perp$ upon head-on collisions. Finally, N is the number of particles. The figure is taken from ref [47].

For the results, we begin by showing how the near-integrable 1D Bose reach thermalization given that the head-on collisions don't have enough energy to populate the excited transverse state. We start by checking the evolution of the momentum distribution for the initial distribution of (a) and (b) in figure 4.12. The evolution is shown in figure

4.13. It can be seen that the images get blurry as time evolves due to the dephasing of the anharmonicity. Furthermore, it can be seen that both systems seem to completely dephase on similar time scales as can be seen from the density images at 720 ms. Unlike the original quantum Newton's cradle experiment, it can be seen that the 1D Bose gas of N=130 eventually thermalizes by having a gaussian distribution. It is conjectured that this thermalization is due to the scattering between the atoms in the ground transverse state and the much fewer atoms in the excited state.[47]

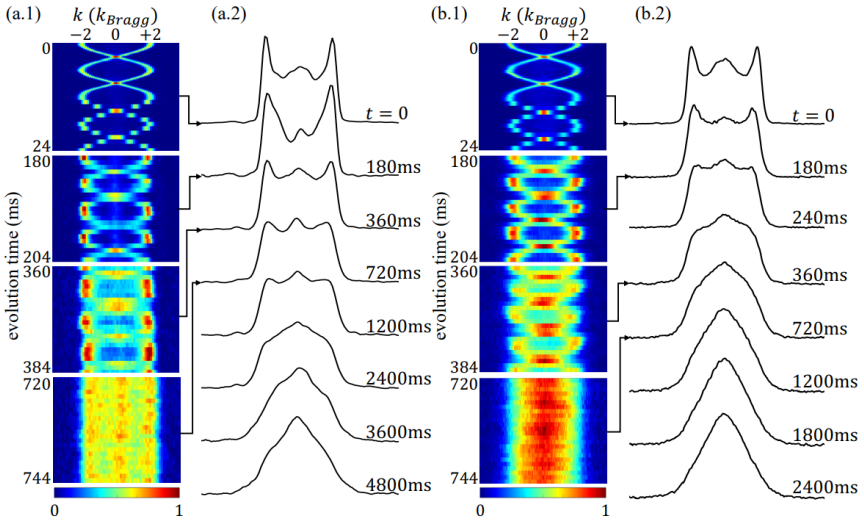

Figure 4.13: **Results of Near-Integrability**. In this figure, the time evolution of the momentum distribution is shown for the distributions (a) and (b) in figure 4.12. For these distributions, the system is near-integrable. The parts of the graph (a.1) and (b.1) show the observations taken of the longitudinal momentum distribution. They both completely dephase at about 720ms where no significant change in the distribution happens after one oscillation. The other parts of the graph (a.2) and (b.2) show the time evolution of the momentum distribution averaged over the oscillation period. The figure is taken from ref [47].

Finally, we will explore the effect of the population of atoms in the excited transverse state on the relaxation towards a thermal state. The observable that will be studied is $\mathcal{R}(t)$, which is the summed square of residuals between the oscillation period averaged momentum distribution and its best gaussian fit. It is quite similar to the distance-to-thermalization metric used in the dipolar quantum Newton's cradle. The time evolution of $\mathcal{R}(t)$ is shown

in figure 4.14 where the letters correspond to the initial momentum distributions in figure 4.12. The more atoms that cross the red vertical line of the threshold momentum in figure 4.12, the faster the decay toward a thermal state. In conclusion, controlling the population of atoms that can access the transverse excited states will control the rate of thermalization. [47]

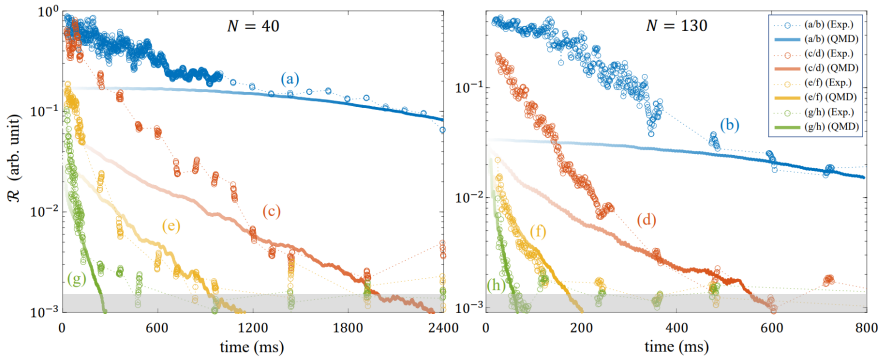

Figure 4.14: **Results of Integrability-Breaking**. This figure corresponds to the initial momentum distributions in figure 4.12. It clearly shows the faster decay of $\mathcal{R}(t)$ as the population of atoms accessing the excited states increases. The figure is taken from ref [47].

4.3.2 Bose-Hubbard Model

Unlike the Lieb-Liniger model, the Bose-Hubbard model will have its experiments and theoretical background discussed very briefly. The reason is that no experiments in the near future will be done to study this system for thermalization. However, only one experiment will be discussed in more detail since its technique will be used in our experiments and since it will provide supporting arguments for our approach to study thermalization.

Introduction

The Bose-Hubbard model has a simple Hamiltonian that surprisingly doesn't have an analytical solution when both the tunneling term J and interaction term U are non-zero

and non-perturbative. The Hamiltonian is:

$$H_{\mathrm{BH}} = -J \sum_{\langle i,j \rangle} \hat{a}_i^\dagger \hat{a}_j + \frac{U}{2} \sum_i \hat{n}_i \left(\hat{n}_i - 1 \right) \tag{4.17}$$

This Hamiltonian describes the physics of particles in a deep lattice. The first term is known as the tunneling term in the sense that it removes one particle from a lattice site using the annihilation operator and creates one in a neighboring site using the creation one. The second term is known as the interaction term in the sense that the energy increases as the number of particles in a site increases. It is important to know always how to create this Hamiltonian using our ultracold atoms. It is created by a deep lattice from a standing wave. It needs to be deep since the Hamiltonian depends on what is called the tight-binding approximation. In this approximation, the lattice is deep enough that the overlap between the Wannier states is small enough that only the nearest-neighbor interaction matters. Wannier states are the Fourier transform of the Bloch states, and they are as localized as they can be. For more details, we refer the reader to the following reference.[41] From these small details above, one can find that the tunneling factor can be controlled by the lattice depth. The interaction term can be controlled by the Feshbach resonance.

Regarding the integrability of the Bose-Hubbard model, the Hamiltonian is non-integrable. It is non-integrable in the sense that it can thermalize. We refer the reader to the following extensive study that shows to what extent the canonical and microcanonical ensembles can describe the system. It considered many factors during this study from the system's size to the strength of the quench.[40] Regarding experimental studies, we refer the reader to a small portion of experiments done in this model.[42,43]

Entanglement Entropy in Bose-Hubbard Model

The idea of using statistical mechanics, which uses certain mixed states, to predict a pure state works nicely, but it is not clearly justified.[48] A possible justification for the use of a mixed state to a pure state can be seen through entanglement since an entangled many-body pure state has its subsystems described by a mixed state. For example, the simple state of $|\psi\rangle = \frac{1}{\sqrt{2}}(|00\rangle + |11\rangle)$ will have its subsystems described by the following mixed state:

$$\rho_A = \mathrm{Tr_B}(\rho_{\mathrm{AB}}) = \mathrm{Tr_B}(|\psi\rangle\langle\psi|) = \frac{1}{2}(|0\rangle\langle 0| + |1\rangle\langle 1|)$$

Following this motivation, an experiment was done to show how the thermal behavior appeared locally in the Bose-Hubbard model in the superfluid regime $\frac{U}{J} << 1$, where the tunneling effect is enhanced causing spatial entanglement. When $\frac{U}{J} >> 1$, the ground state of the Bose-Hubbard model is in a Mott insulator state with unity filling of the lattice sites, which can be verified by setting $J = 0$ in equation (4.17).

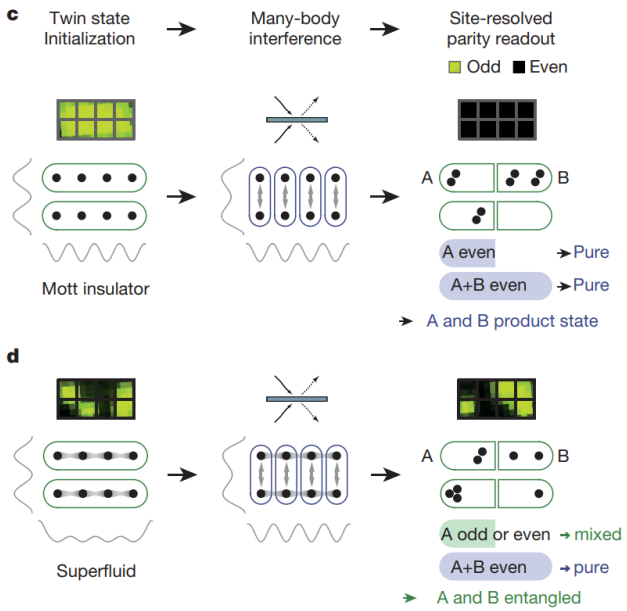

Figure 4.15: **Measurement Method**. The measurement of purity is done by an interference between a single site of one system with the corresponding site on the identically prepared system. (c) A Mott insulator state with unit filling is prepared. An interference between the sites of each system is done to measure the number parity. A measurement of the number of particles will show an even number of particles in the subsystem since the Mott insulator doesn't have any spatial entanglement. (d) The same sequence is done for a superfluid state, which is characterized by its spatial entanglement. After measurement, subsystems will show odd numbers indicating a mixed state due to entanglement. To compute the purity of the whole pure state, we add the particle numbers of each subsystem; the total particle number will be even indicating that the whole quantum system remains pure. The figure is taken from ref [49].

In this elegant experiment, a way was shown to measure entanglement entropy, more

specifically the 2nd-order Renyi entanglement entropy:

$$S_2(\rho_A) = -\ln \mathrm{Tr}\left(\rho_A^2\right) \tag{4.18}$$

It is elegant due to its simplicity in the measurement, where only a 50-50% beam splitter was used to interfere two identical and independent copies of the system. The whole goal was to measure quantum purity $\mathrm{Tr}(\rho_\mathrm{A}^2)$ since it is sufficient to prove entanglement by showing that subsystem A is less pure than the entire system:

$$\mathrm{Tr}\left(\rho_A^2\right) < \mathrm{Tr}\left(\rho_{AB}^2\right)$$

It can be seen how quantum purity is related to the Renyi entropy. This theoretical quantity was related experimentally to the number parity P:

$$\langle P_i \rangle = \mathrm{Tr}\left(\rho^2\right)$$

where i represents a specific lattice site of the system. Note that $P = 1$ for an even number and $P = -1$ for an odd number. Given how the theoretical quantum purity is related to the number parity, the whole experiment was about preparing identical states in the Bose-Hubbard system and then about performing interference measurements between individual lattice sites of one system with the corresponding ones on the other system. Pure states will only lead to an even number of particles in the outputs while a mixed state may lead to an odd number. Figure 4.15 illustrates the process, and figure 4.16 shows the entanglement measurements.[49]

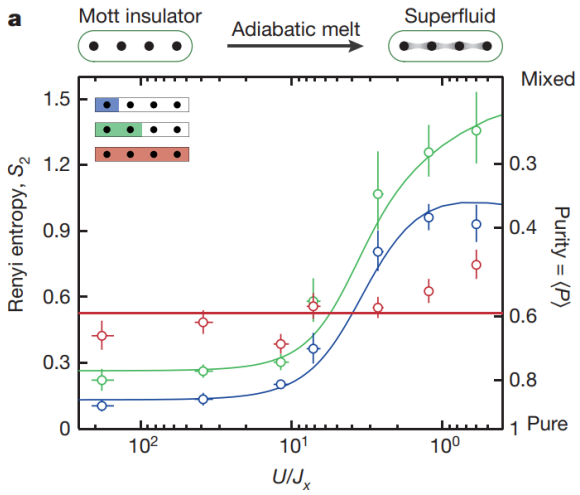

Figure 4.16: **Measurements of Entanglement Entropy**. The Renyi entropy is measured for different subsystems as the parameter U/J is adiabatically reduced. In the superfluid phase, the subsystem has an entanglement entropy higher than the total system due to the spatial entanglement. In the Mott insulator phase, the subsystem has less entanglement entropy. Note how the Renyi entropy for the full system is always fixed. Solid lines are theoretical while circles are data points. The figure is taken from ref [49].

To study thermalization, a quench was made from a Mott insulator state with unity filling to a weakly interacting regime of $U/J = 1.56$. Three main results were observed. The first one is the increase of the entanglement entropy in a subsystem after the quench; it is shown in figure 4.17a. Furthermore, it agrees well with the thermodynamical entropy for small subsystems.

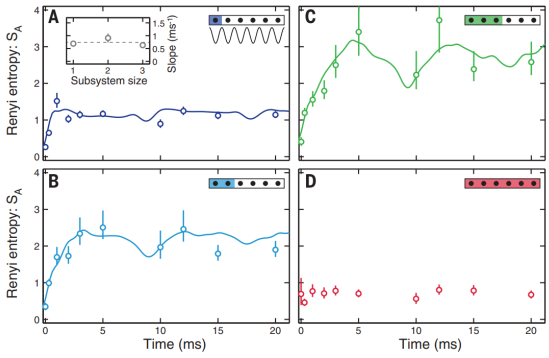

(a) Dynamics of the entanglement entropy for different subsystem sizes.

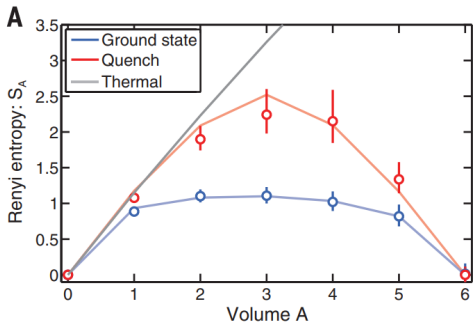

(b) Comparison between the entanglement entropy of the saturated quenched state and the canonical thermal ensemble.

Figure 4.17: **Entanglement Entropy after Quench**. (a) It can be seen how the entanglement entropy increases in the subsystems while it is constant in the whole system. (b)The entanglement entropy for the saturated quench state agrees very well with that of the canonical ensemble. The figures are taken from ref [50].

The second result is the comparison between the reduced density matrix of a site from the saturated quench state and the canonical ensemble. This was done by computing two quantities: the trace distance and the fidelity. The fidelity measures the overlap of density states while the trace distance shows an effective distance between these mixed states in Hilbert space. An agreement between two density operators will have a fidelity of 1 and a trace distance equal to zero. These quantities show how local thermal states emerge. Figure 4.18 shows the results.

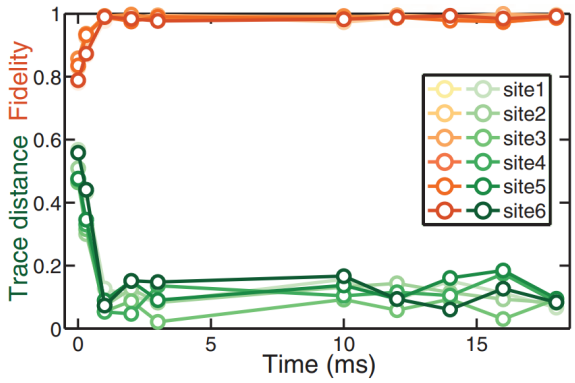

Figure 4.18: **Fidelity and Trace Distance**. Comparing the reduced density matrix of each site to the reduced density matrix from a canonical ensemble. The time evolution of the fidelity and trace distance shows how the reduced density operator agrees well with that of the canonical ensemble; thus, local emergence of thermalization is observed. The figure is taken from ref [50].

Finally, an emerging local thermal state leads to the natural result that the local observables calculated using pure states agree with ones of statistical mechanics. Furthermore, the experiment also showed how the expectation value of the full system interaction energy, which is a global quantity, agrees with the one from a canonical ensemble.[50]

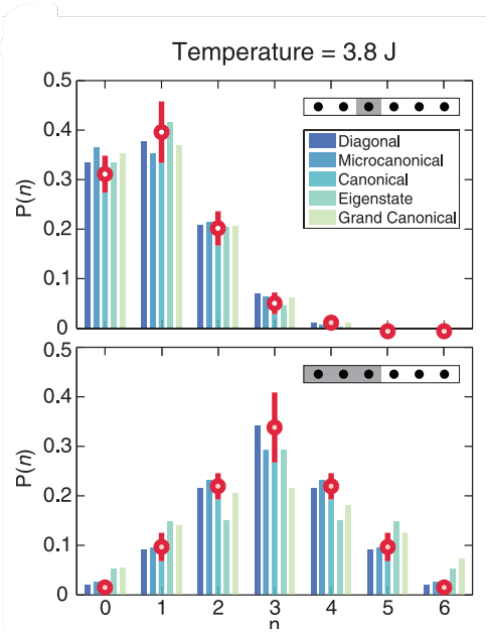

(a) Comparison of atom number distribution between measurements and predictions of thermodynamical ensembles.

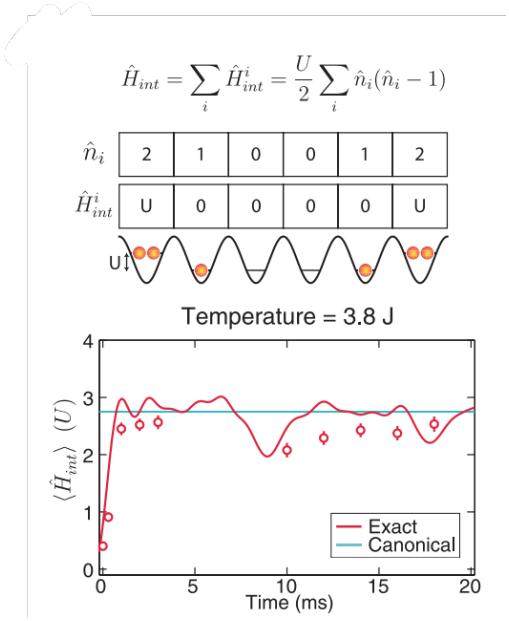

(b) Measurement of the total interaction energy, which is a global observable.

Figure 4.19: **Measurement of Local and Global Observables**. (a) The given temperature is achieved by the quench. One can see how the measured number distribution agrees with different kinds of thermodynamical ensembles. (b) One would expect that only local observables can be described by the thermodynamical ensembles due to the local emergence of a thermal state; however, it can be seen that global observables also agree with the result of the canonical ensemble. The figures are taken from ref [50].

4.4 Subsystem-Bath Approach

Previous experiments mainly provided evidence of what is expected such as integrability, GGE, and integrability-breaking perturbations. It is now the time to use these tools to understand the fundamental physics behind thermalization. We want to be able to have a theory that could predict the thermodynamics of the system by just knowing its Hamiltonian. To plan our experiments, we want to figure out the theoretical approach and to show the experimental techniques that will be used to overcome the discussed

limitations. We start by showing why the subsystem-bath approach is promising and how we would study that experimentally.

Motivation

Applying classical statistical mechanics to quantum systems is a problem since the derivations of ensembles like the canonical one depend on thermodynamics that we know works in the classical limit. The second law of thermodynamics about entropy, which can be defined from the Carnot cycle as a conserved quantity, is a classical law. If it is true also in the quantum regime, one in principle can derive it using quantum mechanics. Luckily, one can derive the second law of thermodynamics from the Markovian Master Equation (MME), which describes the open quantum systems under certain conditions. Note that the entropy in quantum mechanics is usually the Von-Neumann entanglement entropy:

$$S = -\operatorname{Tr}(\rho \ln \rho)$$

This quantity is the first order Renyi entropy related to the 2nd-order in equation 4.18. It can be used to quantify entanglement hence the name entanglement entropy. If a subsystem is in contact with a bath of temperature T, one can show using the MME that the subsystem will reach a steady state described by the canonical ensemble having the bath's temperature T.[7,44]

Although the problem of thermalization is mainly about closed systems, the results from studying open quantum systems hint that the answer may be in the subsystem-bath approach. In this approach, we divide our closed system into a small subsystem and a much larger one that we see as a bath and start studying their interactions together. This approach is supported by some numerical and experimental studies. In a numerical study, it was shown for a pure non-integrable system that the entanglement entropy was calculated for a subsystem in two different ways. One way was through the reduced density matrix generated by taking the partial trace over an eigenstate while the other way was taking the partial trace over the microcanonical ensemble. Both ways gave the same result.[45] Experimentally, the Bose-Hubbard model experiment showed how a thermal state emerges in a subsystem.[50] The subsystem-bath approach can be supported further through arguments related to the generalized gibbs ensemble. It was pointed out that the GGE is used for local observables in the long time limit.[8] It was also shown that the lack of entanglement in the energy eigenbasis leads to the outcome that all local observables retain a memory of their initial state when they equilibrate.[46] Since the GGE is always linked to local

observables, focusing on subsystems seems to be the right way to study thermalization in a closed system.

After figuring out the theoretical approach, the next question is what tools will be used to probe our systems experimentally. Given the experimentally shown overlap of the subsystem and the canonical ensemble and the effect of the lack of entanglement, we believe that the thermalization of quantum systems can be explained through entanglement. In conclusion, studying thermalization in the subsystem-bath approach can be done through implementing entanglement entropy measurements.

Experimental Plans

Our future experiments will mainly study the Lieb-Liniger model for various reasons. First, it is much easier to break integrability than to build one, which is why we focused on the Lieb-Liniger model rather than the Bose-Hubbard model. Another reason is that the Lieb-Liniger model has an exact analytical solution.

After understanding the previous work, we plan to overcome the limitations seen in previous experiments. For example, all quantum Newton's cradle experiments faced the problem of dephasing due to the anharmonicity of the trap; this "technical" dephasing is the main reason for the fast decay at the start of the equilibration process. We believe that we can study the Lieb-Liniger model without any anharmonicity. To avoid the technical dephasing, we plan to trap our bosons in 1D rings because the intensity would have a circular symmetry. The 1D rings in principle can be created in two steps. The first step will be using a Bessel beam that would create a hollow cylinder trap for the atoms. The second step would be cutting this cylinder into many thin rings using a standing wave. The intensity in the ring will have a circular symmetry, which would be the reason for not having any technical dephasing. The frequency and intensity of the optical traps will be controlled by the AOM. Creating 1D ring traps will be interesting for two reasons. The first reason will be experimentally achieving truly periodic boundary conditions. Understanding the bulk properties of this system under periodic boundary conditions is one of our short-term goals. Another reason would be controlling the transition between the integrability and the non-integrability of the system through the thickness of the rings. Having the perfect knob between integrability and non-integrability is another short-term goal. A longer-term goal would then be to deeply understand the correlation between thermalization and entanglement. To study that, we will research a way to implement entanglement entropy

measurements on the 1D rings.

Unlike the other experiments that mainly depended on optical means to control the Hamiltonian, we have extra tools that may help us quench and probe the system better. For example, the Feshbach resonances, which will be controlled by the current controller, will be used to change the interaction strength between particles. We can even use that during time-of-flight measurements to cancel any interaction effects and thus never worry about how interactions may affect our measurements of the momentum distribution. We can use this tool to understand the effect of interactions on the expansion of particles during measurements. Another tool is the available mixture of atoms we have, which can be used as a cooling technique by using one kind to absorb the entropy from the other one. We can also create arbitrary potentials using SLM or DMD. Regarding measurements, we would be able to measure the position of single atoms using a quantum gas microscope.

In conclusion, our new lab will have the means to provide new answers to the problem of thermalization and shed light on the thermodynamics of various systems from different fields due to the ability of ultracold atoms to be an efficient simulator.

References

1. L. D'Alessio, Y. Kafri, A. Polkovnikov, and M. Rigol, From Quantum Chaos and Eigenstate Thermalization to Statistical Mechanics and Thermodynamics, Adv. Phys. 65, 239, 2016

2. Jaynes, E.T., 1957. Information theory and statistical mechanics. Physical Review, 106(4), pp.620–630.

3. Jaynes, E.T., 1957. Information theory and statistical mechanics. II. Physical Review, 108(2), pp.171–190.

4. Gogolin, C. and Eisert, J., 2016. Equilibration, thermalisation, and the emergence of statistical mechanics in closed quantum systems. Reports on Progress in Physics, 79(5), p.056001.

5. Short, A.J., 2011. Equilibration of quantum systems and subsystems. New Journal of Physics, 13(5), p.053009.

6. Short, A.J. and Farrelly, T.C., 2012. Quantum equilibration in finite time. New Journal of Physics, 14(1), p.013063.

7. Binder, F., Correa, L., Gogolin, C., Anders, J. and Adesso, G., 2019. Thermodynamics in the Quantum Regime. Cham: Springer

8. Langen, T., Gasenzer, T. and Schmiedmayer, J., 2016. Prethermalization and universal dynamics in near-integrable quantum systems. Journal of Statistical Mechanics: Theory and Experiment, 2016(6), p.06400

9. Greiner, W., Neise, L. and Stöcker, H., 2012. Thermodynamics and statistical mechanics. Springer Science & Business Media.

10. Kardar, M., 2007. Statistical physics of particles. Cambridge University Press.

11. Marion, J.B., 2013. Classical dynamics of particles and systems. Academic Press.

12. J. Chem. Phys. 84, 3147 (1986)

13. Penrose, O., 2005. Foundations of statistical mechanics: a deductive treatment. Courier Corporation.

14. P. Bocchieri and A. Loinger. Quantum recurrence theorem. Phys. Rev.,107:337-338, Jul 1957

15. H. Wilming, M. Goihl, C. Krumnow, J. Eisert, (2017)

16. Linden, N., Popescu, S., Short, A.J. and Winter, A., 2009. Quantum mechanical evolution towards thermal equilibrium. Physical Review E, 79(6), p.061103.

17. Farrelly, T., Brandão, F.G. and Cramer, M., 2017. Thermalization and return to equilibrium on finite quantum lattice systems. Physical Review Letters, 118(14), p.140601.

18. Peng, P., Yin, C., Huang, X., Ramanathan, C. and Cappellaro, P., 2021. Floquet prethermalization in dipolar spin chains. Nature Physics, 17(4), pp.444-447.

19. Lieb, E.H. and Liniger, W., 1963. Exact analysis of an interacting Bose gas. I. The general solution and the ground state. Physical Review, 130(4), p.1605.

20. Chin, C., Grimm, R., Julienne, P. and Tiesinga, E., 2010. Feshbach resonances in ultracold gases. Reviews of Modern Physics, 82(2), p.1225.

21. Bruus, H. and Flensberg, K., 2004. Many-body quantum theory in condensed matter physics: an introduction. OUP Oxford.

22. Griffiths, David J. Introduction to Quantum Mechanics. Upper Saddle River, NJ: Pearson Prentice Hall, 2005

23. Zill, J.C., 2017. Nonequilibrium dynamics of a one-dimensional Bose gas via the coordinate Bethe ansatz.

24. Korepin, V.E., Bogoliubov, N.M. and Izergin, A.G., 1997. Quantum inverse scattering method and correlation functions (Vol. 3). Cambridge university press.

25. Bouchoule, I. and Dubail, J., 2022. Generalized hydrodynamics in the one-dimensional Bose gas: theory and experiments. Journal of Statistical Mechanics: Theory and Experiment, 2022(1), p.014003.

26. F D M Haldane 1981 J. Phys. C: Solid State Phys. 14 2585

27. Cazalilla, M.A., 2004. Bosonizing one-dimensional cold atomic gases. Journal of Physics B: Atomic, Molecular and Optical Physics, 37(7), p.S1.

28. Kinoshita, T., Wenger, T. and Weiss, D.S., 2005. All-optical Bose-Einstein condensation using a compressible crossed dipole trap. Physical Review A, 71(1), p.011602.

29. Wu, S., Wang, Y.J., Diot, Q. and Prentiss, M., 2005. Splitting matter waves using an optimized standing-wave light-pulse sequence. Physical Review A, 71(4), p.043602.

30. Rigol, M., Dunjko, V., Yurovsky, V. and Olshanii, M., 2007. Relaxation in a completely integrable many-body quantum system: an ab initio study of the dynamics of the highly excited states of 1D lattice hard-core bosons. Physical review letters, 98(5), p.050405.

31. Mora, C. and Castin, Y., 2003. Extension of Bogoliubov theory to quasicondensates. Physical Review A, 67(5), p.053615.

32. Hofferberth, S., Lesanovsky, I., Fischer, B., Schumm, T. and Schmiedmayer, J., 2007. Non-equilibrium coherence dynamics in one-dimensional Bose gases. Nature, 449(7160), pp.324-327.

33. Gring, M., Kuhnert, M., Langen, T., Kitagawa, T., Rauer, B., Schreitl, M., Mazets, I., Smith, D.A., Demler, E. and Schmiedmayer, J., 2012. Relaxation and prethermalization in an isolated quantum system. Science, 337(6100), pp.1318-1322.

34. Tang, Y., Kao, W., Li, K.Y., Seo, S., Mallayya, K., Rigol, M., Gopalakrishnan, S. and Lev, B.L., 2018. Thermalization near integrability in a dipolar quantum Newton's cradle. Physical Review X, 8(2), p.021030.

35. Schmiedmayer, J. and Berges, J., 2013. Cold atom cosmology. Science, 341(6151), pp.1188-1189.

36. Lahav, O., Itah, A., Blumkin, A., Gordon, C., Rinott, S., Zayats, A. and Steinhauer, J., 2010. Realization of a sonic black hole analog in a Bose-Einstein condensate. Physical review letters, 105(24), p.240401.

37. Essler, F.H. and Fagotti, M., 2016. Quench dynamics and relaxation in isolated integrable quantum spin chains. Journal of Statistical Mechanics: Theory and Experiment, 2016(6), p.064002.

38. Gangardt, D.M. and Shlyapnikov, G.V., 2003. Stability and phase coherence of trapped 1D Bose gases. Physical review letters, 90(1), p.010401.

39. Langen, T., Erne, S., Geiger, R., Rauer, B., Schweigler, T., Kuhnert, M., Rohringer, W., Mazets, I.E., Gasenzer, T. and Schmiedmayer, J., 2015. Experimental observation of a generalized Gibbs ensemble. Science, 348(6231), pp.207-211.

40. Sorg, S., Vidmar, L., Pollet, L. and Heidrich-Meisner, F., 2014. Relaxation and thermalization in the one-dimensional Bose-Hubbard model: A case study for the interaction quantum quench from the atomic limit. Physical Review A, 90(3).

41. Gerbier, F., 2017. Quantum Gases in Optical Lattices.

42. Trotzky, S., Chen, Y.A., Flesch, A., McCulloch, I.P., Schollwöck, U., Eisert, J. and Bloch, I., 2012. Probing the relaxation towards equilibrium in an isolated strongly correlated one-dimensional Bose gas. Nature physics, 8(4), pp.325-330.

43. Ronzheimer, J.P., Schreiber, M., Braun, S., Hodgman, S.S., Langer, S., McCulloch, I.P., Heidrich-Meisner, F., Bloch, I. and Schneider, U., 2013. Expansion dynamics of interacting bosons in homogeneous lattices in one and two dimensions. Physical review letters, 110(20), p.205301.

44. Breuer, H. and Petruccione, F., 2002. The theory of open quantum systems. Oxford [England]: Oxford University Press.

45. Deutsch, J.M., Li, H. and Sharma, A., 2013. Microscopic origin of thermodynamic entropy in isolated systems. Physical Review E, 87(4), p.042135.

46. Gogolin, C., Müller, M.P. and Eisert, J., 2011. Absence of thermalization in nonintegrable systems. Physical review letters, 106(4), p.040401.

47. Li, C., Zhou, T., Mazets, I., Stimming, H.P., Møller, F.S., Zhu, Z., Zhai, Y., Xiong, W., Zhou, X., Chen, X. and Schmiedmayer, J., 2020. Relaxation of bosons in one dimension and the onset of dimensional crossover. SciPost Physics, 9(4), p.058.

48. Rigol, M., Dunjko, V. and Olshanii, M., 2008. Thermalization and its mechanism for generic isolated quantum systems. Nature, 452(7189), pp.854-858.

49. Islam, R., Ma, R., Preiss, P. et al. Measuring entanglement entropy in a quantum many-body system. Nature 528, 77–83 (2015). https://doi.org/10.1038/nature15750

50. Kaufman, A.M., Tai, M.E., Lukin, A., Rispoli, M., Schittko, R., Preiss, P.M. and Greiner, M., 2016. Quantum thermalization through entanglement in an isolated many-body system. Science, 353(6301), pp.794-800.

51. Kinoshita, T., Wenger, T. and Weiss, D.S., 2006. A quantum Newton's cradle. Nature, 440(7086), pp.900-903.

52. Vivek, V., 1999. Optical Switches. [ebook] University of Arizona. Available at: ¡https://wp.optics.arizona.edu/milster/wp-content/uploads/sites/48/2016/0/acousto-optics-modulator.pdf¿ [Accessed 9 September 2021].

53. A. Korpel, "Acousto-optics—A review of fundamentals," in Proceedings of the IEEE, vol. 69, no. 1, pp. 48-53, Jan. 1981, doi: 10.1109/PROC.1981.11919.

54. Nickolas, C., 2011. The Basics of Mixers. [online] https://www.digikey.ca/. Available at: ¡https://www.digikey.ca/en/articles/the-basics-of-mixers¿ [Accessed 4 July 2022].

55. Niknejad, A., 2016. Introduction to Receivers and Mixers.

56. Bailey, M., 2011. General Layout Guidelines for RF and Mixed-Signal PCBs. [ebook] Maxim Integrated. Available at: <https://www.maximintegrated.com/en/design /technical-documents/tutorials/5/5100.html> [Accessed 4 July 2022].

57. Pcbway.com. 2022. Impedance Calculation - PCB Prototype the Easy Way - PCB-Way. [online] Available at: https://www.pcbway.com/pcb_prototype /impedance_calculator.html [Accessed 4 July 2022].

58. Sedra, A. S., & Smith, K. C. (1987). Microelectronic circuits. New York: Holt, Rinehart, and Winston.

59. Siglent. 2017. Spectrum Analyzer Basics: Bandwidth - Siglent. [online] Available at: https://www.siglenteu.com/application-note/spectrum-analyzer-basics-bandwidth [Accessed 6 July 2022].

60. Grier, A.T., Ferrier-Barbut, I., Rem, B.S., Delehaye, M., Khaykovich, L., Chevy, F. and Salomon, C., 2013. -enhanced sub-Doppler cooling of lithium atoms in D 1 gray molasses. Physical Review A, 87(6), p.063411.

61. K. J. Åström, Control System Design, Preprint, 2002. Online access

62. Steck, D., 2003. Cesium D Line Data. Los Alamos National Laboratory.

63. FOOT, C. J. (2005). Atomic physics. Oxford, Oxford University Press.

64. Hinkle, Z., 2022. Ultra-Cold CsLi Molecules as a Platform for Quantum Information Processing. University of Waterloo

65. Gehm, M.E., 2003. Properties of 6Li. Jetlab,

66. Bakr, W.S., Gillen, J.I., Peng, A., Fölling, S. and Greiner, M., 2009. A quantum gas microscope for detecting single atoms in a Hubbard-regime optical lattice. Nature, 462(7269), pp.74-77.

67. Chin, C., Grimm, R., Julienne, P. and Tiesinga, E., 2010. Feshbach resonances in ultracold gases. Reviews of Modern Physics, 82(2), p.1225.

68. Maes, W. (2018) "How to make an arduino fast enough to..."